Nanoscopic and spectroscopic methods to investigate biomolecular recognitions in cancer research

PhD thesis of Simona Santini

in

Genetics and Cell Biology (XXVIII Cycle)

Faculty of Mathematics, Physics and Natural sciences

Department of Ecological and Biological Sciences

Tutors:	Prof . dr. Salvatore Cannistraro
	Prof. dr. Anna Rita Bizzarri
Examination panels:	Dr. Gabriella D'Orazi (Università di Chieti)
	Dr. Susanna Molinari (Università di Modena e Reggio Emilia)
	Dr. Maria Forlenza (University of Wageningen)

These studies have been supported by grants from the **Italian Association for Cancer Research (AIRC)**. Grants No. IG 10412 and IG 15866.

Cover

Schematic representation of the Atomic Force Spectroscopy (AFS) setup. p28 (amino acids 50-77 of Azurin, chain B of PDB entry 4AZU), in magenta is anchored to the AFS tip while the p53 DNA Binding Domain, DBD (PDB entry 1TUP), in green, is immobilized on glass substrate.

Contents

Abbreviations

AFM	Atomic Force Microscopy
AFS	Atomic Force Spectroscopy
CDK	Cyclin-dependent kinase
CM	Contact Mode
CTD	C-terminal domain
DBD	DNA Binding Domain
ET	Electron Transfer
FDA	Food and drug Administration
GOF	Gain of function
MCK	Multi-cycle kinetic
MD	Molecular dynamic
MDM2	Mouse Double Minute 2
NC	Non-Contact
NTD	N-terminal domain
PRO	Prolin-Rich Domain
RC	Random coil
RD	Regulatory Domain
ROS	Reactive oxygen species
RU	Resonance Unit
TAD	Transcriptional Activation Domain
TD	Tetramerization Domain
TM	Tapping Mode
UV	Ultraviolet

Chapter 1

Oncosuppressor p53, p53 family proteins, anticancer proteins and peptides: a general overview

Cancer is a genetic disease characterized by abnormal cells growth due to the accumulation of genetic mutations that activate oncogenes or inactivate tumour suppressors genes. One of the most important tumour suppressor is p53, the so called "guardian of the genome" for its crucial role in the cell cycle progression control and coordination of cellular response to a broad range of stress factors ensuring the maintenance of genomic stability and the prevention of cancer development. As a key coordinator of cellular defence, p53 is a common denominator in human cancers, in most of which it is mutated or its pathway altered (*Lane et al., 1992; Prives and Hall, 1999; Levine, 1997; Vogelstein et al., 2000*; *Vousden and Prives, 2009; Harris, 1996; Greenblatt et al., 1994*). p53 prominent position in tumour development has stimulated a lot of research into both its biological and clinical aspects and has drawn great attention from the world-wide cancer researchers with the aim to target it or its pathway for the development of improved cancer therapies.

In this respect, the main purpose of this work is the molecular and kinetic characterization, by nanoscopic and spectroscopic techniques, of biomolecular interactions of pharmaceutical interest involving p53, p53 family proteins, as well peptides or proteins showing anticancer activities somehow connected with p53 pathway. This work, conceived as the natural progression of a wide project in which I was involved since my master thesis, has been supported by the Italian Association for Cancer Research (AIRC) and carried out in the framework of the close collaboration with the Research Group of Dr. C. Beattie (Department of Surgical Oncology, Illinois University, Chicago) and with that of Dr. G. Blandino (Translational Oncogenomic Unit, Molecular Medicine Area, Regina Elena National Cancer Institute, Rome).

p53 structure, pathway and its role in the control of cancer progression

Human p53 protein, is a homotetramer in which each monomer consists of 393 amino acids residues structured in three functional regions: an N-terminal Domain (NTD, aa 1–93), including a Transcriptional Activation Domain (TAD, aa 1-63) involved in the p53 transcriptional function and a Proline-rich Domain (PRO, aa 64-92) necessary for an efficient growth suppression; a core DNA Binding Domain (DBD, aa 102–292) responsible for site-specific DNA binding; and a C-terminal Domain (CTD, aa 293–393) including a Tetramerization Domain (TD, aa 326-353), responsible for the p53 tetramerization, and a Regulatory Domain (RD, aa 363-393), regulating the DBD function (*Levine, 1997*).

In healthy cells, p53 is kept at low concentration by a series of ubiquitin E3 ligases (*Kruse and Gu, 2009*), the most prominent of which being MDM2 (Mouse Double Minutes 2). It is a negative regulator protein, that is found to be over expressed in many tumours (*Freedman et al., 1999*) and that, upon binding to p53, blocks its transcriptional activity, favours its nuclear export and promotes its proteasomal degradation (*Levine, 1997; Haupt et al., 1997; Brooks and Gu, 2006*). In response to a broad range of stress signals (e.g. DNA damage, hypoxia, depletion of microtubules or nucleotides, etc.), post-translational modifications of p53 mainly affect the stability of its interaction with MDM2 (*Haupt et al, 1997; Roth et al., 1998; Honda et al., 2007; Momand et al., 1992*) lowering the degree of p53 degradation. The consequent increase of its intracellular levels thus results in the gene transcription responsible for DNA repair, cell cycle arrest and apoptosis (*Oren, 2003*) (Fig. 1.1).

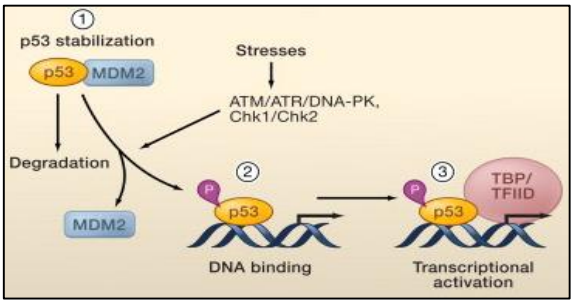

Figure 1.1. The classical model of p53 activation is based on three steps: 1) stress signals induce p53 stabilization mediated by phosphorylation (P) by ATM, ATR and other kinases; 2) binding of active p53 to DNA; 3) recruitment of the general transcription machinery to activate transcription of p53 target genes. Figure is from *Kruse and Gu, 2009.*

The MDM2-p53 interaction is regarded as a key point in the p53 activity control (*Michael and Oren, 2003; Wiman, 2006; Vassilev, 2007; Bossi and Sacchi, 2007; Tollini et al., 2014*) and has stimulated researches aimed at identified molecules able to stabilize p53 by interfering with its interaction with MDM2. The identification of Nutlin (*Klein and Vassilev, 2004; Vassilev, 2004*) as the first selective and potent small molecule able to disrupt the MDM2-p53 interaction with *in vivo* and *in vitro* activity, strengthens the notion that targeting such an interaction can provide a viable strategy to treat cancer. Efforts made to found molecules able to stabilize p53, have led also to the identification of Azurin (Fig. 1.2) as a potent inducer of apoptosis and cancer regression. In particular, it has been found that Azurin, a 128 amino acids copper containing protein with electron transfer (ET) activity in *Pseudomonas Aeruginosa*, is internalized efficiently and preferentially in cancerous with respect to normal cells and shows anticancer activity both *in vitro* (*Yamada et al. 2002a; Yamada et al., 2002b; Goto et al., 2003; Punj et al., 2003; Punj et al., 2004; Yamada et al., 2004*) and *in vivo* (*Yamada et al., 2002a; Punj et al., 2004*). Azurin was found to induce a p53-mediated apoptosis in murine J774, human breast cancer, melanoma and osteosarcoma cells but not in p53-negative osteosarcoma and normal liver cells and was shown to inhibit the proliferation of p53 wild-type breast and melanoma xenografts in athymic mice *(Taylor et al., 2009; Yamada et al., 2009*). Moreover, the pro-apoptotic action of Azurin on cancer cells has been verified to be concomitant with the formation of a complex with p53, thereby leading to both its stabilization and intracellular level increase (*Yamada et al., 2002a,, Yamada et al., 2002b; Punj et al., 2003; Goto et al., 2003; Yamada et al., 2004; Punj et al., 2004).* The p53-Azurin complex has been subjected to different experimental investigations in order to get insight into its relevant kinetic and molecular aspects (*Taranta et al., 2008; Apiyo et al., 2005; De Grandis et al., 2007; Taranta et al., 2009; Domenici et al., 2011, Funari et al., 2010*). Overall it emerged that, by binding to p53 NTD or DBD, Azurin stabilizes p53 by reducing the MDM2–p53 association rate constant and binding affinity through an allosteric mechanism without hindering the MDM2 access to p53 (*Domenici et al., 2011).*

In addition to MDM2 however, other E3 ligases, such as COP1 (constitutively photomorphogenic 1), Pirh2 (p53-induced RING-H2 domain protein) and TOPORS (topoisomerase I binding, arginine/serine rich), also bind to p53 and negatively regulate it (*Leng et al., 2003; Dornan et al., 2004a; Dornan et al., 2004b; Rajendra et al., 2004, Dornan*

et al., 2006; Wang et al., 2011). Among these, COP1 has been found to be over expressed in breast, ovarian, hepatocellular carcinomas, likely contributing to the accelerated degradation of p53 and attenuating its tumour suppressor function (*Dornan et al., 2004b*). Moreover, it has been found that COP1 silencing inhibits tumour growth thus suggesting that COP1 may be a promising target for systemic therapy (*Lee et al., 2010*). This is thus a further confirmation that stabilizing p53 and enhancing its intracellular levels, through the inhibition of its interaction with ubiquitin ligases, could be a useful strategy to hamper cancer cells progression (*Hong et al., 2014*).

p28, a 28 amino acids peptide as a potent anticancer agent

In order to search for efficient therapeutic molecules able to stabilize p53, the group of Drs. Beattie and Gupta (Depart. of Surgical Oncology of the College of Medicine Chicago (USA), has investigated peptides formed by suitably truncated portions of the previously mentioned ET protein Azurin. Promising results have been obtained with p28 (Fig. 1.2) , a 2.9 kDa peptide fragment formed by the amino acids 50–77 of Azurin (LSTAADMQGVVTDGMASGLDKDYLKPDD) and encompassing the Azurin α–helix.

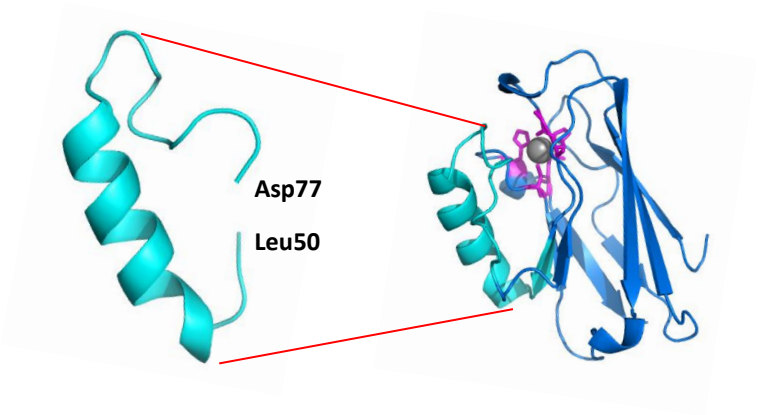

Figure 1.2. On the right: three dimensional structure of Azurin (PDB entry 4 AZU, chain B). The grey sphere in the northern part of the molecule is the copper atom while magenta sticks represent the residues coordinating it. On the left: Azurin peptide fragment p28 (aa 50-77).

p28 has been shown to retain both *in vitro* (*Yamada et al., 2005; Taylor et al., 2009; Yamada et al., 2009*) and *in vivo* (*Yamada et al., 2009; Mehta et al., 2010*) the cellular penetration ability of the whole protein as well its antitumor activity (*Taylor et al., 2009; Yamada et al.,*

2009; Mehta et al., 2010). Notably, the cellular penetration of p28 at relatively high concentrations is not accompanied by haemolytic activity against human erythrocytes or by any cell membrane toxicity (*Mehta et al., 2010*). Moreover, it does so without any stress to normal cells and exhibits no preclinical or clinical toxicity. Because of all these peculiarities, p28 is entering its second clinical trial in patients with advanced refractory central nervous system tumours under Food and Drug Administration (FDA) allowance.

When the AIRC project, in which I have been involved started, there were only preliminary indication and many hypothesis concerning the p28 mode of action. Immunoprecipitation techniques showed that p28 antiproliferative action should be connected with the ability of the p28 amino acids 11 to 18 to bind to p53 mostly at level of its DBD and, to a lesser extent, of its NTD (*Yamada et al., 2009*) resulting in the intracellular level rise of p53. p53 reactivation thus resulted in the intracellular levels increase of cyclin-dependent kinase (CDK) p21 and p27 leading to the inhibition of the cell cycle progression at G_2-M phase (*Taylor et al., 2009*). It was suggested that p28 interaction with p53 could interfere with the p53 down-regulation exerted by some ubiquitin E3 ligases, among which MDM2, thus inhibiting its ubiquitination and proteasomal degradation (*Jia et al., 2011*). However, immunoprecipitation studies (*Yamada et al., 2009*) showed that p28 seems not to directly interfere with the MDM2 binding to p53, even not excluding that it might modify the affinity between p53 and MDM2 through allosteric effects, similarly to what observed for Azurin (*Dominici et al., 2011; Funari et al., 2010*). Another hypothesis was that p28 could exert the p53-ubiquitination regulation through an MDM2-independent pathway (*Jia et al., 2011*) acting, for example, on the recently discovered ubiquitin E3 ligase, COP1 (*Dornan et al., 2006; Li et al., 2012*). In this context it appeared crucial to unravel the molecular mechanisms at the basis of the anticancer action of the p28 peptide. Indeed, this could: i) help optimize its cell penetrating capability; ii) increase its targeting specificity; iii) optimize its antitumour activity; iv) help oncologists identifying which patients are most likely to respond to drug.

One of the main goal of this project has thus been to elucidate the molecular mechanisms of the p28-mediated p53 stabilization by using nanothecnological and spectroscopic approaches able to complement data from common techniques of immunoprecipitation. Atomic Force Spectroscopy (AFS, *Appendix A*) and Surface Plasmon Resonance (SPR, *Appendix B*), have been used, also combined with computational methods and fluorescence spectroscopy .

First, by taking advantage from studies performed during my master thesis, the molecular details of p28 interaction with wild type p53 DBD have been defineded by computational methods. The obtained data, combined with results from biochemical approaches performed by the Prof. Beattie group, have allowed to elucidate the p28 effects and mode of action at the molecular level in cell carrying p53 wild type and, at least some, p53 mutants, as published in *Yamada et al., 2013* (Chapter 2).

Second, I have used AFS to characterize the kinetic and molecular details of the p28 interaction with mutants p53 DBD. Both non physiological (L114D, A119D, C124D and C229D) and physiological (K164E, R273H, P223L,V274F) DBD mutants have been taken into consideration. Non physiological DBD mutants represent a model to show how, alteration in p28 binding capability to the DBD, would be due to a DBD structural change induced by mutations that reduce the hydrophobicity of the p28 binding site. On the other hand, being p53 mutated in more than 50 % of human cancers and being about 80% of p53 mutations missense mutations mainly located in the p53 DBD that lead to the functional loss of p53 antitumour activity (*Freed-Pastor and Prives, 2012*), the capability of p28 to interact with, and stabilize physiological p53 mutants certainly deserves considerable interest. AFS data have been complemented by computational docking studies carried out by the Prof. Beattie' group and Raman data obtained by members of Prof. Cannistraro group to which I belong, in order to further investigate the deep correlation between mutations induced DBD conformational changes and p28 binding affinity (virtual and experimental), and they have been gathered in a preliminary draft (Chapter 3).

Mutant p53 showing gain of function activity as a target for anticancer drugs

Mutant p53 not only can lose its physiological function but it can also acquire negative activity and oncogenic properties, what is referred to as “gain of function” (GOF) phenomenon (*Brosh and Rotter, 2009*). Among the properties that mutant p53 can gain, there is its capability of interact with and sequestrate its related proteins p63 and p73, abrogating their antitumoural function (*Di Como et al., 1999; Strano et al., 2000; Strano et al., 2002; Strano et al., 2007*) and thus making cancer cells more aggressive. In particular, the p73 loss of function consequent to its possible interaction with mutant p53 has been shown to be a major determinant of human tumour chemoresistance (*Lunghi et al., 2009*). In connection

with this, an appealing strategy for cancer therapy is just to target p73 in order to disrupt its interaction with mutant p53 and restore p73 antitumoural function (*Di Agostino et al., 2008*). Along this direction, it has emerged the need for a deeper knowledge of the interaction mechanisms underlying the formation of the mutant p53/p73 complex. In connection with this, I have characterize the p53R175H/p73 interaction both at the single molecule level by AFS and in bulk condition by SPR and data have been published in *Santini et al., 2014a* (Chapter 4).

Azurin – Cytochrome C551 interaction mechanism

As before mentioned, cupredoxin Azurin from *Pseudomonas Aeruginosa* has attracted greater interest over the years for its anticancer role connected with its ability to destabilize the interaction between MDM2 and p53. However it cannot be completely excluded that Azurin anticancer activity could involve oxygen reactive species (ROS) generation somehow connected with its ET capability (*Liu et al., 2008*). In connection with this, the attempts to knowledge of the Azurin physiological role and interaction with its physiological partner, have attracted a fairly good interest. Fluorescence spectroscopy and SPR have thus been used to characterize, from a kinetic point of view, the Azurin interaction with its physiological partner Cytochrome C551 (*Santini et al., 2014b,* Chapter 5).

References

Apiyo D, Wittung-Stafshede P. Unique complex between bacterial azurin and tumor suppressor protein p53. 2005. *Biochem. Biophys. Res. Commun*. **332**: 965-968.

Bossi G, Sacchi A. 2007. Restoration of wild-type p53 function in human cancer: relevance for tumour therapy. *Head & Neck* **29:** 272-284.

Brooks CL, Gu W. 2003. Ubiquitination, phosphorylation and acetylation: the molecular basis for p53 regulation. *Curr. Opin. Cell Biol*. **15**: 164–171.

Brosh R, Rotter V. 2009. When mutants gain new powers: news from the mutant p53 field. *Nat. Rev. Cancer* **9**: 701-713.

De Grandis V, Bizzarri AR, Cannistraro S. 2007. Docking study and free energy simulation of the complex between p53 DNA-binding domain and azurin. *J. Mol. Recognit*. **20**: 215-226.

Di Agostino S, Cortese G, Monti O, Dell'Orso S, Sacchi A, Eisenstein M, Citro G, Strano S, Blandino G. 2008. The disruption of the protein complex mutantp53/p73 increases selectively the response of tumor cells to anticancer drugs. *Cell Cycle* **7**: 3440-3447.

Di Como CJ, Gaiddon C, Prives C. 1999. p73 function is inhibited by tumor-derived p53 mutants in mammalian cells. *Mol. Cell. Biol.* **19**: 1438–1449.

Domenici F, Fiasconi M, Mazzei F, D'Orazi G, Bizzarri AR, Cannistraro S. 2011. Azurin modulates the association of Mdm2 with p53: SPR evidence from interaction of the full-length proteins. *J. Mol. Recognit. **24**:* 707-714.

Dornan D, Bheddah S, Newton K, Ince W, Frantz GD, Dowd P, Koeppen H, Dixit VM, French DM. 2004a. COP1, the negative regulator of p53, is overexpressed in breast and ovarian adenocarcinomas. *Cancer Res.* **64**: 7226–7230.

Dornan D, Wertz I, Shimizu H, Arnott D, Frantz GD, Dowd P, O'Rourke K, Koeppen H, Dixit VM. 2004b. The ubiquitin ligase COP1 is a critical negative regulator of p53. *Nature* **429**: 86–92.

Dornan D, Shimizu H, Mah A, Dudhela T, Eby M, O'Rourke K, Seshagiri S, Dixit VM. 2006. ATM engages autodegradation of the E3 ubiquitin ligase COP1 after DNA damage. *Science* **313**: 1122–1126.

Freed-Pastor WA, Prives C. 2012. Mutant p53: one nam, many proteins. *Gene Dev*. **26:** 1268-1286.

Freedman DA, Wu L, Levine AJ. 1999. Functions of the Mdm2 oncoprotein. *Cell. Mol. Life Sci.* **55**: 96-107.

Funari G, Domenici F, Nardinocchi L, Puca R, D'Orazi G, Bizzarri AR, Cannistraro S. 2010. Interaction of p53 with Mdm2 and azurin as studied by atomic force spectroscopy. *J. Mol. Recognit*. **23**: 343-351.

Goto M, Yamada T, Kimbara K, Horner J, Newcomb M, Das Gupta TK, Chakrabarty AM. 2003. Induction of apoptosis in macrophages by Pseudomonas aeruginosa Azurin: tumour-suppressor protein p53 and reactive oxygen species, but not redox activity, as critical elements in cytotoxicity. *Mol. Microbiol*. **47**: 549–559.

Greenblatt MS, Bennett WP, Hollstein M, Harris CC. 1994. Mutations in the p53 tumor suppressor gene: clues to cancer etiology and molecular pathogenesis. *Cancer Res.* **54**: 4855-4878.

Harris CC. 1996. Structure and function of the p53 tumor suppressor gene: clues for rational cancer therapeutic strategies. *J. Natl. Cancer Inst*. **88**: 1442–1455.

Haupt Y, Maya R, Kazaz A, Oren M. 1997. Mdm2 promotes the rapid degradation of p53. *Nature* **387**: 296–299.

Honda R, Tanaka H, Yasuda, H. 1997. Oncoprotein MDM2 is a ubiquitin ligase E3 for tumor suppressor p53. *FEBS Lett.* **420**: 25–27.

Hong B, van den Heuvel AP, Prabhu VV, Zhang S, El-Deiry WS. 2014. Targeting tumor suppressor p53 for cancer therapy: strategies, challenges and opportunities. *Curr. Drug Targets.* **15**: 80-89.

Jia L, Gorman GS, Coward LU, Noker PE, McCormick D, Horn TL, Brooks Harder J, Muzzio M, Prabhakar B, Ganesh B, Das Gupta TK, Beattie CW. Preclinical pharmacokinetics, metabolism, and toxicity of azurin-p28 a peptide inhibitor of p53 ubiquitination. 2011. *Cancer Chemother. Pharmacol*. **68**: 513-524.

Klein C, Vassilev LT. 2004. Targeting the p53-MDM2 interaction to treat cancer. *Br. J. Cancer* **91:** 1415-1419.

Kruse JP, Gu W. 2009. Modes of p53 regulation. *Cell* **137**: 609-622.

Lane DP. 1992. Cancer. p53, guardian of the genome. *Nature* **358**: 15–16.

Lee YH, Andersen JB, Song HT, Judge AD, Seo D, Ishikawa T, Marquardt JU, Kitade M, Durkin ME, Raggi C, Woo HG, Conner EA, Avital I, Maclachlan I, Factor VM, Thorgeirsson SS. 2010. Definition of ubiquitination modulator COP1 as a novel therapeutic target in human hepatocellular carcinoma. *Cancer Res.* **70**: 8264–8269.

Leng RP, Lin Y, Ma W, Wu H, Lemmers B, Chung S, Parant JM, Lozano G, Hakem R, Benchimol S. 2003. Pirh2, a p53-induced ubiquitin-protein ligase, promotes p53 degradation. *Cell* **112**: 779–791.

Levine AJ. 1997. p53, the cellular gatekeeper for growth and division. *Cell* **88**: 323–331.

Li YF, Wang DD, Zhao BW, Wang W, Huang CY, Chen YM, Zheng Y, Keshari RP, Xia JC, Zhou ZW. 2012. High level of COP1 expression is associated with poor prognosis in primary gastric cancer. *Int. J. Biol. Sci.* **8**: 1168–1177.

Liu B, Chen Y, St. Clair DK. 2008. ROS and p53: versatile partnership. *Free Radical Bio. Med.* **44**:1529−1535.

Lunghi P, Costanzo A, Mazzera L, Rizzoli V, Levrero M, Bonati A. 2009. The p53 family protein p73 provides new insights into cancer chemosensitivity and targeting. *Clin. Cancer. Res*. **15**: 6495-6502.

Mehta RR, Hawthorne M, Peng X, Shilkaitis A, Mehta RG, Beattie CW, Das Gupta TK. 2010. a 28-amino-acid peptide fragment of the cupredoxin azurin prevents carcinogen-induced mouse mammary lesions. *Cancer Prev. Res. (Phila)* **3:** 1351-1360.

Michael D, Oren M. 2003. The p53-Mdm2 module and the ubiquitin system. *Semin. Cancer Biol.* **13**: 49-58.

Momand J, Zambetti GP, Olson DC, George D, Levine AJ. 1992. The mdm-2 oncogene product forms a complex with the p53 protein and inhibits p53-mediated transactivation. *Cell* **69**:1237–1245.

Oren M. 2003. Decision making by p53: life, death and cancer. *Cell. Death. Diff.* **10**: 431-442.

Punj V, Das Gupta TK, Chakrabarty AM. 2003. Bacterial cupredoxin azurin and its interactions with the tumor suppressor protein p53. *Biochem. Biophys*. **312**: 109–114.

Punj V, Bhattacharyya S, Saint-Dic D, Vasu C, Cunningham EA, Graves J, Yamada T, Constantinou AI, Christov K, White B, Li G, Majumdar D, Chakrabarty AM, Das Gupta TK. 2004. Bacterial cupredoxin azurin as an inducer of apoptosis and regression in human breast cancer. *Oncogene* **23**: 2367– 2378.

Prives C, Hall PA. 1999. The p53 pathway. *J. Pathol*. **187**: 112–126.

Rajendra R, Malegaonkar D, Pungaliya P, Marshall H, Rasheed Z, Brownell J, Liu LF, Lutzker S, Saleem A, Rubin EH. 2004. Topors functions as an E3 ubiquitin ligase with specific E2 enzymes and ubiquitinates p53. *J. Biol. Chem.* **279**: 36440–36444.

Roth J, Dobbelstein M, Freedman DA, Shenk T, Levine AJ. 1998. Nucleocytoplasmic shuttling of the hdm2 oncoprotein regulates the levels of the p53 protein via a pathway used by the human immunodeficiency virus rev protein. *EMBO J.* **2**: 554–564.

Santini S, Di Agostino S, Coppari E, Bizzarri AR, Blandino G, Cannistraro S. 2014a. Interaction of mutant p53 with p73: A Surface Plasmon Resonance and Atomic Force Spectroscopy study. *Biochim. Biophys. Acta* **1840**: 1958-1964.

Santini S, Bizzarri AR, Yamada T, Beattie CW, Cannistraro S. 2014b. Binding of azurin to cytochrome c 551 as investigated by surface plasmon resonance and fluorescence. *J. Mol. Recognit.* **27**: 124-130.

Sigal A, Rotter V. 2000. Oncogenic mutations of the p53 tumor suppressor: the demons of the guardian of the genome. *Cancer Res.* **60**: 6788-6793.

Strano S, Munarriz E, Rossi M, Cristofanelli B, Shaul Y, Castagnoli L, Levine AJ, Sacchi A, Cesareni G, Oren M, Blandino G, 2000. Physical and functional interaction between p53 mutants and different isoforms of p73. *J. Biol. Chem*. **275**: 29503–29508.

Strano S, Fontemaggi G, Costanzo A, Rizzo G, Monti O. Baccarini A. 2002. Physical interaction with human tumor derived p53 mutants inhibits p63 activities. *J. Biol. Chem.* **277**: 18817–18826.

Strano S, Dell'Orso S, Di Agostino S, Fontemaggi G, Sacchi A, Blandino G. 2007. Mutant p53: an oncogenic transcription factor. *Oncogene* **26**: 2212-2219.

Taranta M, Bizzarri AR, Cannistraro S. 2008. Probing the interaction between p53 and the bacterial protein azurin by Single Molecule Force Spectroscopy. *J. Mol. Recognit*. **21**:63-70.

Taranta M, Bizzarri AR, Cannistraro S. 2009. Modelling the interaction between the N-terminal domain of the tumor suppressor p53 and azurin. *J. Mol. Recognit*. **22**: 215-222.

Tollini LA, Jin A, Park J, Zhang Y. 2014. Regulation of p53 by Mdm2 E3 ligase function is dispensable in embryogenesis and development, but essential in response to DNA damage. *Cancer Cell*. **26**: 235–247.

Vassilev LT. 2004. Small-molecule inhibitors of p53-MDM2 binding: research tools and potential cancer therapeutics. *Cell cycle* **3**: 419-421.

Vassilev LT. 2007. Mdm2 inhibitors for cancer therapy. *Trends Mol. Med*. **13**: 23-31.

Vogelstein B, Lane D, Levine AJ. 2000. Surfing the p53 network. *Nature* **408**: 307–310.

Vousden KH, Prives C. 2009. Blinded the light: the growing complexity of p53. *Cell* **137**: 413-431.

Wang L, He G, Zhang P, Wang X, Jiang M, Yu L. 2011. Interplay between MDM2, MDMX, Pirh2 and COP1: the negative regulators of p53. *Mol. Biol. Rep.* **38**: 229–236.

Wiman KG. 2006. Strategies for therapeutic targeting of the p53 pathway in cancer. *Cell Death Diff.* **13** 921-926.

Taylor BN, Mehta RR, Yamada T, Lekmine F, Christov K, Chakrabarty AM, Green A, Bratescu L, Shilkaitis A, Beattie CW, Das Gupta TK. 2009. Non cationic peptides obtained from azurin preferentially enter cancer cells. *Cancer Res.* **69**: 537-546.

Yamada T, Goto M, Punj V, Zaborina O, Chen ML, Kimbara K, Majumdar D, Cunningham E, Das Gupta TK, Chakrabarty AM. 2002a. Bacterial redox protein azurin, tumor suppressor protein p53, and regression of cancer. *Proc. Natl. Acad. Sci. USA* **99**: 14098–14103.

Yamada T, Goto M, Punj V, Zaborina O, imbara K, Das Gupta TK, and Chakrabarty AM. 2002b. The bacterial redox protein azurin induces apoptosis in J774 macrophages through complex formation and stabilization of the tumor suppressor protein p53. *Infect. Immun.* **70**: 7054–7062.

Yamada T, Hiraoka Y, Ikehata M, Kimbara K, Avner BS, Das Gupta TK, Chakrabarty AM. 2004. Apoptosis or growth arrest: modulation of tumor suppressor p53's specificity by bacterial redox protein azurin. *Proc. Natl. Acad. Sci. USA* **101**: 4770–4775.

Yamada T, Fialho AM, Punj V, Bratescu L, Das Gupta TK, Chakrabarty AM. 2005 Internalization of bacteria redox protein azurin in mammalian cells: entry domain and specificity. *Cell Microb.* **10***:* 1418–1431.

Yamada T, Mehta RR, Lekmine F, Christov K, King ML, Majumdar D, Shilkaitis A, Green A, Bratescu L, Beattie CW, Das Gupta TK. 2009. A peptide fragment of azurin induces a p53 – mediated cell cycle arrest in human breast cancer cells. *Mol. Cancer Ther.* **8:** 2947–2958.

Yamada T, Christov K, Shilkaitis A, Bratescu L, Green A, Santini S, Bizzarri AR, Cannistraro S, Gupta TKD, Beattie CW. 2013. p28, a first in class peptide inhibitor of COP1 binding to p53. *British J. Cancer* **108**: 2495-2504.

Chapter 2

A detailed study of p28 mode of action

To define p28 mode of action at the molecular level I have taken advantage from studies performed during my master thesis when experimental techniques and computational methods were applied to study the molecular and kinetics details of the interaction between p28 and both p53 full length protein and its domains. At first, AFS was used revealing that a specific biorecognition process occurs between p28 and the DBD of p53 while there is almost no interaction with the p53 NTD. These findings prompted me to investigate the molecular details of the p28-DBD complex by means of computational methods that allow to predict the structure of a complex simply starting from the three dimensional (3D) structure of the two partners. The molecular details of the p28 interaction with the p53 DBD were thus disclosed. These data, combined with results from common biochemical approaches performed by Prof. Beattie group, have allowed to completely elucidate the p28 mode of action at the molecular level.

Preliminary data

Interaction of p28 with p53 and its isolated domains as studied by atomic force spectroscopy and computational methods

AFS was used to investigate the interaction of p28 with full length p53 and its DBD and NTD (*Bizzarri et al., 2011*) while the interaction with the CTD was excluded on the basis of competition assays results (*Yamada et al., 2009*). AFS experiments (see *Appendix A* for details on the technique) were performed by anchoring p28 to the AFS tip while p53 and its fragments were immobilized on a glass substrate. To reach a stable anchoring of p28 to the tip without altering the system, a p28 peptide modified with the addition of a Cysteine at the N-terminal (p29) was used and a well-established chemical procedure was followed. Also the immobilization of p53 full length and of its fragments on the glass substrate was based on a previously developed strategy in which amino-silane-treated surfaces have been linked with polyethylene polymers, whose ends were suitably tailored for covalent reaction with the

amino groups of biomolecules. The AFS approach revealed that a specific interaction occurs between p28 and p53, leading to the formation of a stable complex, characterized by a dissociation constant in the order of 10^{-6} M. Such an interaction appeared confined to the DBD core domain of p53 while almost no interaction was found between p28 and the p53 NTD (*Bizzarri et al., 2011*).

Once the p53 region interacting with p28 was determined, computational methods were used to get further inside into the molecular details of the p28 interaction with the p53 DBD (*Santini et al., 2011*). To this aim, the 3D structures of both p28 and DBD were necessary. However, while the crystal structure of DBD is well defined (*Cho et al., 1994*), the folding state of p28 inside the cell is not known, hence two different starting structures for the peptide were taken into consideration: (i) a folding structure derived from the crystallographic structure of Azurin and suitably relaxed by molecular dynamics simulation and (ii) an unfolded structure obtained by submitting the folded one to high-temperature cycles to mimic the structure obtained after synthesis. Each of these two models of p28 (folded and unfolded) were separately submitted to a docking procedure with the X-ray structure of the DBD. Docking procedure was then followed by cluster analysis, molecular dynamic (MD) simulations and binding free energy calculations. Such an approach revealed that both the folded and the unfolded p28 peptides can form complexes with the DBD characterized by a rather low binding free energy, high shape complementarily, the presence of several hydrogen bonds at the interface, and involving similar DBD regions (*Santini et al., 2011*).

Overall, AFS and computational methods, showed the occurrence of a stable complex between p28 and the p53 DBD and allowed to hypothesize that the p28 anticancer potentiality might be connected with its ability to hamper the binding of ubiquitin ligases (such as COP1, Pirh2 and perhaps TOPORS and ARF-BP1) (*Chan et al., 2006; Rajendra et al., 2004; Chen et al., 2005; Dornan et al., 2004a; Corcoran et al., 2004*) to the DBD by preventing in such a way the tumour suppressor p53 from a proteasomal degradation.

The p28 mode of action was then completely disclosed in a work published on British Journal of Cancer, which is reported below, and in which computational data have been complemented by results from biochemical methods.

p28, a first in class peptide inhibitor of Cop1 binding to p53

Abstract

Background: A 28 amino-acid (aa) cell-penetrating peptide (p28) derived from Azurin, a redox protein secreted from the opportunistic pathogen *Pseudomonas Aeruginosa*, produces a post-translational increase in p53 in cancer cells by inhibiting its ubiquitination.

Methods: In silico computational simulations were used to predict motifs within the p53 DNA-binding domain (DBD) as potential sites for p28 binding. In vitro direct and competitive pull-down studies as well as western blot and RT-PCR analyses were used to validate predictions.

Results: The L_1 loop (aa 112–124), a region within the S_7–S_8 loop (aa 214–236) and T140, P142, Q144, W146, R282 and L289 of the p53DBD were identified as potential sites for p28 binding. p28 decreased the level of the E3 ligase COP1 >80%, in $p53^{wt}$ and $p53^{mut}$ cells with no decrease in COP1 in $p53^{dom/neg}$ or $p53^{null}$ cells. Brief increases in the expression of the E3 ligases, TOPORS, Pirh2 and HDM2 (human double minute 2) in $p53^{wt}$ and $p53^{mut}$ cells were in response to sustained increases in p53.

Conclusion: These data identify the specific motifs within the DBD of p53 that bind p28 and suggest that p28 inhibition of COP1 binding results in the sustained, post-translational increase in p53 levels and subsequent inhibition of cancer cell growth independent of an HDM2 pathway.

These results have been published as:

Yamada T, Christov K, Shilkaitis A, Bratescu L, Green A, Santini S, Bizzarri AR, Cannistraro S, Gupta TKD, Beattie CW. 2013. p28, a First in Class Peptide Inhibitor of COP1 Binding to p53. *British J. Cancer* **108**: 2495-2504.

Introduction

The cupredoxin Azurin preferentially enters a wide variety of cancer cells, inducing p53-mediated cytostatic and cytotoxic (apoptotic) effects in murine and human cancer cells (*Yamada et al., 2002; Punj et al., 2004; Apiyo and Wittung-Stafshede, 2005; Bizzarri and Cannistraro, 2009*). Molecular modeling and atomic force microscopy studies suggest that Azurin binds to the flexible L_1 and S_7–S_8 loops of the p53 DNA-binding domain (DBD), forming a stable complex through tight protein–protein interactions (*De Grandis et al., 2007; Taranta et al., 2008*). Amino acids (aa) 50–67 (p18) and 50–77 (p28) of Azurin represent the protein transport domain (*Yamada et al., 2005; Taylor et al., 2009*) and motif (*Yamada et al., 2009*) responsible for Azurin's antiproliferative activity, respectively. Exposure of $p53^{wt}$ MCF-7 breast cancer cells to p28 induces a post-translational increase in the level and activity of p53, inhibits the cell cycle at the G_2–M transition and induces apoptosis, but not in the isogenic $p53^{dom/neg}$ cell line MDD2 (*Shaulian et al., 1992; Yamada et al., 2009*).

Intracellular levels of p53 are tightly regulated by a series of ubiquitin E3 ligases that promote ubiquitination and proteasomal degradation of p53 (*Michael and Oren, 2003*). The most prominent is HDM2 (human double minute 2) (*Haupt et al., 1997*). Current small-molecule HDM2 antagonists MI-219/AT-219, RITA, PXN727, Nutlins (cis-imidazoline analogues) and JNJ-26854165 (*Cheok et al., 2011*) bind to HDM2 and inhibit the subsequent ubiquitination and proteolysis of wild-type p53. Unlike these agents, p28 forms a complex (*Bizzarri et al., 2011*) within aa 80–276 of the p53DBD that decreases ubiquitination (*Yamada et al., 2009*) and proteasomal degradation of p53 via an HDM2-independent pathway (*Yamada et al., 2009*). In addition to HDM2, other E3 ligases, COP1 (constitutively photomorphogenic 1), Pirh2 (p53-induced RING-H2 domain protein) and TOPORS (topoisomerase I binding, arginine/serine rich), also reportedly bind to p53 and negatively regulate intracellular levels of p53 (*Leng et al., 2003; Dornan et al., 2004a; Dornan et al., 2004b; Rajendra et al., 2004; Dornan et al., 2006; Wang et al, 2011*). COP1 is reportedly overexpressed in breast, ovarian and hepatocellular carcinomas, and gastric cancer (*Li et al., 2012*) predictive of survival in the latter (*Dornan et al., 2004b*), suggesting it contributes to the accelerated degradation of the p53 protein and attenuating the tumour suppressor function of p53 (*Dornan et al., 2004b*). Silencing COP1 inhibits tumour growth and suggests COP1 may be a promising target for systemic therapy (*Lee et al., 2010*).

In contrast, COP1 also reportedly acts as a developmentally dependent tumour suppressor (*Migliorini et al., 2011; Vitari et al., 2011*), interacting with the oncoprotein c-Jun (*Bianchi et al.,*

2003) to keep c-Jun at constitutively low levels in vivo and modulate c-Jun/AP-1 transcriptional activity in mice bred to be genetically hypomorphic at the COP1 locus (*Migliorini et al., 2011*). A COP1 deficiency also reportedly leads to c-Jun upregulation in human cancer cells (*Migliorini et al., 2011*), suggesting COP1 is also a tumour suppressor that functions, at least in part, antagonizing c-Jun oncogenic activity in the absence of a genetic interaction between COP1 and p53 (*Migliorini et al., 2011*). Here, we report the underlying mechanism for the post-translational increase in $p53^{wt,mut}$ levels induced by p28 in breast cancer and melanoma cells. p28 inhibits the binding of COP1 to a specific motif of the p53DBD, leading to an autoreduction in COP1 levels (*Dornan et al., 2006*) and an increase in the level of p53 in the absence of any alteration in c-Jun.

Material and methods

Peptide synthesis. p28 (Leu^{50}-Asp^{77} LSTAADMQGVVTDGMAS GLDKDYLKPDD, 2914 Da) was synthesised by C S Bio, Inc. (Menlo Park, CA, USA) at >95% purity and mass balance.

Molecular dynamics. Computer simulations were performed essentially as described (*De Grandis et al., 2007; Bizzarri et al., 2009*). Configurations for Azurin and the DBD of p53 were taken from 1E5Z and 1TUP of PDB files, respectively. The 28 aa of p28 was cut from the crystallographic structure for Azurin and used to generate the configuration file subsequently applied to MD simulations at 300K and P=1 bar. Complete details for MD are in the Supplementary Materials and Methods.

Docking studies. ClusPro (*Kozakov et al., 2010*) was used to conduct automated docking as a six-dimensional search within the rotational space between the two molecules. This generated a set of possible configurations for a predicted series of p53DBD–p28 complexes that were ranked based on scoring. The predicted complexes were then subjected to cluster analysis under a pairwise binding site root mean squared deviation criterion. The cluster model with the best score was used to further compare the protein–protein interface using the ProtorP: Protein–Protein Interface Analysis Server (*Reynolds et al., 2009*).

Cell proliferation and xenograft tumour assays. Human breast cancer cells MCF-7, $p53^{wt}$ (ATCC, Manassas, VA, USA), the isogenic MDD2, $p53^{dom/neg}$ (*Shaulian et al., 1992*) (courtesy of Dr Andrei V. Gudkov, Roswell Park Cancer Institute, Buffalo, NY, USA) and MDA-MB-231,

$p53^{mut}$, as well as normal breast (MCF-10A, $p53^{wt}$) (ATCC) and melanoma cells (UISO-Mel-6, $p53^{null}$; UISO-Mel-23, $p53^{mut}$; UISO-Mel-29, $p53^{wt}$) (*Kichina et al., 2003*) were cultured as described (*Yamada et al., 2002; Punj et al., 2004; Taylor et al., 2009*). p28 is a stable peptide that binds to p53 in the cell nucleus (*Yamada et al., 2009*) with intracellular concentrations reaching 120 ng ml^{-1} (p28) or 0.042 (μmol l^{-1}) 2 h post exposure to 100 μmol l^{-1} p28, which eliminated the need for repeated exposure. The effect of p28 on cell growth was determined by direct cell counting (*Taylor et al., 2009*).

Human melanoma (Mel-29, -23 and -6) and breast cancer cells (MCF-7 and MDA-MB-231) were injected s.c. in the right flank of 5- to 6-week-old male and female athymic mice (*Punj et al., 2004; Jia et al., 2011; Mehta et al., 2011*). When tumours reached 3mm in diameter, animals were randomised into control (20 mice) and treatment (10 mice) groups, and injected i.p. with DTIC (5-(3,3- dimethyl-1-triazeno) imidazole-4-carboxamide), 4mg kg^{-1}, 3 x /week (melanoma); paclitaxel, 12.8 mg kg^{-1} i.p., days 10, 14, 21 and 25 (breast cancer); or p28 10 or 20 mg kg^{-1} i.p. 3 x /week for 30 days. Although p28 is rapidly cleared ($t_{½}$ 0.06 h; clearance (ml kg^{-1} h^{-1}) 2159), it is also rapidly taken up (Vdss (ml kg^{-1}) 297) at pharmacologically active doses (*Punj et al., 2004; Jia et al., 2011; Mehta et al., 2011*). p28 is also stable in murine serum ($t_{1/2}$ ~60 min) (*Punj et al., 2004; Jia et al., 2011; Mehta et al., 2011*) assuring a continuous release of the mature peptide. At necropsy, tumours were dissected, freed of fat and weighed. Statistical comparisons were performed by analysis of variance ANOVA (control vs treatment) (GraphPad InStat ver. 3.0, La Jolla, CA, USA).

Western blot analysis and RT-PCR. Human breast and melanoma cells were cultured with p28 at 50 μmol l^{-1} for 24–72 h, whole-cell lysates prepared and western blot analysis conducted (*Yamada et al., 2002; Yamada et al., 2009*). A list of antibodies used is provided in Supplementary Materials and Methods. Band intensity was determined using UN-SCAN-IT (Silk Scientific Inc., Orem, Utah). Each control and experimental band was normalised by calculating the ratio of a specific protein/actin. Each experimental level was then expressed as the (relative) percentage of control.

Total RNA was extracted from human breast and melanoma cells exposed to p28, and RT-PCR conducted as previously described (*Yamada et al., 2009*). Primer sets are described under Supplementary Materials. Each control and experimental band was normalised by calculating the

ratio of a specific gene/GAPDH. Each experimental level was then expressed as the (relative) percentage of control. The data are representative of at least two independent measures.

Construction and purification of p53 fragments. Plasmid pGEX5X3 (GE Healthcare, Little Chalfont, United Kingdom) expressing GST fused to fragments of human $p53^{wt}$ were constructed by PCR (*Yamada et al., 2009*). DNA fragments encoding aa 1–80, 81–300, 81–160, 161–300 and 301–393 of p53 were amplified with specific primer sets (Supplementary Materials and Methods) and GST fusion proteins purified by Glutathione Sepharose 4B affinity chromatography and HiLoad Superdex 75 gel-filtration column connected to the ÄKTAprime plus FPLC system (GE Healthcare) (*Yamada et al., 2009*).

GST pull-down assays. p28 binding to fragments of p53 was analysed using a GST pull-down assay (*Yamada et al., 2009*). GST fused to fragments of p53 and GST alone were bound to glutathione-Sepharose 4B beads (GE Healthcare), p28 added and incubated for 2 h. Each sample was loaded on 6% native-PAGE. Membranes were incubated with polyclonal anti-p28 antibody, washed three times with Tris–HCl containing 0.05% Tween 20, secondary rabbit IgG-HRP antibody (Sigma-Aldrich, St Louis, MO, USA). COP1 binding to p53 in the presence or absence of p28 was analysed using competitive pull-down assays (*Hosaka et al., 2005*). GST fused to fragments of p53 were immobilised on beads, followed by incubating with or without p28 (10–100 mole excess). Whole-cell lysates containing COP1 were prepared from MCF-7 cells in PBS containing 0.1% Triton X-100, 10% glycerol and a protease inhibitor cocktail (Sigma-Aldrich). Soluble extracts were incubated with beads, each sample washed with PBS, pelleted and analysed with an anti-COP1 antibody.

Results

Docking simulation of p28–p53 complex. ClusPro identified motifs spanning the L_1 loop (aa 112–124), within aa 139–146, a region within the S_7–S_8 loop (aa 214–236) and R282 and L289 of the p53 DBD (*Tu et al., 2008*) that were involved in the binding between p28 and p53 (Figure 2.1A). Molecular surface and electrostatic potential plots of the p53DBD were calculated by DeepView ver. 4.0.3 (Swiss Institute of Bioinformatics, Geneva, Switzerland) (Figure 2.1B). A blue, red and white colour gradient represents positive, negative and neutral (including hydrophobic aa) potentials on the molecular surface, respectively. The DNA-

binding surface of the p53DBD is highly cationic (blue). In contrast, the p28-binding area is essentially neutral (white), suggesting that electrostatic interaction may not have a role in p28 binding to p53 (Figure 2.1B). The amino-acid composition of the predicted p28-binding sites on p53 was FLHSGTAVTCTYPALTPQWEGSDCTHRL or 43% hydrophobic, 36% neutral and 21% hydrophilic residues. p28 bound to 10 of 13 aa (77%) in the L_1 loop that were 50% hydrophobic, 40% neutral and 10% hydrophilic residues and 7 of 23 aa (30%), 14% hydrophobic, 43% neutral and 43% hydrophilic, in the S_7–S_8 loops (Figure 2.1C). The four amino acids residing between residues 139 and 147 predicted to bind p28 are 50% hydrophobic and 50% neutral. These residues and the L_1 and S_7–S_8 loops are not located at or near the DNA-binding surface of p53 (R248 and R273 are direct DNA-binding residues on p53), suggesting p28 does not interfere with the ability of p53 to bind to DNA (Figure 2.1B). The ClusPro best score model also predicted that amino-acid residues LSTAAMQVVGDYLKDD of p28 bind to p53. Fifty per cent of the predicted residues are hydrophobic, again suggesting that hydrophobic rather than electrostatic interaction is essential to the formation of the p28–p53 complex (Figure 2.1B). These results agree with computational docking (*De Grandis et al., 2007*) studies demonstrating that Azurin binds to the L_1 and S_7–S_8 loops of p53 through interaction of non-polar residues at the interface, creating a short-range hydrophobic interaction. A sequence map of the amino acids predicted to be involved in p28 binding and their relationship to the known binding sites of the E3 ubiquitin ligases that negatively regulate p53 is illustrated in Figure 2.1D. p28 does not bind to motifs shown to bind either HDM2 or Pirh2.

GST pull-down assays. p28-binding regions on p53 were mapped using a GST pull-down assay (*Yamada et al., 2009*). GST-$p53_{1–393}$ (full length p53), GST-$p53_{81–300}$ (p53DBD), GST-$p53_{81–160}$ and GST-$p53_{161–300}$ pulled down p28, but the N- (GST-$p53_{1–80}$) and C-terminus of p53 (GST-$p53_{301–393}$) and GST alone did not (Figure 2.2A). These results confirm computerised predictions of regions within the DBD of p53 likely to bind p28 (Figure 2.1A–D). We confirmed that binding motifs for p28 and COP1 overlap using competitive pull-down assays of purified GST-p53 and GST alone in the presence of excess p28. p28 induced a significant concentration-dependent reduction in the amount of COP1 binding to the DBD of p53 (Figure 2.2B). Fine mapping of the regions within the p53DBD revealed that p28 inhibited the binding of COP1 to only GST-$p53_{81–300}$ and GST-$p53_{81–160}$, clearly

demonstrating that p28 inhibits the binding of COP1 to p53 only where their respective binding sites overlap (Figure 2.2C).

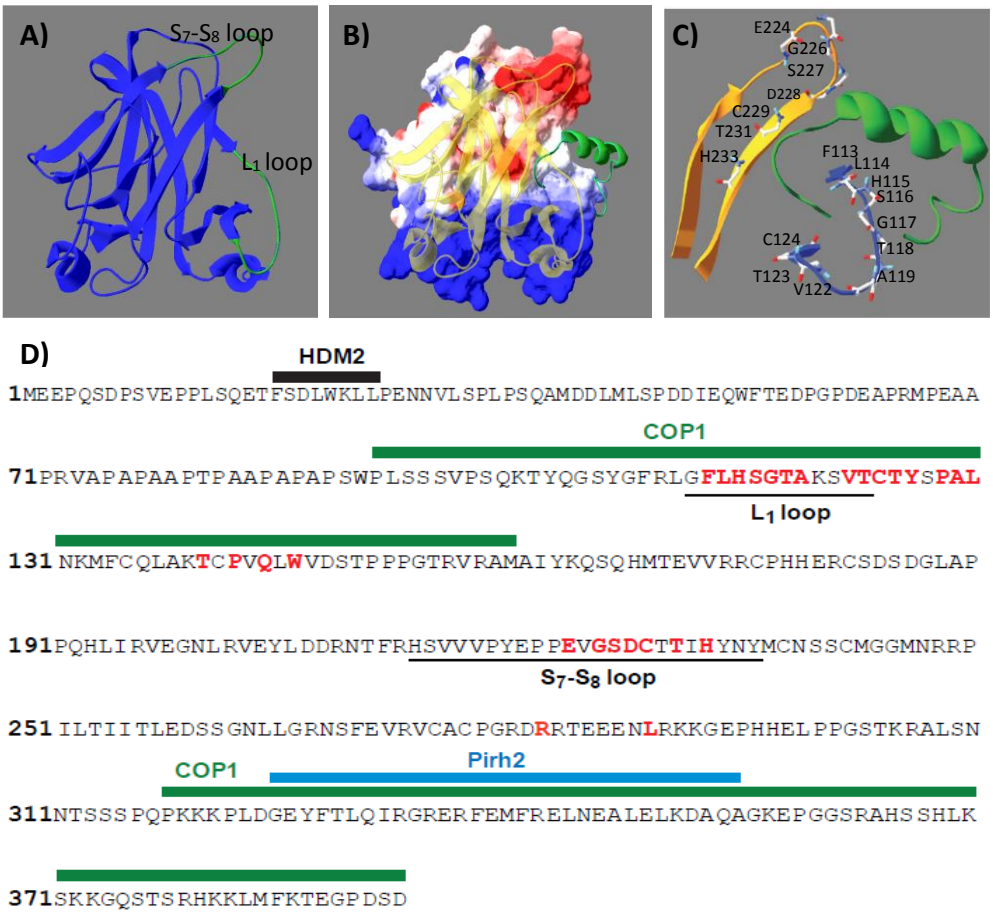

Figure 2.1. Docking model of p28 and p53. (A) The p28–p53 complex structure obtained from the best docking model. Blue: overall ribbon diagram of the p53DBD, green: L_1 and S_7–S_8 loops. **(B)** Ribbon diagram of the p53DBD (yellow) superimposed on the electrostatic potential plot. p28 (green) binds to hydrophobic pocket. **(C)** Relationship of p28 (green) and L_1 (blue) and S_7–S_8 (yellow) loops of the p53DBD. **(D)** Map of E3 ligase binding regions superimposed on the full-length sequence of p53. p28-binding residues indicated in red. Binding regions of HDM2, COP1 and Pirh2 indicated in black, green and blue bars, respectively. COP1 binds to p53 in regions separate from HDM2. p28 and COP1 share a binding motif within aa 92–160 of the p53DBD.

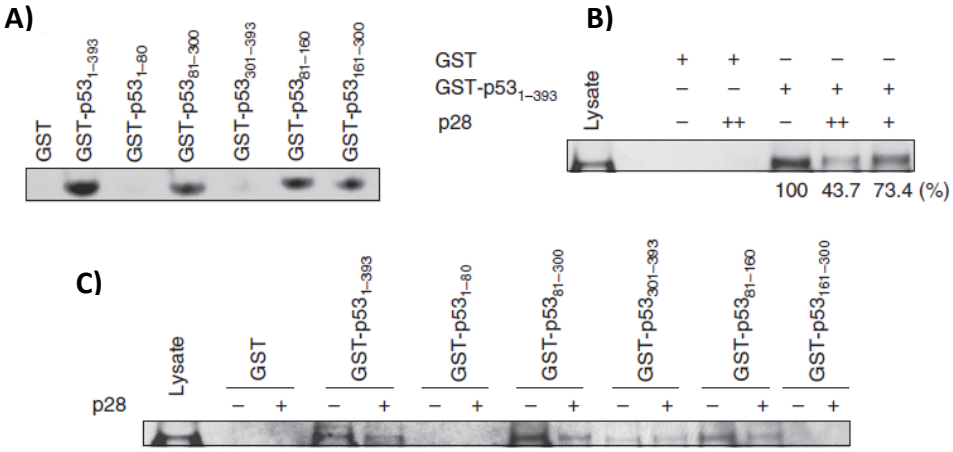

Figure 2.2. p28-binding regions on p53. (A) Purified various fragments of p53 and GST alone were used for a GST pull-down assay. Each sample was analysed by immunoblotting with an anti-p28 antibody. **(B)** Competitive pull-down assay. Immobilised GST-p53$_{1–393}$ and GST alone on glutathione-Sepharose 4B beads were incubated in absence (-) or presence of p28 (+: 10, ++: 100 mole excess), followed by adding MCF-7 lysates containing COP1. Samples were separated by SDS-PAGE and immunoblotted with an anti-COP1 antibody. Lysate: whole-cell lysates of MCF-7 used for the assay showed the stable expression of COP1. Numbers below COP1 bands were relative percentage to the level of COP1 bound to p53 in absence of p28. **(C)** COP1 binding to various fragments of p53 in absence or presence of p28 was analysed using a similar competitive pull-down assay. Immobilized various fragments of p53 and GST alone were treated with or without p28 (100 mole excess), followed by incubation with MCF-7 lysates containing COP1.

Effect of p28 on the growth of human cancer cells. p28 produces a time and dose-related inhibition of p53^{wt} tumour cell and xenograft growth (*Yamada et al., 2009; Jia et al., 2011*). Figure 2.3A shows that a 72-h exposure to p28 at 50 μmol l^{-1} decreased the proliferation of (p53^{wt}) Mel-29 and (p53^{mut}) Mel-23, where p53 is internally deleted at aa 178–183 (*Kichina et al., 2003*), ~25–30% from control. The inhibition was similar to that of 50 μmol l^{-1} DTIC. Neither p28 nor DTIC altered the proliferation of p53^{null} Mel-6 cells. p28 also exhibited significant cytostatic activity on p53^{wt} MCF-7 breast cancer cells with a similar reduction (~20%) in the number of (p53^{mut} R280K) MDA-MB-231 cells after 72 h (Figure 2.3B). These observations, in contrast, p28 did not exhibit an antiproliferative effect on MDD2 (p53$^{dom/neg}$) or normal MCF-10A (p53^{wt}) mammary cells confirming previous results (*Yamada et al, 2009*). Paclitaxel at 50 μmol l^{-1} inhibited the growth of MCF-7 and MDA-MB-231 breast

cancer cells by ~90% and MDD2 ($p53^{dom/neg}$) and MCF-10A ($p53^{wt}$) cells by ~50% and 35%, respectively (Figure 2.3B). p28 also significantly decreased the weight of established $p53^{wt}$ Mel-29 and $p53^{mut}$ Mel-23 xenograft tumours in athymic mice (Figure 2.3C). p28 did not inhibit cell growth of $p53^{null}$ Mel-6 *in vitro* (Figure 2.3A) or *in vivo* (Figure 2.3C). p28 also decreased the weight of MCF-7 ($p53^{wt}$) and MDA-MB-213 ($p53^{mut}$) xenograft tumours by ~50 and 60% respectively, similar to the effect of a non-toxic dose of paclitaxel (*Mi et al., 2002*) (Figure 2.3D).

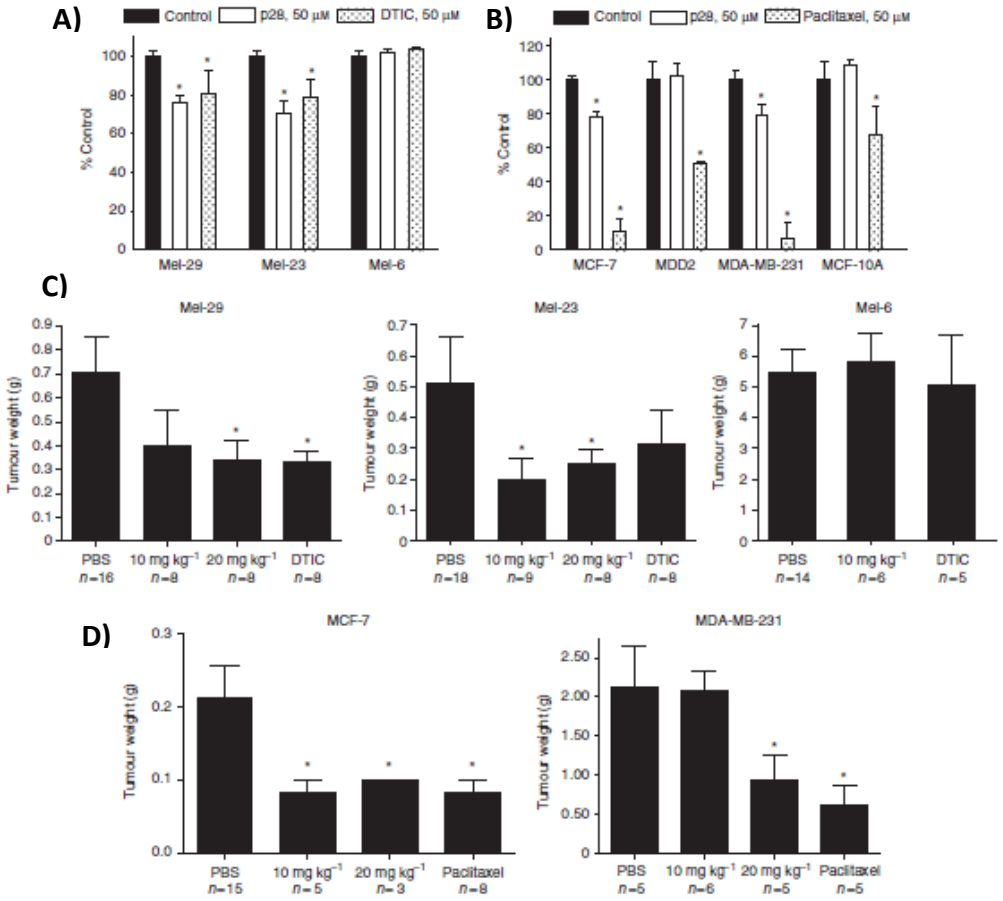

Figure 2.3. The effect of p28 on cell and xenograft growth. Human melanoma UISO-Mel-29, -23 and -6 **(A)** and breast cancer MCF-7, MDD2, MDA-MB-231 and normal MCF-10A cells **(B)** were exposed to p28, DTIC, paclitaxel or a similar volume of media without peptide for 72 h and cells counted. Values represent the mean±s.d. of three replicates. Reduction in Mel-23, 29 xenograft growth **(C).** Reduction of MCF-7, MDA-MB-231 xenograft growth **(D).** *P<0.05.

The significant reduction in growth at 20 mg kg^{-1} and lack of effect at 10 mg kg^{-1} on MDA-MB-231 cells contrast sharply with the similarity in effect for either dose of p28 on $p53^{wt}$ MCF-7, Mel-29 or $p53^{mut}$ Mel-23 cells, suggesting the site of the mutation may be critical to overexpression of p53 (Figure 2.4A and 2.5A) and to the overall effect of p28 on the proliferation of $p53^{mut}$ cancer cells.

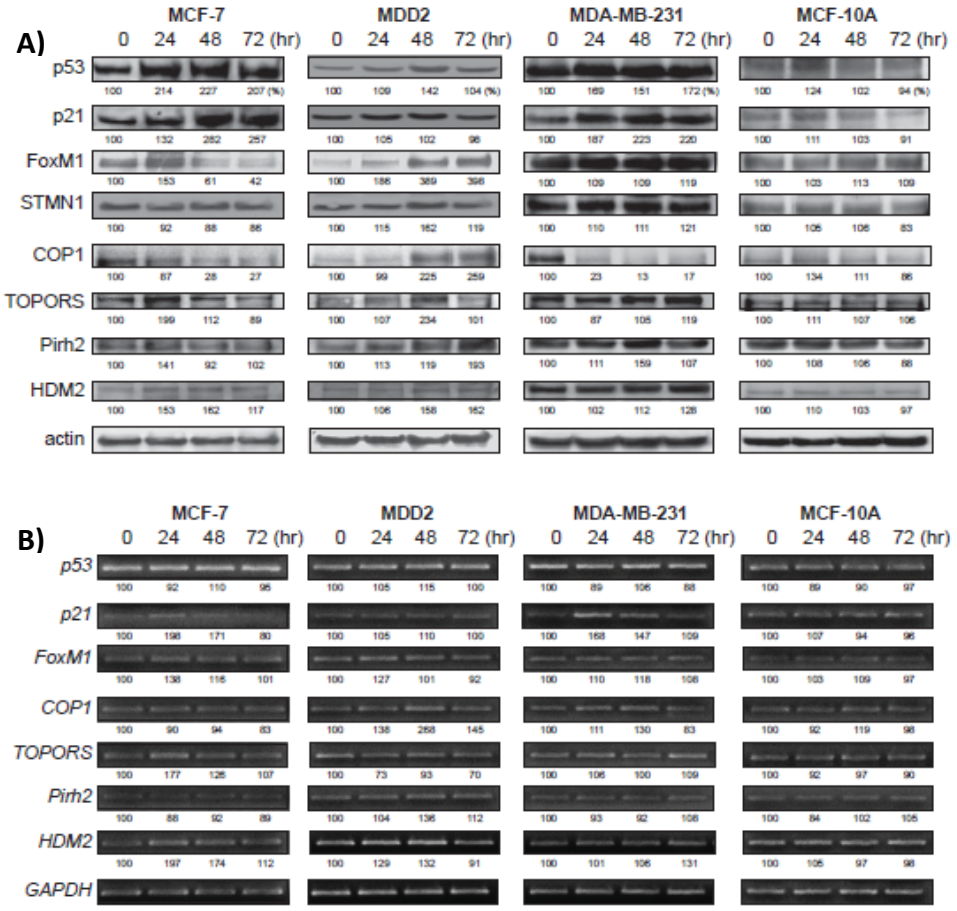

Figure 2.4. Stabilisation of p53 by E3 ligases on $p53^{wt,mut}$ breast cancer cells. (**A)** MCF-7, MDD2, MDA-MB-231, and MCF-10A cells were treated with p28 at 50 µmol l^{-1} for 24–72 h. Whole-cell lysates were subjected to western blot analysis. **(B)** The expression of each gene was determined by RT-PCR. The numbers indicated below each band represent the relative to control (control expressed as 100%).

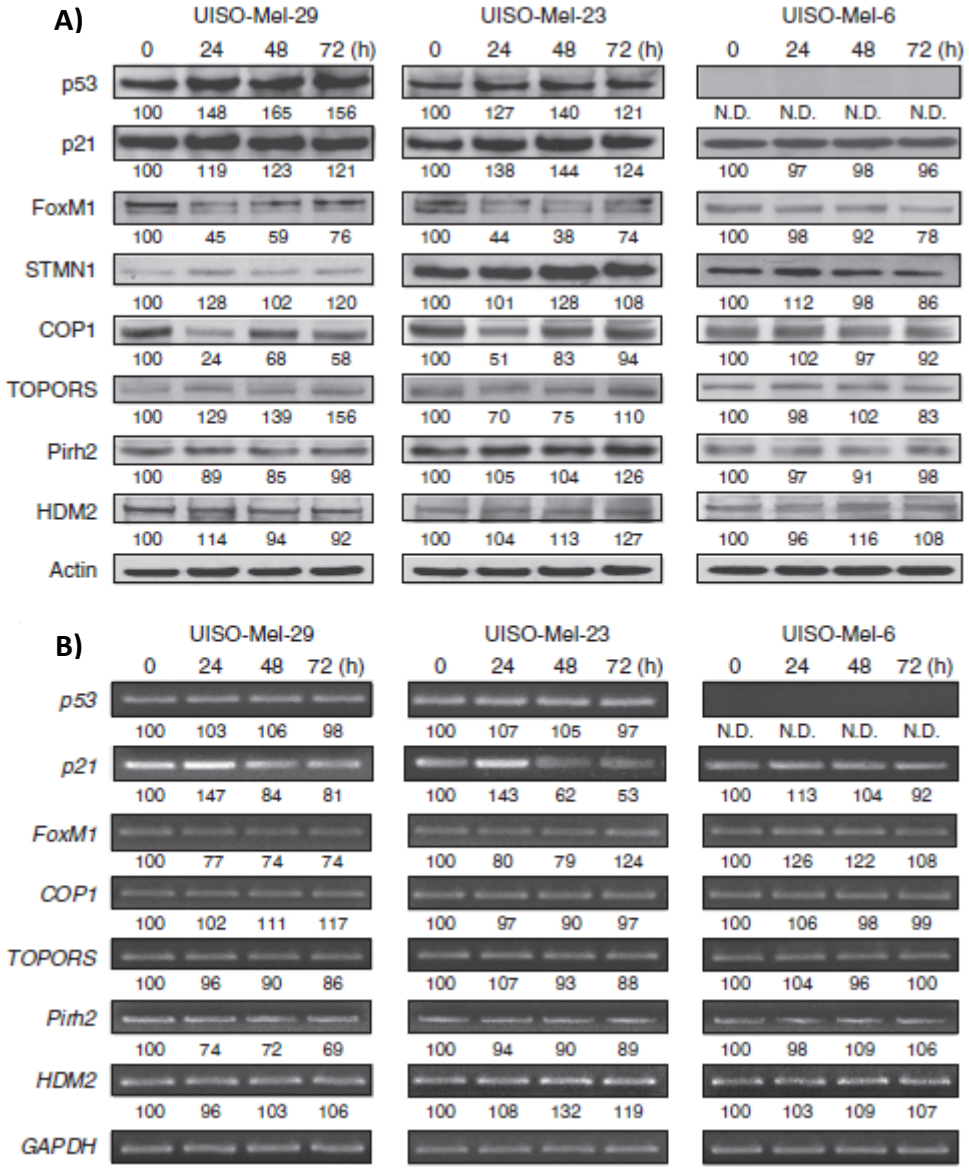

Figure 2.5. Stabilisation of p53 by E3 ligases on p53^{wt,mut} melanoma cells. (A) Mel-29, Mel-23 and Mel-6 cells were treated with p28 at 50 μmol l^{-1} for 24–72 h**. (B)** The expression of each gene was determined by RT-PCR. The numbers indicated below each band represent the relative to control (control expressed as 100%).

p28 Alters the level of p53 and major downstream targets. The significant decrease in growth following exposure to p28 was associated with a sustained increase in the level of p53 in $p53^{wt}$ MCF-7 and $p53^{mut}$ MDA-MB-231 cells (Figure 2.4A) and $p53^{wt}$ Mel-29 and $p53^{mut}$ Mel-23 cells (Figure 2.5A) with no alteration in the level of transcription of p53 (Figure 2.4B and 2.5B), confirming earlier results of an increase in $p53^{wt}$ MCF-7 cells in response to p28 (*Yamada et al., 2009*). The increase in the level of p53 protein in these lines was also directly associated with an increase in the level of transcription and translation of p21. p28 did not alter either the level or rate of transcription of p53 or p21 in $p53^{dom/neg}$ MDD2, $p53^{wt}$ normal MCF-10A or $p53^{null}$ Mel-6 cells (Figure 2.4A and B, and 2.5A and B). Forkhead box M1 protein (FoxM1), an important regulator of the G_2–M transition, was significantly reduced in MCF-7, Mel-29 and Mel-23 cells during exposure to p28, increased in $p53^{dom/neg}$ MDD2 cells at 48–72 h, and remained essentially unchanged in MDA-MB-231, MCF-10A and Mel-6 cells, suggesting that downregulation of FoxM1 also contributed to inhibition of the cell cycle in $p53^{wt}$ MCF-7, Mel-29 and $p53^{mut}$ Mel-23 cells. Although this may result from an inability of $p53^{mut}$ to bind the p53 canonical consensus regions in the FOXM1 promoter, p21 levels were sufficiently elevated to inhibit the proliferation of $p53^{mut}$ MDA-MB-231 cells, despite the overexpression of FoxM1 (Figure 2.4A) (*Bektas et al., 2008*). This is not surprising because p53 mutants can often transactivate promoters containing a p21 responsive element (*Campomenosi et al., 2001*) and loss of function in mutant p53 breast tumours does not represent a complete absence of activity (*Williams et al., 1998*). STMN1, an inhibitor of microtubule polymerisation (*Belmont and Mitchison, 1996*) and critical for cell cycle progression, was not significantly decreased in any cancer cell line tested (Figure 2.4A and 2.5A), suggesting p28 inhibition of the cell cycle at G_2–M is at G_2 and does not involve inhibition of microtubule formation.

The p28-induced increase in p53 was associated with a significant decrease in the levels of COP1 in $p53^{wt}$ and $p53^{mut}$ breast cancer and melanoma cells (Figure 2.4A and 2.5A). Exposure of $p53^{wt}$ MCF-7 and $p53^{mut}$ MDA-MB-231 cells to p28 reduced COP1 levels by ~70% and 80%, respectively, over 24–72 h without altering the transcription of COP1 (Figure 2.4A). Exposure of $p53^{wt}$ Mel-29 to p28 significantly reduced COP1 levels (~75%) at 24 h that gradually increased (~60% of control) at 72 h (Figure 2.5A). A similar effect on COP1 levels was observed in $p53^{mut}$ Mel-23 cells. The lack of effect of p28 on COP1 levels in $p53^{null}$ Mel-6 and delayed increase in $p53^{dom/neg}$ MDD2 exposed to p28 suggest that the effects

of p28 on COP1 are a function of a cell's p53 status. Moreover, as continued exposure to p28 does not significantly alter COP1 transcription in $p53^{wt}$ and $p53^{mut}$ cancer cells, the decrease in the overall level of COP1 likely occurs through autodegradation (*Dornan et al., 2006*).

p28 Effects on minor E3 ubiquitin ligases. p28 produces a posttranslational increase in p53 through decreased ubiquitination and proteasomal degradation rather than transcriptional activation (*Yamada et al., 2009*). However, exposure to p28 transiently increased the transcription and level of TOPORS (48 h) in $p53^{wt}$ MCF-7 cells, but did not significantly affect either the transcription or level of TOPORS in $p53^{mut}$ MDA-MB-231 cells (Figure 2.4A and B). This suggests the upregulation of TOPORS by wild-type p53 was more efficient than with mutated p53. Exposure of $p53^{wt}$ Mel- 29 cells to p28 produced a sustained increase in the level of TOPORS that was not transcription dependent, whereas exposure of $p53^{mut}$ Mel-23 cells to p28 reduced the level of TOPORS over 48 h, which was not preceded or accompanied by a change in transcription (Figure 2.5 A and B). The increase in the level and transcription of TOPORS in $p53^{wt}$ MCF-7 and Mel-29 cells and lack of effect on $p53^{mut}$ MDA-MB-231 and Mel-23 cells suggest that changes in the level of TOPORS in response to p28 are dependent on p53 status and do not have a major role in the regulation of cell proliferation.

p28 also induced a short-term (24 h) increase in the level of Pirh2 in $p53^{wt}$ MCF-7 and MDA-MB-231 cells without an accompanying increase in transcription, suggesting that the transient increase was in response to the p28-induced increase in p53 (Figure 2.4A and B). In contrast, p28 had no significant effect on the expression of the Pirh2 protein or transcription in $p53^{wt}$ Mel-29 or $p53^{mut}$ Mel-23 cells (Figure 2.5A and B). Collectively, changes in the level of TOPORS and Pirh2 appeared dependent on the cell line treated as well as p53 status and are a minor factor in the regulation of wild-type or mutated p53.

In contrast, the initial increase (24–48 h) and slow rise (72 h) in the level of the major E3 ligase HDM2 in $p53^{wt}$ MCF-7 and $p53^{mut}$ MDA-MB-231 cells, respectively, was accompanied by a parallel increase in transcription. However, neither increase reflected the sustained increase in p53 in response to p28. Unlike COP1, HDM2 levels were not significantly altered by p28 in $p53^{wt}$ Mel-29 cells, but increased late in exposure (48–72 h) in $p53^{mut}$ Mel-23 (Figure 2.5A).

p28 Effect on c-Jun. If COP1 acts as a developmentally dependent tumour suppressor (*Migliorini et al., 2011; Vitari et al., 2011*), interacting with the oncoprotein c-Jun (*Bianchi et al., 2003*) to keep c-Jun at constitutively low levels in vivo and COP1 deficiency leads to c-Jun upregulation in human cancer cells (*Migliorini et al., 2011*) even in the absence of a genetic interaction between COP1 and p53 (*Migliorini et al., 2011*), then exposure to p28 should significantly increase c-Jun levels in $p53^{wt,mut,null}$ cells. p28 did not significantly alter the level of c-Jun in either $p53^{wt}$ MCF-7, MDD2 or MCF-10A cells and transiently (48 h) reduced (38%) c-Jun levels in $p53^{mut}$ MDA-MB-231 breast cancer cells (Figure 2.6A).

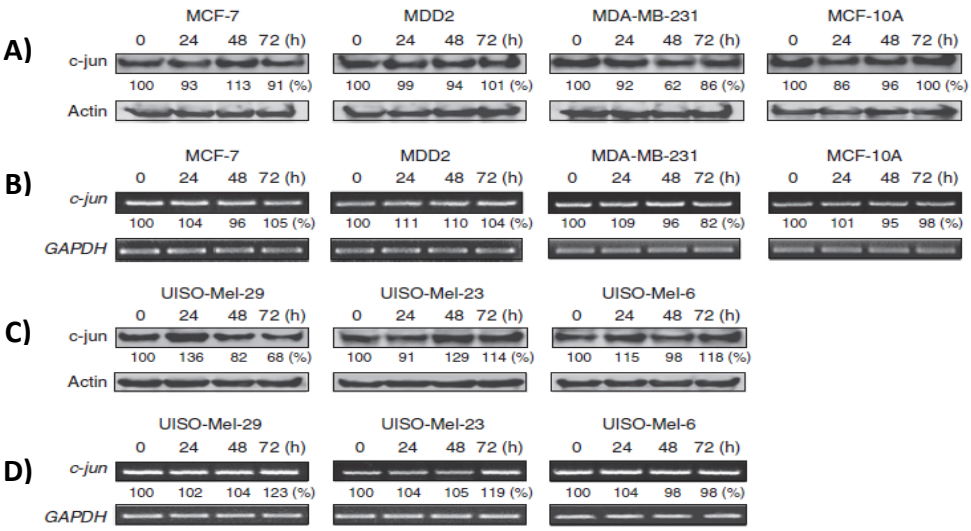

Figure 2.6. The effect of p28 on c-Jun. The protein level of c-Jun was determined in MCF-7, MDD2, MDA-MB-231 and MCF-10A cells **(A),** and Mel-29, Mel-23 and Mel-6 **(C)** treated with p28 at 50 μmol l^{-1} for 24–72 h. The transcription level of c-Jun was determined by RT-PCR in breast cell lines **(B)** and melanoma cells **(D).** The numbers indicated below each band represent the relative to control (control expressed as 100%).

In contrast, c-Jun was significantly decreased over 48–72 h in $p53^{wt}$ Mel-29 cells, briefly increased (48 h) in $p53^{mut}$ Mel-23 cells, and only increased slightly over 24 h in $p53^{null}$ Mel-6 cells (Figure 2.6C). The decrease in c-Jun in $p53^{wt}$ Mel-29 cells was accompanied by an increase in transcription (72 h), suggesting the increase was in response to the decrease in the level of the c-Jun protein (Figure 2.6B and D) rather than the result of a decrease in COP1

following exposure to p28. None of these results suggest that a sustained decrease in COP1 results in an increase in the level and transcription of c-Jun (*Migliorini et al., 2011*).

Moreover, the absence of any change in p53, COP1, p21, FOXM1, TORPORS, Pirh2 or HDM2 and the transient increase in c-Jun in $p53^{null}$ Mel-6 cells in response to p28 suggest that the antiproliferative effects of p28 are mediated via the sustained increase in p53 and p21 independent of any effect on c-Jun (*Migliorini et al., 2011*).

Discussion

Although most wild-type or mutated p53 tumours must certainly be dysfunctional (*Wiman, 2006*), cancer cells proliferate irrespective of p53 status. This suggests reactivation of p53-induced control of the cell cycle and apoptosis is a plausible therapeutic goal regardless of p53 status. The loss of wild-type p53 function or gain of new oncogenic properties may result, in part, from the numerous missense point mutations within the DBD of p53 clustered into discrete hot spots (R175, G245, R248, R249, R273 and R282) (*Tu et al., 2008*). However, the reported gain-of-function properties reportedly associated with p53 hot spot mutations may not be a universal phenomenon (*Lee et al., 2012*). Amino-acid residues R248 and R273 directly contact DNA while the remainder stabilizes the structure of the DNA-binding motif within the DBD (*Tu et al., 2008*). In contrast, the flexible L_1 loop (aa 112–124) within the p53DBD is a mutational cold spot (*Zupnick and Prives, 2006*). Our models predicted that p28 would bind to the L_1 loop, a region of the S_7–S_8 loop (aa 214–236) and T140, P142, Q144, W146, R282 and L289 of the p53DBD. This prediction was supported by GST pull-down assays (Figure 2.2A) and atomic force spectroscopy studies that indicated p28 binds with high affinity to the p53DBD (*Bizzarri et al., 2011*).

Once bound, p28 produces an increase in the level of $p53^{wt,mut}$ (Figure 2.4A and 2.5A), which is associated with an inhibition of cell proliferation in vitro and in vivo (Figure 2.3A–D). Neither the internal in frame deletion (aa 178–183) (*Kichina et al., 2003*) in p53 in Mel-23 cells, which does not include the predicted binding sites for p28, nor the point mutation at R280K in MDA-MB-231 cells that leads to overexpression (*Olivier et al., 2002*) (Figure 2.4A) affects the binding of p28. This suggests that increasing an already elevated level of mutated p53 may also positively impact downstream targets within the cell cycle and apoptotic pathways (*Ludwig et al., 1996; Campomenosi et al., 2001*).

The FoxM1, a transcription factor for genes regulating the G_2–M transition, is a major downstream target of p53 (*Laoukili et al, 2005*). Loss of FoxM1 leads to a delay in G_2 (*Laoukili et al, 2005*). p28 reduced the level of FoxM1 in $p53^{wt}$ MCF-7, $p53^{wt}$ Mel-29 and $p53^{mut}$ Mel-23 cells and inhibited cell proliferation, but did not reduce the high basal levels of FoxM1 in triple negative (ER^-, PGR^-, $HER2^-$) $p53^{mut}$ MDA-MB-231 cells (Figure 2.4A). The significant inverse correlation between FoxM1 expression and human epidermal growth factor 2 (HER2) (*Bektas et al., 2008*) suggests overexpression of FoxM1 may result from this interaction or that the $p53^{mut}$ R280K in MDA-MB-231 cells may not allow binding to the promoter region of FoxM1. However, p28 did increase the level of p21 in $p53^{mut}$ MDA-MB-231 cells (Figure 2.4A), in turn inhibiting the activity of the cyclin–CDK2 complex (*Yamada et al., 2009*). This suggests that inhibition of CDK by p21 provided an alternative pathway for the reduction in growth in the absence of a reduction in FoxM1.

Intracellular levels of p53 are tightly regulated by a series of ubiquitin E3 ligases that promote ubiquitination and proteasome dependent degradation of p53 (*Michael and Oren, 2003*). HDM2 or MDM2 is the major E3 ligase promoting p53 degradation (*Haupt et al., 1997; Kubbutat et al., 1997*), but TOPORS, Pirh2 and particularly COP1 also bind to and negatively regulate p53 (*Leng et al., 2003; Dornan et al., 2004b; Rajendra et al., 2004*). Although TOPORS is expressed in most normal human tissues (*Saleem et al., 2004*), it is not expressed in colon cancer (*Rajendra et al., 2004*) and may not be an E3 ligase critical to p53 function in malignant cells. In contrast, Pirh2 expression is lower in normal compared with tumour cells and appears independent of the type of p53 mutation (*Duan et al., 2006*). The C-terminal domain of Pirh2 (aa 190–261) binds primarily to the tetramerisation domain (aa 325–355) of p53 (*Sheng et al., 2008*) well removed from the binding sites for p28. Exposure to p28 did not reduce Pirh2 levels in either breast cancer or melanoma cells (Figure 2.4 and 2.5), producing only short-term increases that were not accompanied by an increase in transcription. This suggests that only extant Pirh2 was recruited to degrade the increasing levels of p53.

p28 significantly increased the level and transcription of HDM2 in $p53^{wt}$ MCF-7 cells over 24–72 h, while p53 levels remained elevated (Figure 2.4). The increase in HDM2 was minimal and delayed (72 h) in $p53^{mut}$ MDA-MB-231 cells. p28 had essentially no effect on HDM2 levels or transcription in $p53^{wt}$ Mel-29, and induced only a delayed increase in HDM2 protein and RNA levels in $p53^{mut}$ Mel-23 cells in spite of a sustained increase in p53 levels in both cell lines.

COP1 is overexpressed in breast and ovarian cancers (*Dornan et al., 2004b*), promotes p53 degradation via the proteasome pathway independently of HDM2 or Pirh2 (*Dornan et al., 2004b*) and is able to ubiquitinate itself (*Bianchi et al., 2003; Dornan et al., 2006*). We confirm that COP1 binds to aa 92–160 and aa 318–393 of p53 (*Li et al., 2009*). We show that p28 binds to specific motifs within the COP1-binding regions of the p53DBD, blocking COP1 binding and the subsequent ubiquitination and proteasomal degradation of p53. These motifs are distinct (Figure 2.1D) from those binding HDM2. The significant reduction in COP1 levels in breast cancer and melanoma cells (Figure 2.4 and 2.5) is not accompanied by an increase in the transcription of COP1 message, indicating the loss in COP1 is through autodegradation (*Dornan et al., 2006*). The p28-induced reduction in COP1 levels was also not accompanied by a significant or sustained increase in the transcription in c-Jun levels (*Migliorini et al., 2011*) that would be expected if a decrease in COP1 levels led to upregulation of c-Jun or altered its ubiquitination. Similarly, overexpression of COP1 does not result in a decrease in steady-state levels of c-Jun nor reduce c-Jun half-life (*Bianchi et al., 2003*).

The slight, transient increases and decreases in c-Jun levels were also unrelated to alterations in the expression of p53 or in c-Jun transcription (Figure 2.6) (*Migliorini et al., 2011*), and may result from as yet unknown modulating effects on the steady-state condition of c-Jun in individual cell lines as a result of exposure to p28. The sustained decrease in COP1 levels induced by p28 did not result in a c-Jun-dependent increase in cell proliferation (Figure 2.3) (*Migliorini et al., 2011*), again suggesting that a pharmacologically induced reduction in COP1 levels does not result in a c-Jun mediated increase in tumour cell proliferation in either $p53^{wt}$ or $p53^{mut}$ cancers (*Migliorini et al., 2011*).

On the basis of our findings, we propose a model for the stabilisation of p53 by p28 that results in a reduction in tumour growth through regulation of cell cycle-related genes. p28 binds to the L_1 loop (aa 112–124) and additional motifs within the COP1-binding regions of the p53DBD (Figure 2.1D), subsequently inhibiting COP1-mediated p53 proteasomal degradation and stabilising p53. Increased levels of p53 upregulate the downstream molecules p21 (Figure 2.4A and 2.5A) and p27 (*Yamada et al., 2009*) in $p53^{wt}$ and, at least some, $p53^{mut}$ cancer cells, downregulating FoxM1, and leading to inhibition of cell cycle at G_2–M.

Currently, small molecules designed to inhibit HDM2-mediated ubiquitination are apparently only being tested in patients with $p53^{wt}$ tumours (*Kojima et al., 2010*). Unlike these small

molecules, p28 preferentially enters wide variety of cancer cells (*Taylor et al., 2009*) and enhances the cellular level of $p53^{wt,mut}$ by inhibiting the binding of COP1 independent of the HDM2 pathway. As such, p28 is a prototype molecule that exhibits efficacy in patients with advanced (Stage IV) $p53^{wt,mut}$ solid tumours (*Warso et al., 2013*).

Supplementary Information accompanies this paper on British Journal of Cancer website (http://www.nature.com/bjc).

References

Apiyo D, Wittung-Stafshede P. 2005. Unique complex between bacterial azurin and tumor-suppressor protein p53. *Biochem. Biophys. Res. Commun.* **332**: 965–968.

Bektas N, Haaf A, Veeck J, Wild PJ, Luscher-Firzlaff J, Hartmann A, Knuchel R, Dahl E. 2008. Tight correlation between expression of the Forkhead transcription factor FOXM1 and HER2 in human breast cancer. *BMC Cancer* **8**: 42.

Belmont LD, Mitchison TJ. 1996. Identification of a protein that interacts with tubulin dimers and increases the catastrophe rate of microtubules. *Cell* **84**: 623–631.

Bianchi E, Denti S, Catena R, Rossetti G, Polo S, Gasparian S, Putignano S, Rogge L, Pardi R. 2003. Characterization of human constitutive photomorphogenesis protein 1, a RING finger ubiquitin ligase that interacts with Jun transcription factors and modulates their transcriptional activity. *J. Biol. Chem.* **278**: 19682-19690.

Bizzarri AR, Cannistraro S. 2009. Atomic force spectroscopy in biological complex formation: strategies and perspectives. *J. Phys. Chem. B* **113**: 16449–16464.

Bizzarri AR, Di Agostino S, Andolfi L, Cannistraro S. 2009. A combined atomic force microscopy imaging and docking study to investigate the complex between p53 DNA binding domain and Azurin. *J. Mol. Recognit.* **22**: 506–515.

Bizzarri AR, Santini S, Coppari E, Bucciantini M, Di Agostino S, Yamada T, Beattie CW, Cannistraro S. 2011. Interaction of an anticancer peptide fragment of azurin with p53 and its isolated domains studied by atomic force spectroscopy. *Int. J. Nanomedicine* **6**: 3011–3019.

Campomenosi P, Monti P, Aprile A, Abbondandolo A, Frebourg T, Gold B, Crook T, Inga A, Resnick MA, Iggo R, Fronza G. 2001. p53 mutants can often transactivate promoters containing a p21 but not Bax or PIG3 responsive elements. *Oncogene* **20**: 3573–3579.

Chan WM, Mak MC, Fung TK, Lau A, Siu WY, Poon RYC. 2006. Ubiquitination of p53 at multiple sites in the DNA-binding domain. *Mol. Cancer Res*. **4**: 15–25.

Chen D, Kon N, Li M, Zhang W, Qin J, Gu W. 2005. ARF-BP1/Mule is a critical mediator of the ARF tumor suppressor. *Cell* **121**: 1071–1083.

Cheok CF, Verma CS, Baselga J, Lane DP. 2011. Translating p53 into the clinic. *Nat. Rev. Clin. Oncol.* **8**: 25–37.

Cho Y, Gorina S, Jeffrey PD, Pavletich NP. 1994. Crystal structure of a p53 tumor suppressor–DNA complex: understanding tumorigenic mutations. *Science* **265**: 346–355.

Corcoran C, Huang Y, Sheikh M. 2004. The p53 paddy wagon: COP1, Pirh2 and MDM2 are found resisting apoptosis and growth arrest. *Cancer Biol. Ther*. **3**: 721–725.

De Grandis V, Bizzarri AR, Cannistraro S. 2007. Docking study and free energy simulation of the complex between p53 DNA-binding domain and azurin. *J. Mol. Recognit.* **20**: 215–226.

Dornan D, Bheddah S, Newton K, Ince W, Frantz GD, Dowd P, Koeppen H, Dixit VM, French DM. 2004a. COP1, the negative regulator of p53, is overexpressed in breast and ovarian adenocarcinomas. *Cancer Res*. **64**: 7226–7230.

Dornan D, Wertz I, Shimizu H, Arnott D, Frantz GD, Dowd P, O'Rourke K, Koeppen H, Dixit VM. 2004b. The ubiquitin ligase COP1 is a critical negative regulator of p53. *Nature* **429**: 86–92.

Dornan D, Shimizu H, Mah A, Dudhela T, Eby M, O'Rourke K, Seshagiri S, Dixit VM. 2006. ATM engages autodegradation of the E3 ubiquitin ligase COP1 after DNA damage. *Science* **313**: 1122–1126.

Duan W, Gao L, Wu X, Zhang Y, Otterson GA, Villalona-Calero MA. 2006. Differential response between the p53 ubiquitin-protein ligases Pirh2 and MdM2 following DNA damage in human cancer cells. *Exp. Cell Res.* **312**: 3370–3378.

Haupt Y, Maya R, Kazaz A, Oren M. 1997. MDM2 promotes the rapid degradation of p53. *Nature* **387:** 296–299.

Hosaka M, Watanabe T, Sakai Y, Kato T, Takeuchi T . 2005. Interaction between secretogranin III and carboxypeptidase E facilitates prohormone sorting within secretory granules. *J. Cell Sci.* **118** (Part 20): 4785–4795.

Jia L, Gorman GS, Coward LU, Noker PE, McCormick D, Horn TL, Harder JB, Muzzio M, Prabhakar B, Ganesh B, Das Gupta TK, Beattie CW. 2011. Preclinical pharmacokinetics, metabolism, and toxicity of azurin-p28 (NSC745104) a peptide inhibitor of p53 ubiquitination. *Cancer Chemother. Pharmacol.* **68**: 513–524.

Kichina JV, Rauth S, Das Gupta TK, Gudkov AV. 2003. Melanoma cells can tolerate high levels of transcriptionally active endogenous p53 but are sensitive to retrovirus-transduced p53. *Oncogene* **22**: 4911–4917.

Kojima K, Burks JK, Arts J, Andreeff M. 2010. The novel tryptamine derivative JNJ-26854165 induces wild-type p53- and E2F1-mediated apoptosis in acute myeloid and lymphoid leukemias. *Mol. Cancer. Ther.* **9**: 2545–2557.

Kozakov D, Hall DR, Beglov D, Brenke R, Comeau SR, Shen Y, Li K, Zheng J, Vakili P, Paschalidis I, Vajda S. 2010. Achieving reliability and high accuracy in automated protein docking: ClusPro, PIPER, SDU, and stability analysis in CAPRI rounds 13-19. *Proteins* **78**: 3124–3130.

Kubbutat MH, Jones SN, Vousden KH. 1997. Regulation of p53 stability by Mdm2. *Nature* **387**: 299–303.

Laoukili J, Kooistra MR, Bras A, Kauw J, Kerkhoven RM, Morrison A, Clevers H, Medema RH. 2005. FoxM1 is required for execution of the mitotic programme and chromosome stability. *Nat. Cell. Biol.* **7**: 126–136.

Lee MK, Teoh WW, Phang BH, Tong WM, Wang ZQ, Sabapathy K. 2012. Cell-type, dose, and mutation-type specificity dictate mutant p53 functions in vivo. *Cancer Cell* **22**: 751–764.

Lee YH, Andersen JB, Song HT, Judge AD, Seo D, Ishikawa T, Marquardt JU, Kitade M, Durkin ME, Raggi C, Woo HG, Conner EA, Avital I, Maclachlan I, Factor VM, Thorgeirsson SS. 2010. Definition of ubiquitination modulator COP1 as a novel therapeutic target in human hepatocellular carcinoma. *Cancer Res.* **70**: 8264–8269.

Leng RP, Lin Y, Ma W, Wu H, Lemmers B, Chung S, Parant JM, Lozano G, Hakem R, Benchimol S. 2003. Pirh2, a p53-induced ubiquitin-protein ligase, promotes p53 degradation. *Cell* **112**: 779–791.

Li DQ, Divijendra Natha Reddy S, Pakala SB, Wu X, Zhang Y, Rayala SK, Kumar R. 2009. MTA1 coregulator regulates p53 stability and function. *J. Biol. Chem.* **284**: 34545–34552.

Li YF, Wang DD, Zhao BW, Wang W, Huang CY, Chen YM, Zheng Y, Keshari RP, Xia JC, Zhou ZW. 2012. High level of COP1 expression is associated with poor prognosis in primary gastric cancer. *Int. J. Biol. Sci.* **8**: 1168–1177.

Ludwig RL, Bates S, Vousden KH. 1996. Differential activation of target cellular promoters by p53 mutants with impaired apoptotic function. *Mol. Cell. Biol.* **16**: 4952–4960.

Mehta RR, Yamada T, Taylor BN, Christov K, King ML, Majumdar D, Lekmine F, Tiruppathi C, Shilkaitis A, Bratescu L, Green A, Beattie CW, Das Gupta TK. 2011. A cell penetrating peptide derived from azurin inhibits angiogenesis and tumor growth by inhibiting phosphorylation of VEGFR-2, FAK and Akt. *Angiogenesis* **14**: 355–369.

Mi Q, Lantvit D, Reyes-Lim E, Chai H, Zhao W, Lee IS, Peraza-Sanchez S, Ngassapa O, Kardono LB, Riswan S, Hollingshead MG, Mayo JG, Farnsworth NR, Cordell GA, Kinghorn AD, Pezzuto JM. 2002. Evaluation of the potential cancer chemotherapeutic efficacy of natural product isolates employing in vivo hollow fiber tests. *J. Nat. Prod.* **65**: 842–850.

Michael D, Oren M. 2003. The p53-Mdm2 module and the ubiquitin system. *Semin. Cancer Biol.* **13**: 49–58.

Migliorini D, Bogaerts S, Defever D, Vyas R, Denecker G, Radaelli E, Zwolinska A, Depaepe V, Hochepied T, Skarnes WC, Marine JC. 2011. Cop1 constitutively regulates c-Jun protein stability and functions as a tumor suppressor in mice. *J. Clin. Invest.* **121**: 1329–1343.

Olivier M, Eeles R, Hollstein M, Khan MA, Harris CC, Hainaut P. 2002. The IARC TP53 database: new online mutation analysis and recommendations to users. *Hum. Mutat*. **19**: 607–614.

Punj V, Bhattacharyya S, Saint-Dic D, Vasu C, Cunningham EA, Graves J, Yamada T, Constantinou AI, Christov K, White B, Li G, Majumdar D, Chakrabarty AM, Das Gupta TK. 2004. Bacterial cupredoxin azurin as an inducer of apoptosis and regression in human breast cancer. *Oncogene* **23**: 2367–2378.

Rajendra R, Malegaonkar D, Pungaliya P, Marshall H, Rasheed Z, Brownell J, Liu LF, Lutzker S, Saleem A, Rubin EH. 2004. Topors functions as an E3 ubiquitin ligase with specific E2 enzymes and ubiquitinates p53. *J. Biol .Chem.* **279**: 36440–36444.

Reynolds C, Damerell D, Jones S. 2009. ProtorP: a protein-protein interaction analysis server. *Bioinformatics* **25**: 413–414.

Saleem A, Dutta J, Malegaonkar D, Rasheed F, Rasheed Z, Rajendra R, Marshall H, Luo M, Li H, Rubin EH. 2004. The topoisomerase I- and p53- binding protein topors is differentially expressed in normal and malignant human tissues and may function as a tumor suppressor. *Oncogene* **23**: 5293–5300.

Santini S, Bizzarri AR, Cannistraro S. 2011. Modelling the interaction between the p53 DNA-binding domain and the p28 peptide fragment of azurin. *J. Mol. Recognit.* **24**:1043–1055.

Shaulian E, Zauberman A, Ginsberg D, Oren M. 1992. Identification of a minimal transforming domain of p53: negative dominance through abrogation of sequence-specific DNA binding. *Mol. Cell. Biol.* **12**: 5581–5592.

Sheng Y, Laister RC, Lemak A, Wu B, Tai E, Duan S, Lukin J, Sunnerhagen M, Srisailam S, Karra M, Benchimol S, Arrowsmith CH. 2008. Molecular basis of Pirh2-mediated p53 ubiquitylation. *Nat. Struct. Mol. Biol.* **15**:1334–1342.

Taranta M, Bizzarri AR, Cannistraro S. 2008. Probing the interaction between p53 and the bacterial protein azurin by single molecule force spectroscopy. *J. Mol. Recognit.* **21**: 63–70.

Taylor BN, Mehta RR, Yamada T, Lekmine F, Christov K, Chakrabarty AM, Green A, Bratescu L, Shilkaitis A, Beattie CW, Das Gupta TK. 2009. Noncationic peptides obtained from azurin preferentially enter cancer cells. *Cancer Res.* **69**: 537–546.

Tu C, Tan YH, Shaw G, Zhou Z, Bai Y, Luo R, Ji X. 2008. Impact of low frequency hotspot mutation R282Q on the structure of p53 DNA-binding domain as revealed by crystallography at 1.54 angstroms resolution. *Acta Crystallogr. D Biol. Crystallogr.* **64**(Pt 5): 471–477.

Vitari AC, Leong KG, Newton K, Yee C, O'Rourke K, Liu J, Phu L, Vij R, Ferrando R, Couto SS, Mohan S, Pandita A, Hongo JA, Arnott D, Wertz IE, Gao WQ, French DM, Dixit VM. 2011. COP1 is a tumour suppressor that causes degradation of ETS transcription factors. *Nature* **474**: 403–406.

Wang L, He G, Zhang P, Wang X, Jiang M, Yu L. 2011. Interplay between MDM2, MDMX, Pirh2 and COP1: the negative regulators of p53. *Mol. Biol. Rep.* **38**: 229–236.

Warso MA, Richards JM, Mehta D, Christov K, Schaeffer C, Rae Bressler L, Yamada T, Majumdar D, Kennedy SA, Beattie CW, Das Gupta TK. 2013. A first-in-class, first-in-human, phase I trial of p28, a non-HDM2- mediated peptide inhibitor of p53 ubiquitination in patients with advanced solid tumours. *Br. J. Cancer* **108**: 1061–1070.

Williams C, Norberg T, Ahmadian A, Ponten F, Bergh J, Inganas M, Lundeberg J, Uhlen M. 1998. Assessment of sequence-based p53 gene analysis in human breast cancer: messenger RNA in comparison with genomic DNA targets. *Clin. Chem.* **44**: 455–462.

Wiman KG. 2006. Strategies for therapeutic targeting of the p53 pathway in cancer. *Cell Death Differ.* **13**: 921–926.

Yamada T, Goto M, Punj V, Zaborina O, Chen ML, Kimbara K, Majumdar D, Cunningham E, Das Gupta TK, Chakrabarty AM. 2002. Bacterial redox protein azurin, tumor suppressor protein p53, and regression of cancer. *Proc. Natl. Acad. Sci. USA* **99**: 14098–14103.

Yamada T, Fialho AM, Punj V, Bratescu L, Gupta TK, Chakrabarty AM. 2005. Internalization of bacterial redox protein azurin in mammalian cells: entry domain and specificity. *Cell Microbiol.* **7**: 1418–1431.

Yamada T, Mehta RR, Lekmine F, Christov K, King ML, Majumdar D, Shilkaitis A, Green A, Bratescu L, Beattie CW, Das Gupta TK. 2009. A peptide fragment of azurin induces a p53-mediated cell cycle arrest in human breast cancer cells. *Mol. Cancer. Ther.* **8**: 2947–2958.

Zupnick A, Prives C. 2006. Mutational analysis of the p53 core domain L1 loop. *J. Biol. Chem.* **281**: 20464–20473.

Chapter 3

Study of the interaction between p28 and both physiological and non physiological p53 DBD mutants

Once the p28 binding region on p53 was determined and its mode of action was disclosed, the successive step has been the investigation of its interaction with mutated forms of the p53DBD in order to get insight into the possible correlation existing between mutations induced DBD conformational changes, hydrophobicity degree of the DBD surface involved in the interaction with p28, the p28 binding capability and affinity, as well its biological activity. To this aim, a multidisciplinary approach has been used in which the kinetic information on the p28/DBD mutants interaction that I have obtained by Atomic Force Spectroscopy studies, have integrated results from computational docking approach (by the group of Prof. Beattie, Department of Surgical Oncology, Illinois University, Chicago) and Raman spectroscopy experiments (performed by Prof. Cannistraro group, Biophysics and Nanoscience Center, University of Tuscia, Viterbo). All data have been here gathered for a global vision of the obtained results.

Introduction

The Azurin derived fragment p28 binds with high affinity to the DBD of p53 (*Bizzarri et al., 2011*) without altering its conformation (*Yamada et al., 2013a; Yamada et al., 2013b*). The majority of p28 binding sites are within the non-mutated L_1 loop (aa 112-124) (*Friedler et al., 2002; Inga and Resnick, 2001; Zupnick and Prives, 2006*) and a mutable region e.g. (Y220C, P223L) within the $S_{7\text{-}8}$ loops (aa 214-236) of the DBD (*Yamada et al., 2013a*). In the last few years, it has been shown that missense or deletion mutations within the p53 DBD that do not prevent contact with DNA or completely unfold the molecule do not inhibit a p28 induced post-translational increase in wild type (p53wt) or mutated (p53mut) p53 and accompanying decrease in the downstream cell cycle inhibitor p21 (*Yamada et al., 2009; Yamada et al., 2013a; Yamada et al., 2013b*) in a wide variety of cancer cells, nor elicit a deleterious gain-of-function via either p63 or p73 (*Coppari et al., 2014*). Finally, molecular dynamics

simulations, computational docking and cluster analyses have predicted that hydrophobicity as well as secondary structure may play a significant role in the binding of p28 to the L_1 and S_{7-8} loops of the p53 DBD (*Santini et al., 2011; Yamada et al., 2013b*).

In connection with this, a multidisciplinary approach has been used in order to investigate if mutation induced structural changes in the p53 DBD that potentially reduce the hydrophobicity of the p28 binding site(s) could lead to an alteration of DBD conformation and p28 binding. Atomic Force Spectroscopy (AFS) has thus been used to study, at the single molecule level, the interaction of p28 with both non-physiological and physiological p53 DBD mutants. In the first case, single point mutants have been used in which the hydrophobicity of p28 binding sites has been modified by substituting hydrophobic amino acids residues located in the DBD L_1 loop (L114D, A119D, C124D) or in the S_{7-8} loop (C229D) with aspartate. On the other hand the physiological mutants K164E, R173H and double mutant P223L,V274F have been considered to complete the picture of the influence of mutations on the DBD conformational changes and p28 binding. AFS binding data have been then integrated with molecular dynamic simulation studies, and Raman Spectroscopy results, these last allowing to determine how mutations alter the overall conformation and secondary structure motifs (α-helix, β-sheet and random coil) of the DBD.

Overall, it emerged that mutation induced reductions in the β-sheet content of specific motifs within the p53 DBD are associated with a loss of secondary structure and conformation essential to the integrity of p28 binding to the p53 DBD.

Materials and Methods

Sample Selection and Purification. The wild type-DBD fragment, a.a. 81-300 of p53 ~25 kDa, (*Yamada et al., 2013a; Yamada et al., 2013b)* and four site-directed mutants (Leu114Asp, Ala119Asp, Cys124Asp and Cys229Asp) were constructed and purified as described (*Yamada et al., 2009).* p28 (Leu^{50}–Asp^{77} LSTAADMQGVVTDGMASGLDK-DYLKPDD, 2,914 Da) was synthesized by C S Bio, Inc., (Menlo Park, CA, USA) at >95% purity and mass balance.

AFS tip functionalization and substrates preparation. p28 was bound to the silicon nitride AFM tips (Veeco Instruments, Plainview, NY, USA) through a cysteine residue conjugated to its NH_2-terminus to create p29 (Cys-p28, 3.0 kDa) as described in *Bizzarri et al., 2011*. The

tips were cleaned in acetone for 10 minutes, dried with a stream of nitrogen, and ultraviolet (UV) irradiated for 30 minutes to expose hydroxyl groups. Later, they were immersed in a solution of 2% (v/v) 3-aminopropyl-triethoxysilane (APTES) (Acros Organics, Geel, Belgium) in chloroform in order to functionalize the tip surface with amino groups, incubated for 2 hours at room temperature, washed with chloroform and then dried with nitrogen. Silanized tips were immersed in 1 mM N-hydroxysuccinimide-polyethylene glycolmaleimide (NHS-PEG-MAL, molecular weight), 1395 Da, 9.5 nm in length from Thermo Scientific Inc, Waltham, MA) and dissolved in dimethylsulfoxide (DMSO) for 3 hours at room temperature. The NHS-ester group at one end of the PEG reacts with amino-silane molecule to form an amide bond while the -MAL group at the other hand reacts with the -SH group of the cysteine residue conjugated to the NH_2-terminal of p28. After washing with DMSO and Milli-Q® (Millipore, Billerica, MA, USA) water, the tips were incubated with 10 µL of a 10 µM solution of p29 in 50 mM phosphate buffered saline (PBS), pH 7.5, overnight at 4°C. The tips were then gently rinsed and stored in buffer at 4°C.

Distinct glass slides were prepared to separately immobilize wild type and mutants p53 DBD by following the procedure reported in *Bizzarri et al., 2011*. Briefly, the substrates were cleaned in acetone for 5 minutes, dried under a stream of nitrogen, and then UV-irradiated for 30 minutes. After immersion in 0.3 M APTES in chloroform and incubation for 3 minutes at room temperature, they were rinsed in three changes of chloroform and dried with nitrogen. Glass slides were subsequently incubated with a solution of 1% glutaraldehyde (Sigma-Aldrich, St Louis, MO, USA) in Milli-Q water for 4 minutes at room temperature, rinsed with Milli-Q water, and dried with nitrogen. Fifty µL of a 10 µM solution of DBD wild type and mutants in 50 mM PBS pH 7.5 were poured onto this amine-reactive surface, incubated overnight at 4°C, gently washed with PBS, and stored in buffer at 4°C.

Force Spectroscopy measurements. Force measurements were carried out in PBS buffer (50 mM K3PO4, 150 mM NaCl, pH 7.5) using force calibration mode atomic force microscopy (AFM). The cantilevers had a nominal spring constant, k_{nom}, of 0.02 N/m. The effective spring constant, k_{eff}, was determined by the procedure reported in *Hutter and Bechhoefer, 1993*. A relative trigger of 50 nm was applied to limit the maximum contact force applied by the tip on the protein to 0.5 nN. A ramp size of 150 nm was set, and an encounter time of 100 ms established. Tip was approached to the substrate at a constant velocity of 50 nm/s, while

the retraction velocity was varied from 50 to 4.200 nm/s, according to the selected nominal loading rates, defined as the product of the nominal cantilever spring constant (k_{nom}) by the tip pulling velocity (v), and set in the nominal range of 1–84 nN/s. The effective loading rate was determined by replacing the nominal cantilever constant with the effective one, k_{syst}, to take into account that molecules (e.g proteins and/or linkers) tied to an AFM tip make the cantilever spring constant change. The k_{syst} values were obtained, at various loading rates, from the slope of the retraction curve immediately prior to the unbinding event as reported in *Friedsam et al., 2003*. For each force experiment, thousands force curves for each loading rates (five to six loading rates were selected) were recorded to perform a statistical analysis and obtain a reliable quantitative information from the experiments. Moreover, to check the specificity of the interactions, control experiments were performed by adding a 30 μM solution of free p28 on the DBD functionalized substrates.

Molecular Dynamics and docking studies. Computer simulations were performed essentially as described (*Bizzarri et al., 2009; De Grandis et al., 2007*). Configurations for azurin and the DNA-binding domain (DBD) of p53 were taken from PDB files 1E5Z (chain B) and 1UTP (chain A) at 2.0 Å and 2.2 Å resolution, respectively. The 28 aa sequence of p28 was cut from the overall crystallographic structure for azurin and used to generate the configuration file subsequently applied to MD simulations at 300 K and P = 1 bar. The Nose–Hoover thermostat method was applied to control the system temperature, with a coupling time constant t = 0.1 ps. Constant pressure was imposed using the Parrinello–Rahman extended-ensemble (P = 1.0 ps). p28 was minimized with steepest descent and gradually heated from 50 to 300 K at increments of 50 K. The system was then equilibrated by a 600 ps MD simulation under position restraints, prior to an unrestrained MD run for 3 ns. The resulting structure file for p28 was used for further analysis. Amino acid substitutions and internal deletions of p53DBD present in solid tumor cell lines were modeled using the Schrödinger molecular modeling package (*Yamada et al., 2013b*). ClusPro (*Kozakov et al., 2010*) was used to conduct automated docking as a six-dimensional search within the rotational space between the two molecules. The docking algorithms of ClusPro evaluate 10^9 putative complexes, retaining a preset number with favorable surface complementarities, after filtering with electrostatic and desolvation free energies for further clustering. The desolvation free energy used the atomic contact potential (*Zhang et al., 1997*), a statistical

measure of the desolvation free energy, with the electrostatic free energy calculated using a Coulombic model with a distance-dependent dielectric of 4*r (Camacho et al., 2000).* The top 2000 energetically favorable structures were clustered on the basis of a pairwise binding site root mean squared deviation criterion. Clusters were formed by selecting the ligand that had the most neighbors below a previously selected clustering radius. Each member within the cluster was eliminated from the matrix to avoid overlaps between clusters that were repeated until at least 30 clusters formed, and the cluster model with the best score was selected to further compare the protein–protein interface using the ProtorP: Protein–Protein Interface Analysis Server (*Reynolds et al., 2009*). Complexes calculated by ClusPro were visualized with Visual Molecular Dynamics ver.1.8 (VMD) software (University of Illinois Urbana—Champaign, IL). Molecular surfaces and electrostatic potentials of wild type and mutated p53 were calculated by DeepView (GlaxoSmithKline).

Raman Spectroscopy. A Jobin-Yvon Super Labram confocal system equipped with a liquid nitrogen-cooled CCD (EEV CCD10-11 back illuminated; pixel format: 1024x128 detector and a spectrograph with a 1800 g/mm grating allowing a resolution of 5 cm^{-1}) was used to acquire Raman spectra. A filter to reject the elastic contribution and back-scattering geometry for spectra collection was applied. The source was a diode-pumped solid state laser emitting in the green region of the spectrum at 532 nm with a power of 10 mW (4.4 mW on the sample). Measurements were collected using a 50x objective with a numerical aperture NA=0.6 (laser spot diameter reaching the sample was about 1μm). A confocal diaphragm of 400 μm and a slit of 200 μm were chosen as optimal acquisition parameters. The typical acquisition time was 3 minutes. Specimen drops were deposited on optical glass for the acquisition. Band fitting of the Raman Amide I mode (1545-1725 cm^{-1}) was performed essentially as described (*Maiti et al., 2004*). The spectral region between 1620-1725 cm^{-1} was fitted with three curves associated with helical conformations, 1655 cm^{-1}, β-sheet structures (1667 cm^{-1}) and random coiled regions at 1680-1685 cm^{-1}. An additional curve was fit at 1645 cm^{-1}, due to a disordered/vibronic coupling band, as described (*Reinemer et al., 1991*). Spectral peaks at 1550, 1580, 1604, 1615 cm^{-1} were included to account for Trp55, Phe45, Tyr and Tyr35 residues, respectively, since they were not baseline separated from Amide I features. Spectra were normalized with the baseline from 1525 to 1720 cm^{-1} assumed to be linear. Curve-fitting was performed using the Levenberg-Marquardt minimization algorithm

(LMA) and a mixture of Lorentzian/Gaussian pseudo-Voigt functions as peak profiles were employed. Goodness of fit was assessed with a reduced chi-square statistic.

Results

Molecular Dynamic Analysis of protein structure

It was first investigated whether the binding and subsequent post-translation stabilization of $p53^{mut}$ by p28 is dependent on the type of *e.g.* missense and location of the mutation within the p53 DBD. Docking analyses suggests that ~54% of $p53^{wt}$ residues predicted to bind p28 are located within the L_1 and S_7−S_8 loops of p53. Fig. 3.1A illustrates the identity and location of the predicted binding sites for p28 within the DBD of $p53^{wt}$ and the position of the amino acids selected for computational and site directed mutation. Non-polar, hydrophobic amino acids within and outside the non-mutable L_1 loop as well as within the S_7−S_8 loops were uniformly replaced with one with a strong anionic side chain (pKa ~3.7), the hydrophilic aspartate (D), to determine whether alterations in hydrophobicity might alter the predicted interaction between the p53 DBD and p28. In addition, similar types of hydrophobic amino acids predicted to bind p28 located within F113, G117, and outside P128, P142, the non-mutable L_1 loop were computationally altered to aspartate for additional contrast. Negative controls for prediction included hydrophilic to hydrophobic and hydrophilic to hydrophilic alterations at K120 within the L_1 loop (Fig. 3.1B) that is not predicted to bind p28 and does not contact DNA (*Lukman et al., 2013*). Computationally generated predictions of p28 binding suggest that ~90% p53 mutations that significantly alter the hydrophobicity within the L_1 and S_7-S_8 loops of the DBD of p53 or completely unfold the molecule, *e.g.* by introducing a large hydrophobic side chain (S241F) (*Yamada et al., 2013b*), consistently alter the predicted binding of p28 for p53. In particular, it appears that p28 continues to bind, but to another, essentially the same, site on the DBD. The A119D transition, and negative controls did not, suggesting A119 is not a critical aa for the interaction. Fig. 3.2A presents a ribbon diagram illustrating the location of actual and site directed mutations as a function of secondary structure within the DBD of p53. Fig. 3.2 B-J illustrate the contrast in surface hydrobophicity from wild type (Fig. 3.2 B,G) generated by hydrophobic to hydrophilic substitutions within predicted binding sites for p28 (Fig. 3.2 C-F) using the DeepView software package. Additional mutations within the DBD of solid tumor cells (Fig. 3.2 H-J), previously modeled to assess potential binding (*Yamada et al., 2013b*),

are also reanalyzed here with the DeepView software. Substitution of non-polar hydrophobic amino acids with the anionic (electrophilic) aspartic acid at positions 114 and 119 altered the surface charge from essentially neutral to anionic, while substitution of the special case (polar, hydrophobic) amino acid cysteine at positions 124 and 229 to aspartic acid slightly reduced the cationic (Fig. 3.2 E) and increased the anionic surface charge (Fig. 3.2F) of the p53 DBD, respectively.

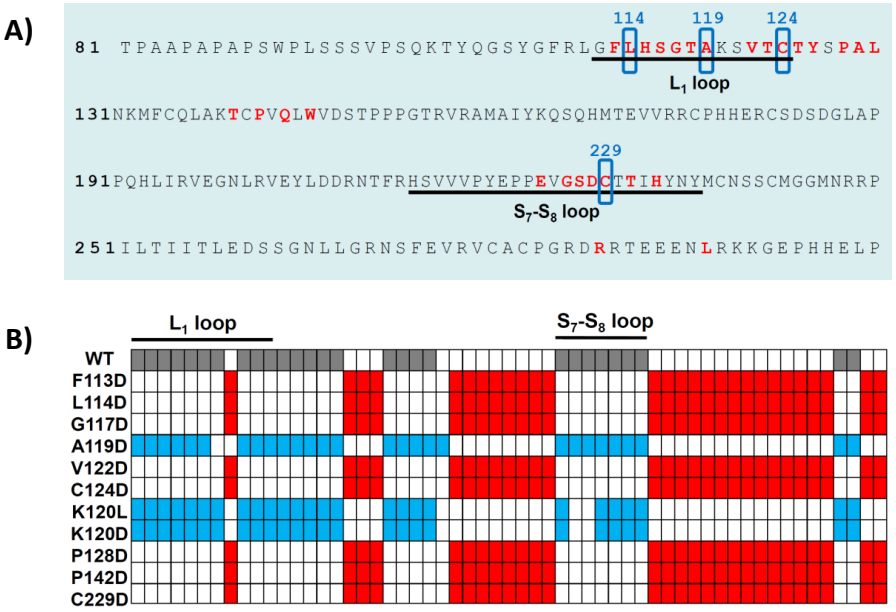

Figure 3.1. A. Predicted p28 binding sites within the p53 DNA-binding domain. The L_1 loop (aa 112-124) and S_7-S_8 loop (aa 214-236) are underlined. Predicted p28-binding residues including parts of L_1 and S_7-S_8 loops and R282 and L289 indicated (red) within p53DBD (aa 81-300 of human p53). Site-directed mutation sites are indicated (blue box). **B**. Hydrophobic Interaction between p53DBD and p28. Amino acid substitutions of p53 (left) were modeled using the Schrödinger software package. Docking analyses of potential alterations of p28 binding to $p53^{mut}$ sites relative to $p53^{wt}$ were carried out using the ClusPro 2.0 server. Residues on $p53^{wt}$ binding p28 are gray. Residues on $p53^{mut}$ with >95% identity to $p53^{wt}$ are in blue. p28 binding sites are predicted to be significantly altered when hydrophobic aa of p53 was mutated to hydrophilic aa (red).

The naturally occurring mutations at positions 164, (positive to negative, hydrophilic, Fig. 3.2H) altered the surrounding surface charge to anionic, while minimal changes to

hydrophobicity, at 223 and 274, (Fig. 3.2 I) did not alter surface charge. A slight reduction in positive charge and hydrophilicity in the naturally occurring mutation R273H (Fig. 3.2 J) produced the expected slight reduction in surface charge. It was previously demonstrated that contact mutations that prevent p53 binding to DNA (R273H) (Fig. 3.2 J) may, but do not necessarily, alter the binding motif for p28 on p53 (*Yamada et al., 2013a*). This also appears true for either non-frameshift, internal deletions (Δ178−183) (*Yamada et al., 2013a*) or multiple missense mutations (P223L, V274F) (Fig. 3.2, I) that essentially lie outside the L_1 and S_7−S_8 loops, the major p53 DBD binding motifs for p28.

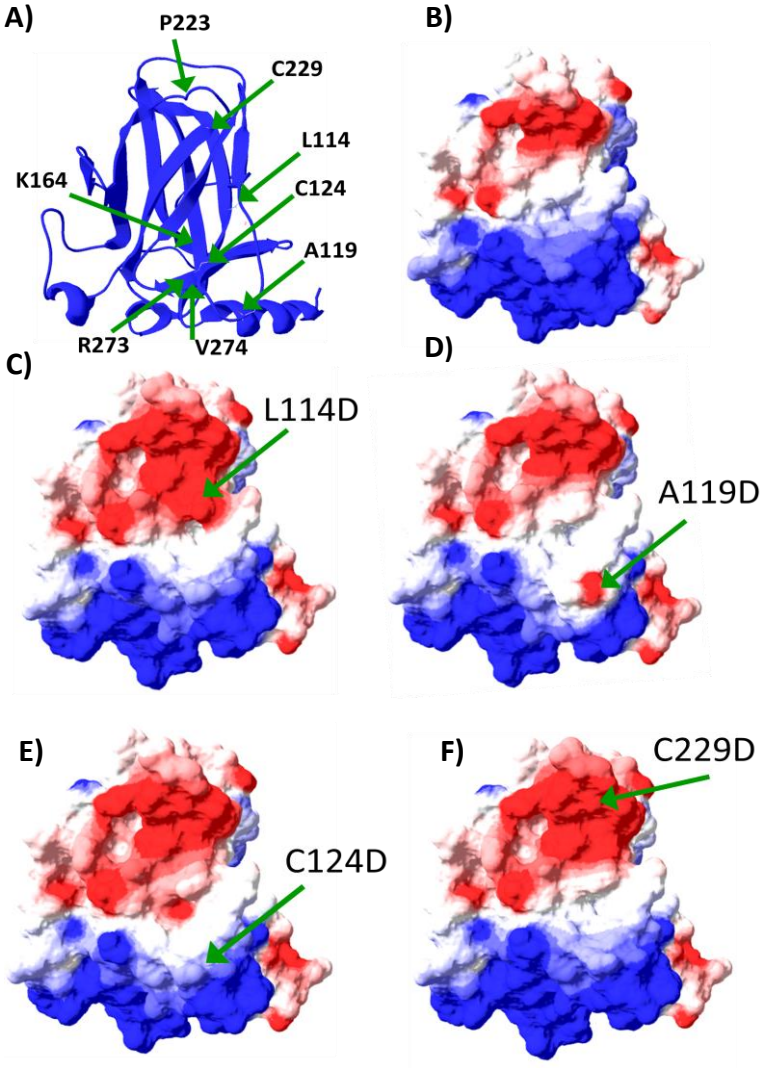

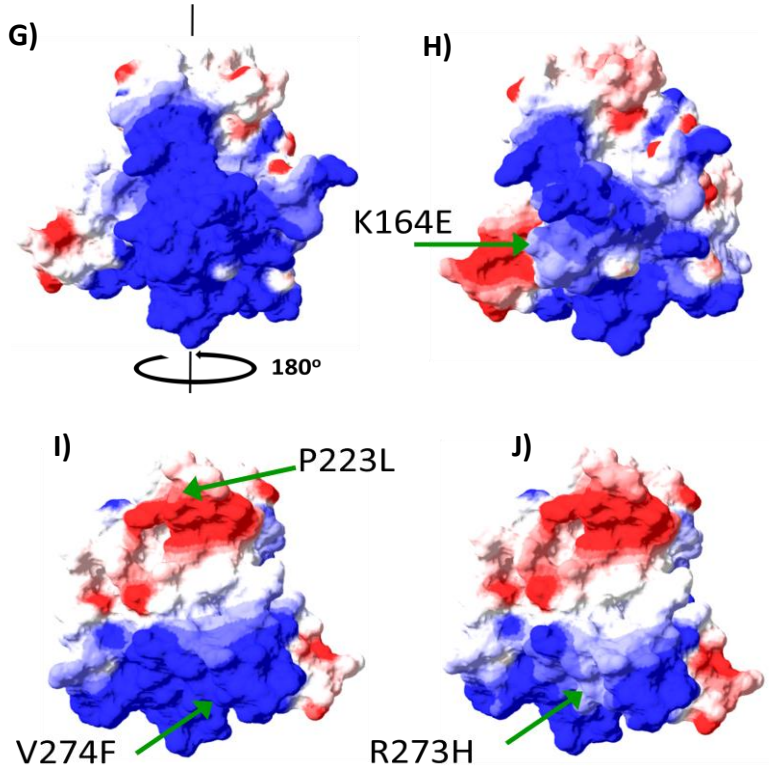

Figure 3.2. A) Ribbon-diagram of the wt p53DBD. Arrows indicate the amino acid positions where mutations were introduced (L114, A119, C124 and C229) as well the position of naturally occurring mutations analyzed (K164E, R273H, P223L/V274F) . The β-barrel structure of the p53DBD orientated vertically. Molecular surfaces and electrostatic potentials of wt (**B, G**) and mut (**C-F, H-J**) p53DBD were calculated by DeepView (GlaxoSmithKline). **G,H**:180º rotated vertically. Arg, Lys, Glu and Asp were used as charged amino acids. Cationic and anionic areas are represented in blue and red, respectively.

AFS analyses of p28 binding to the p53 DBD

With the p29-functionalized tip, thousands of force curves were recorded at several distinct points of the DBD functionalized substrates. A scheme of the approach-retraction cycle performed to acquire force–distance curves being shown in Fig. A.3 (*Appendix A).* Details on the AFS experimental procedure followed being reported in *Appendix A*. Briefly, after selecting force curves corresponding to specific unbinding events (e.g. force curves whose

retraction portion, before the jump-off, exhibited a nonlinear trend starting and ending at the zero-deflection line) the unbinding frequency was calculated for each one of the binding interactions. Unbinding forces were extracted at each loading rate from the collection of curves assigned to specific events and plotted as histograms. The most probable unbinding force values were then determined from the maximum of the main peak of each histogram. Once the most probable unbinding force was determined for each loading rate, the kinetic parameters x_β and k_{off}, at zero force conditions, were extracted by applying the Bell–Evans model, which describes the unbinding process in a non-equilibrium condition, under the influence of an external force (*Bell, 1978; Evans and Ritchie, 1997*).

Table I contrasts the binding of p28 (p29) to the DBD of $p53^{wt}$ and site directed mutants L114D, A119D, C124D and C229D. Although DeepView analysis (Fig. 3.2 C,D) suggested that the L114D and A119D substitutions increased the anionic nature of the surface of the p53 DBD, docking analysis predicted that only the A119D substitution would allow binding of p28 to the correct amino acids. Now, it emerges that the L114D mutant bound p28 with similar affinity to $p53^{wt}$ while A119D also bound, albeit with a slightly lower affinity, possibly due to the significantly altered k_{off}. As predicted, neither the C124D or C229D mutants bound p28. Interestingly, missense mutations at either K164 or P223 and V274 bound p28 although the affinity (K_D) of the double mutant for p28 was lower than that of $p53^{wt}$ (Table II). The data directly reflect an earlier report showing the relative activity of p28 to inhibit the proliferation of cancer cell lines bearing these mutations *in vitro (Yamada et al., 2013a*.

Table I. AFS results on the interaction between p29 and both wild type and site-direct mutants p53 DBD.

Complex	k_{off}	k_{on}	K_D
p29/DBD $p53^{wt}$	$1.0 \pm 2.1 \cdot 10^{-5}$ s^{-1}	$1.4 \cdot 10^{4}$ M^{-1} s^{-1}	$0.7 \cdot 10^{-9}$ M
p29/DBDmut L114D	$3.0 \cdot 10^{-6}$ s^{-1}	$4.8 \cdot 10^{3}$ M^{-1} s^{-1}	$0.6 \cdot 10^{-9}$ M
p29/DBDmut A119D	$1.3 \cdot 10^{-3}$ s^{-1}	$1.8 \cdot 10^{4}$ M^{-1} s^{-1}	$0.7 \cdot 10^{-7}$ M
p29/DBDmut C124D	no interaction	-	-
p29/DBDmut C229D	no interaction	-	-

Table II. AFS results on the interaction between p29 and natural occurring p53 DBD mutants.

Complex	k_{off}	k_{on}	K_D
p29/DBDmut K164E	$(5.1 \pm 0.2)\cdot 10^{-6}\ s^{-1}$	$\sim 10^3\ M^{-1}\ s^{-1}$	$\sim 10^{-9}$ M
p29/DBDmut R273H	no interaction	-	-
p29/DBDmut P223L,V274F	$(4.3 \pm 2.2)\ s^{-1}$	$\sim 10^3\ M^{-1}\ s^{-1}$	$\sim 10^{-3}$ M

Raman Analysis of protein secondary structure

Raman spectroscopy has been used to analyze the effect of mutations on the secondary structure of the p53 DBD and possible correlation with p28 binding. Particular attention was paid to the analysis of the Amide I band located within spectral region 1620-1725 cm^{-1}, that is strongly dependent on the secondary structure of each protein (*Maiti et al., 2004*). Such a band was fitted with three curves centered at 1650-1656, 1664-1670 and ~1680 cm^{-1} and representing α-helix, β-sheet and random coil (RC) configurations, respectively (*Eker et al., 2004; Tiffany and Krimm, 1972*). An example of curve fitting of the wt p53 DBD in PBS is shown in Fig. 3.3, in which particular attention is given to the Amide I Raman band analysis.

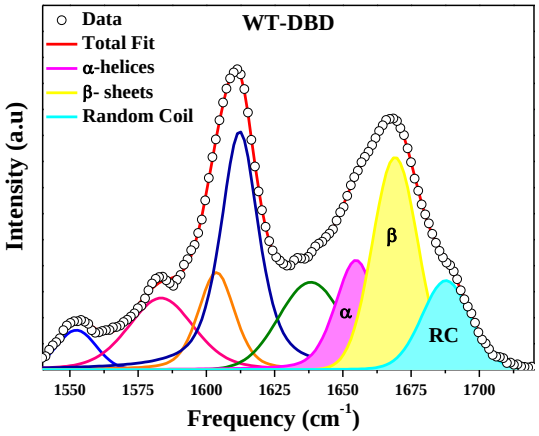

Figure 3.3. Raman spectra (black circles) of DBD wt in PBS fitted through the LMA (red line). Pink, yellow and cyan solid lines are the fitting curves of Amide I band while magenta, yellow and blue regions indicate α-helix, β-sheet and random coil conformations, respectively.

The Amide I Raman band was thus used to unravel the amount of α-helix, β-sheet and random coil present in known structural mutations, K164E, R273H (DNA contact residue), a double mutation at P223L/V274F and single point mutations within the p53 DBD of cancer cells that produce hydrophobic to hydrophilic changes in the normally non-mutable L_1 motif and within the S_{7-8} loop that bind p28, to provide insight as to how mutations might alter secondary structure within the p53 DBD and, consequently, the binding of p28 or similar molecules. The obtained relative contribution (% area) of each secondary structure to the wt and mutants p53 DBD are reported in Table III.

The secondary structure of the wt p53 DBD was comprised of 50% β-sheet, while RC and α helix contribute ~23% and ~27%, respectively, to its conformation. Data reflect the well characterized β-sandwich of the core domain and loop-sheet-helix nature of the DNA binding surface of p53 (*Cho et al., 1994*). These results provided a baseline for analyses of mutational effects on secondary structure of the p53 DBD mutants.

Table III. Secondary structures of wild type and mutated DBD, both physiological and not physiological as resulting from the fitting of the Amine I band of samples.

Sample	**Secondary structure**		
	% α-helix	**% β-sheet**	**% RC**
DBD p53^{wt}	27	50	23
DBDmut L114D	23	44	33
DBDmut A119D	28	43	29
DBDmut C124D	47	18	35
DBDmut C229D	11	24	66
DBDmut K164E	18	59	23
DBDmut R273H	20	43	38
DBDmut P223L/V274F	16	59	25

Concerning the physiological DBD mutants (K164E, R273H , P223L/V274F), the β-sheet structure predominates although the percentage appears to depend on the position of the mutation in the amino acid sequence. The results also suggest that mutations at K164E and P223L/V274F induce an increase in β-sheet content and a decrease in α-helical structure. The relative amount of RC does not significantly change from wt across the K164E and P223L/V274F mutations. In contrast, the DNA-contact mutation (R273H) is associated with a significantly lower β-sheet content and an increase in RC suggesting an unwinding of that portion of the protein. Again, by observing data related to the site-directed, non physiological DBD mutants , the L114D and A119D have a similar α-helix, lower β-sheet and higher RC content to that of the wild-type DBD (Table III) although the L114D mutation has a slight increase in the percentage of RC. Hence, the substitution of the hydrophobic Leu114 and Ala119 with a hydrophilic (acidic) Asp residue within the highly conserved, non-mutable L_1 loop does not appear to significantly alter the secondary structure from wt p53 DBD. On the contrary, the C124D mutant is mainly in an α-helix (47%) and RC (35%) structure while the β-sheet structure represents only 18% of the total, what is in sharp contrast to the wt pattern. Finally the C229D mutation also shows a higher content of an extended RC conformation (66%) relative to wt DBD (23%), with significantly less β-sheet (24%) and α-helix (11%) content.

Conclusions

Azurin derived amphipathic fragment p28 binds with high affinity to the DBD of p53 (*Bizzarri et al., 2011*) without altering its conformation and post-translationally activates p53 (*Yamada et al., 2013a, Yamada et al., 2013b*). Molecular dynamic analyses predicted that the majority of p28 binding sites are within the non-mutated L_1 loop (aa 112-124) (*Zupnick and Prives, 2006*) and a mutable region *e.g.* (Y220C, P223L) within the $S_{7\text{-}8}$ loops (aa 214-236) of the DBD (*Yamada et al., 2013a)* and bind p28 through hydrophobic interaction. We speculated that mutations in the L_1 and S_7-S_8 loops directed at amino acids predicted to bind p28 might compromise local secondary structure sufficiently to alter the affinity for p28 and confirm the predicted regional binding motifs. A multidiscpliplinary approach has thus been used to investigate both the effect in the DBD conformation and p28 binding induced by mutations predicted to change the hydrophobicity of the p28 binding sites, as well the relationship between conformational changes of natural structural mutants, and alterations in

the p28 activity and biological activity also in connection with biochemical data (*Yamada et al., 2013b*).

Molecular dynamic simulations and docking analyses predict that altering the hydrophobicity of selected amino acids within the L_1 and S_7-S_8 loops can potentially alter, and even increase, the number of sites binding p53, while maintaining or reversing the hydrophilicity of the nonbinding K120 does not (Fig. 3.1). However, the L114D mutation in L_1, predicted to alter the binding site of p28, did not significantly alter the affinity (K_D) of the mutant for p28, while the A119D mutation lowered it only slightly (Table 1) in spite of inducing significant local changes in electrostatic potential (Fig. 3.2 C,D). This suggests that the L114D mutation continues to allow p28 to bind to the DBD, at a similar affinity, but at a different site. As Leu is the most hydrophobic residue in the series L114, A119, C124 and C229 (*Kyte and Doolittle, 1982*) a significant reduction in hydrophobicity at position 114 may be critical for p28 binding. This may also be reflected by the increase in random coil content of this mutant relative to the wt DBD. As predicted the A119D mutation continued to bind p28, albeit at a lower affinity (Table I). The relative content of α-helix and β-sheet of these directed L_1 mutations mirrors that of the natural mutations K164E and P223L/V274F (Table III) suggesting missense mutations cause similar types of local disruptions in secondary structure across the DBD, irrespective of whether the mutation produces a change in hydrophobicity.

On the other hand, the significant decrease in β-sheet and increase in random coil associated with the R273H mutation (Table III) is reflected in the absence of predicted (*Yamada et al., 2013a; Yamada et al., 2013b*) and actual (Table II) binding of p28 to p53. Similarly, the significant loss of β-sheet in C124D and C229D mutations and higher content of an extended random coil conformation relative to wt DBD, with significantly less β-sheet (24%) and α-helix (11%) content provides further evidence that local changes in hydrophobicity can significantly alter DBD scaffold organization. Modeling substitution of the special case (polar, hydrophobic) amino acid cysteine (*Cornette et al., 1987*) at positions 124 and 229 to aspartic acid showed a reduced cationic (Fig. 3.2E) and increased anionic surface charge (Fig. 3.2F) of the p53 DBD, respectively. The C124D mutation is at the c-terminus of the L_1 loop at the initiation of a β-sheet (S_2) (Fig. 3.1), while C229D is central within the S_7-S_8 loop. This may provide an explanation of why we observed a significant reduction in β-sheet content relative to wt DBD and L_1 mutations. As the overall NMR structure of p53 core domain is a β-sandwich, composed of two antiparallel β-sheets with a small β-hairpin (124–135) in

contact with the second β-sheet, closing the access to the hydrophobic core (*Canãdillas et al., 2006*) altering hydrophobicity and charge of the c-terminus of the L_1 loop or the β-hairpin would appear to reduce p28 binding (Table I). A similar case could be made for the S_7-S_8 loop.

Overall, the combination of molecular dynamic modeling with docking analysis, atomic force and Raman spectroscopies and a suitable fitting procedure allowed us to conclusively suggest that a mutation induced reduction in β-sheet content of specific motifs within the p53 DBD is associated with a loss of secondary structure and conformation, essential to the integrity of p28 binding to the p53 DBD. p28 is active in initial clinical trials in patients with a variety of advanced, $p53^{wt,mut}$ positive tumors with no significant drug related adverse effects or toxicity (*Lulla et al., 2016; Warso et al., 2013*). Additional efforts to define how p28 and similar proteins stabilize wt and mutated p53 will no doubt improve the performance of these type of agents.

References

Bell GI. 1978. Models for the specific adhesion of cells to cells. *Science*. **200:** 618–627.

Bizzarri AR, Di Agostino S, Andolfi L, Cannistraro S. 2009. A combined atomic force microscopy imaging and docking study to investigate the complex between p53 DNA binding domain and Azurin. *J. Mol. Recognit.* **22**:506-515.

Bizzarri AR, Santini S, Coppari E, Bucciantini M, Di Agostino S, Yamada T, Beattie CW, Cannistraro S. 2011. Interaction of an anticancer peptide fragment of azurin with p53 and its isolated domains studied by atomic force spectroscopy. *Int. J. Nanomedicine* **6**: 3011–3019.

Camacho CJ, Kimura SR, DeLisi C, Vajda S. 2000. Kinetics of desolvation-mediated protein-protein binding. *Biophys. J.* **78**: 1094-1105.

Canãdillas JM, Tidow H, Freund SM, Rutherford TJ, Ang HC, Fersht AR. 2006. Solution structure of p53 core domain: structural basis for its instability. *Proc. Natl. Acad. Sci. U S A*. **103**: 2109-2114.

Cho Y, Gorina S, Jeffrey PD, Pavletich NP. 1994. Crystal structure of a p53 tumor suppressor-DNA complex: understanding tumorigenic mutations. *Science* **265**: 346-355.

Coppari E, Yamada T, Bizzarri AR, Beattie CW, Cannistraro S. 2014. A nanotechnological, molecular-modeling, and immunological approach to study the interaction of the anti-tumorigenic peptide p28 with the p53 family of proteins. *Int. J. Nanomedicine* **9**: 1799-1813.

Cornette JL, Cease KB, Margalit H, Spouge JL, Berzofsky, JA, DeLisi C. 1987. Hydrophobicity scales and computational techniques for detecting amphipathic structures in proteins. *J. Mol. Biol.* **195**: 659-685.

De Grandis V, Bizzarri AR, Cannistraro S. 2007. Docking study and free energy simulation of the complex between p53 DNA-binding domain and azurin. *J. Mol. Recognit.* **20**: 215-226.

Eker F, Griebenow K, Cao X, Nafie L A, Schweitzer-Stenner R. 2004. Preferred peptide backbone conformations in the unfolded state revealed by the structure analysis of alanine-based (AXA) tripeptides in aqueous solution. *Proc. Natl. Acad. Sci. U S A* **101**: 10054-10059.

Evans E, Ritchie K. 1997. Dynamic strength of molecular adhesion bonds. *Biophys. J.* **72**:1541–1555.

Friedler A, Hansson LO, Veprintsev DB, Freund SM, Rippin TM, Nikolova PV, Proctor MR, Rudiger S, Fersht AR. 2002. A peptide that binds and stabilizes p53 core domain: chaperone strategy for rescue of oncogenic mutants. *Proc Natl Acad Sci U S A* **99**: 937-942.

Friedsam C, Wehle AK, Kuhner F, Gaub HE. 2003. Dynamic single molecule force spectroscopy: bond rupture analysis with variable spacer length. *J. Phys. Condens. Matter* **15**: S1709–1723.

Hutter JL, Bechhoefer J. 1993. Calibration of atomic-force microscope tips. *Rev. Sci. Instrum*. **64**:1868–1873.

Inga A, Resnick MA. 2001. Novel human p53 mutations that are toxic to yeast can enhance transactivation of specific promoters and reactivate tumor p53 mutants. *Oncogene* **20**: 3409-3419.

Kyte J, Doolittle RF. 1982. A simple method for displaying the hydropathic character of a protein. *J. Mol. Biol.* **157**: 105-132.

Kozakov D, Hall DR, Beglov D, Brenke R, Comeau SR, Shen Y, Li K, Zheng J, Vakili P, Paschalidis I, Vajda S. 2010. Achieving reliability and high accuracy in automated protein docking: ClusPro, PIPER, SDU, and stability analysis in CAPRI rounds 13-19. *Proteins* **78**: 3124-3130.

Lukman S, Lane DP, Verma CS. 2013. Mapping the structural and dynamical features of multiple p53 DNA binding domains: insights into loop 1 intrinsic dynamics. *PloS one* **8**: e80221.

Lulla RR, Goldman S, Yamada T, Beattie CW, Bressler L, Pacini M, Pollack IF, Fisher PG, Packer RJ, Dunkel IJ, Dhall G, Wu S, Onar A, Boyett JM, Fouladi M. 2016. Phase 1 trial of p28 (NSC745104), a non-HDM2-mediated peptide inhibitor of p53 ubiquitination in pediatric patients with recurrent or progressive central nervous system tumors: A Pediatric Brain Tumor Consortium Study. *Neuro Oncol.*

Maiti NC, Apetri MM, Zagorski MG, Carey PR, Anderson VE. 2004. Raman spectroscopic characterization of secondary structure in natively unfolded proteins: alpha-synuclein. *J. Am. Chem. Soc.* **126**: 2399-2408.

Reinemer P, Dirr HW, Ladenstein R, Schaffer J, Gallay O, Huber R. 1991. The three-dimensional structure of class pi glutathione S-transferase in complex with glutathione sulfonate at 2.3 A resolution. *EMBO J* **10**: 1997-2005.

Reynolds C, Damerell, D, Jones, S. 2009. ProtorP: a protein-protein interaction analysis server. *Bioinformatics* **25**: 413-414.

Santini S, Bizzarri AR, Cannistraro S. 2011. Modelling the interaction between the p53 DNA-binding domain and the p28 peptide fragment of Azurin. *J. Mol. Recognit.* **24**: 1043-1055.

Tiffany ML, Krimm S. 1972. Effect of temperature on the circular dichroism spectra of polypeptides in the extended state. *Biopolymers* **11**: 2309-2316.

Warso MA, Richards JM, Mehta D, Christov K, Schaeffer C, Rae Bressler L, Yamada T, Majumdar D, Kennedy, SA, Beattie CW, Das Gupta TK. 2013. A first-in-class, first-in-human, phase I trial of p28, a non-HDM2-mediated peptide inhibitor of p53 ubiquitination in patients with advanced solid tumours. *Br. J. Cancer* **108**: 1061-1070.

Yamada T, Mehta RR, Lekmine F, Christov K, King ML, Majumdar D, Shilkaitis A, Green A, Bratescu L, Beattie CW, Das Gupta TK. 2009. A peptide fragment of azurin induces a p53 – mediated cell cycle arrest in human breast cancer cells. *Mol. Cancer Ther.* **8:** 2947–2958.

Yamada T, Christov K, Shilkaitis A, Bratescu L, Green A, Santini S, Bizzarri AR, Cannistraro S, Gupta TKD, Beattie CW. 2013a. p28, a first in class peptide inhibitor of COP1 binding to p53. *British J. Cancer* **108**: 2495-2504.

Yamada T, Das Gupta TK., Beattie CW. (2013b). p28, an Anionic Cell-Penetrating Peptide, Increases the Activity of Wild Type and Mutated p53 without Altering Its Conformation. *Mol. Pharm.* **10**: 3375–3383.

Zhang C, Vasmatzis G, Cornette J L, DeLisi C. 1997. Determination of atomic desolvation energies from the structures of crystallized proteins. *J. Mol. Biol*. **267**: 707-726.

Zupnick A, Prives C. 2006. Mutational analysis of the p53 core domain L1 loop. *J. Biol. Chem.* **281**: 20464-20473.

Chapter 4

Interaction of mutant p53 with p73: A Surface Plasmon Resonance and Atomic Force Spectroscopy study

Abstract

Background: TP53 tumor suppressor gene is mutated in more than 50% of human tumors. Mutated p53 proteins could sequestrate and inactivate p73 reducing the apoptotic and anti-proliferative effects of the transcription factor, and yielding cancer cells more aggressive and chemoresistant. The possibility of using drugs to prevent the mutant p53/p73 complex formation preserving the p73 function, calls for a deeper insight into the molecular and biochemical mechanisms of mutant p53/p73 protein interaction.

Methods: The kinetics of the mutant p53R175H/p73 complex was investigated with innovative and complementary techniques, operating in real time, in near physiological conditions and without any labeling. Specifically, Atomic Force Spectroscopy and Surface Plasmon Resonance working at single-molecule level and in bulk condition, respectively, were used.

Results: The two techniques revealed that a stable complex is formed between mutant p53R175H and p73 proteins; the complex being characterized by a high interaction force and a dissociation equilibrium constant in the order of 10^{-7} M, as expected for specific interactions. No binding was instead observed between p73 and wild type p53.

Conclusions: Mutant p53R175H protein, unlike wild type p53, can form a stable complex with p73. The mutant p53R175H/p73 protein complex could be a target for innovative pharmaceutical drugs that, by dissociating it or preventing biomolecule interaction thus preserving the p73 function, could enhance the response of cancerous cells carrying mutant p53R175H protein to common chemotherapeutic agents.

General significance: The kinetic information obtained *in vitro* may help to design specific pharmaceutical drugs directed against cancerous cells carrying mutant p53 proteins.

The results presented in this chapter have been published as:

Santini S, Di Agostino S, Coppari E, Bizzarri AR, Blandino G, Cannistraro S. 2014. *Biochim. Biophys. Acta* **1840**: 1958-1964.

1. Introduction

p53 is a tumor suppressor protein called the "*guardian of the genome*" (*Lane, 1992*) for its crucial role in the cell cycle progression control and coordination of cellular response to a broad range of stress factors ensuring the maintenance of genomic stability and the prevention of cancer development (*Prives and Hall, 1999, Vogelstein et al., 2000; Levine, 1997*). Tumors expressing a mutant p53 protein (mutp53) are characterized by high genomic instability, resistance to chemotherapy and invasiveness. These new characteristics constitute the main features cancer cells acquire when the tumor suppressor p53 gene undergoes gain-of-function (GOF) mutations (*Levine, 1997*). More than 50% of human cancers carry TP53mutations that abrogate its wild type function (*Vogelstein et al., 2000; Greenblatt et al., 1994*). Although two thirds of mutations in the DNA-binding domain of p53 abolish the p53 ability to transactivate its target genes through the p53 consensus sequences onto the promoters, the modulation of gene transcription by mutp53 is well documented as an important GOF mechanism. Probably mutp53 acts as an adaptor or mediator that links specific transcription factors to the general transcription apparatus. It has been shown how mutp53 reaches target gene promoters through the interaction with sequence-specific transcription factors, such as NF-Y, E2F1, NF-kB and the Vitamin D receptor (*Di Agostino et al., 2006; Weisz et al., 2007; Fontemaggi et al., 2009; Stambolsky et al., 2010*). In such aberrant cells, the p53 activity could be, at least in part, vicariated by two members of its family, p63 and p73, that share high structural and functional homology with p53 (*Kaghad et al., 1997; Schmale and Bamberger, 1997; Jost et al., 1997; Kaelin Jr, 1999*). In fact, both p63 and p73 are activated by the same signaling pathways that lead to the p53 activation and stimulate the transcription of p53 responsive genes controlling cell proliferation, differentiation and death (*Collavin et al., 2010*). Furthermore mutp53, unlike the wild type p53 (wtp53), can interact and sequester both p73 and p63 family members, abrogating their antitumoral function (*Di Como et al., 1999; Strano et al., 2000; Strano et al., 2002*). In particular, many evidences indicate that p73 loss of function in p53 defective cells not only contributes to the insurgence, maintenance and spreading of human cancers (*Flores et al., 2005; Sigal et al., 2000; Strano et al., 2007*), but it

is also a major determinant of human tumor chemoresistance (*Irwin et al., 2003; Bergamaschi et al., 2003; Lunghi et al., 2009*). In this context, the efforts to search innovative pharmaceutical drugs and molecules able to dissociate the aberrant mutp53/p73 protein complex (*Di Agostino et al., 2008*) safeguarding the p73 activity are arousing greater interest. Of course, a deeper knowledge of the molecular and biochemical interaction mechanisms underlying the formation of the mutp53/p73 complex, could help to design more specific drugs. In particular, the present work is aimed at shedding light on the kinetics of the interaction between full length p73 and the conformational mutant p53R175H (mutp53R175H) proteins, the latter having a point mutation of codon 175 of the TP53 gene. Such an interaction has been already detected both *in vitro* and *in vivo* (*Di Como et al., 1999; Strano et al., 2000; Di Agostino et al., 2008*). Indeed, it is believed that this interaction severely impairs the p73-mediated transcriptional activity and apoptosis in response to anticancer drugs by sequestering p73 away from its target gene promoters (*Strano et al., 2000; Di Agostino et al., 2008*). These evidences emerge in human large lung carcinoma and breast cancer cells where p53 is mutated (*Strano et al., 2000; Di Agostino et al., 2008*). The mutp53R175H/ p73 protein interaction has been studied here using two innovative and complementary techniques, Atomic Force Spectroscopy (AFS) and Surface Plasmon Resonance (SPR). AFS is a nanotechnological-based approach able to detect piconewton interaction forces between a tip anchored molecule and its substrate-immobilized partner, even at single molecule level, in near native conditions and without any label or sample preparation (*Bizzarri and Cannistraro, 2009; Bizzarri and Cannistraro, 2010*). On the other hand, SPR is a flexible and powerful approach providing the kinetic and equilibrium characterization of binding processes occurring between a sensor chip immobilized ligand and its partner free in solution (*Homola et al., 1999; Cooper, 2003*). Taken together, the AFS and SPR results demonstrate that mutp53R175H protein forms a high affinity complex with p73. At single molecule level, such a complex is characterized by a dissociation rate constant typical of specific complexes, as well by a high interaction force and a single barrier in the energy landscape. No interaction has been instead monitored between p73 and wild type p53.

2. Material and Methods

2.1. GST-protein expression and purification

Escherichia coli cells (BL21DE3) transformed with pGEX-4X-mutp53R175H, pGEX-4X-

wtp53 and pGEX-4X-p73 vectors were grown at 37°C in LB medium containing 100µg/ml ampicillin to an optical density at 600 nm of 0.4. Expression of recombinant proteins was induced by the addition of 0.5 mM isopropyl-1-thio-β-galactopyranoside (IPTG) for 3 hours at the same temperature under vigorous shaking. Bacteria were pelleted and lysed in phosphate-buffered saline (PBS 1X) containing 0.1% Triton X-100, 1mM DTT, protease inhibitors, by probe sonication (three cycles of 1 minute each). The sonicate was clarified by centrifugation at 13000 rpm and supernatant fractions were incubated with glutathione-Sepharose beads (Sigma, G 4510) for 1 hour at 4°C with constant shaking. After several washes in PBS, the GST-proteins beads were re-suspended in 1X PBS containing 300 mM $CaCl_2$ and 10 units of thrombin protease (Amersham Biosciences). After incubation at room temperature (RT) for 16 h, the GST-free supernatant fractions containing wtp53, mutp53R175H and p73 purified proteins were passed three times through a column containing 1 ml of *p*-aminobenzamidine-agarose beads (Sigma, A-7155). The eluates containing the purified proteins were dialyzed against storage buffer (50mM Tris-HCl pH 7.5, 1 mM $MgCl_2$, 0.5 mM DTT). Levels of expressed proteins were checked by SDS-PAGE and Coomassie Brilliant Blue R-250 staining, while known amounts of bovine serum albumin were used as standard. Additional protein concentrations were determined by colorimetric assay (Bio-Rad, Hercules, CA, USA).

2.2. Functionalization of AFS substrate and tips

Silicon nitride Atomic Force Microscopy (AFM) tips (Veeco Instruments, Santa Barbara, CA) and glass substrates were amino-functionalized using a gas-phase method with (3-aminopropyl)triethoxysilane (APTES, Sigma) (*Ebner et al., 2007*).

Full length p73 tumour suppressor proteins were immobilized on cover glass (Ø 12 mm). The glass was cleaned for 5 minutes in acetone and then irradiated by an UV lamp for 30 minutes to expose hydroxyl groups. The clean glass substrate was then placed at RT inside a dessiccator together with the lids of two eppendorf vials in which 30 µl of APTES and 10 µl of triethylamine where separately added. The dessiccator was flooded with N_2 to remove air and moisture. After 2 h incubation time lids were removed, the dessiccator was re-flooded with N_2 and the substrate was here left for 2 days to cure APTES layer. Then, the glass was incubated with a solution of 1% glutaraldehyde in Milli-Q water for 3 minutes at RT, successively rinsed carefully with Milli-Q water and dried with nitrogen. Finally it was

incubated overnight at 4 °C with a 4 μM full length p73 protein solution in Tris HCl pH 7.4, 4% glycerol. Afterwards the substrate was gently washed with buffer to remove the unbound proteins and unreacted aldehyde groups were capped with 10 M ethanolamine-HCl 20 min incubation. Substrate was then washed again and stored at 4 °C. A scheme of the substrate preparation procedure is shown in Fig. 4.1A.

A very similar procedure was used to anchor full length mutp53R175H (or wtp53) protein to the AFS tip cantilever. Once the APTES layer was obtained with the gas-phase method, tips were incubated in 1% glutaraldehyde in Milli-Q water for 4 minutes, rinsed with Milli-Q water, dried with nitrogen and then incubated overnight at 4 °C with 4 μM mutp53R175H (or wtp53) protein. Once the tips were washed and reactive aldehyde groups quenched with ethanolamine, they were stored at 4 °C. A schematic representation of tips functionalization is shown in Fig. 4.1B.

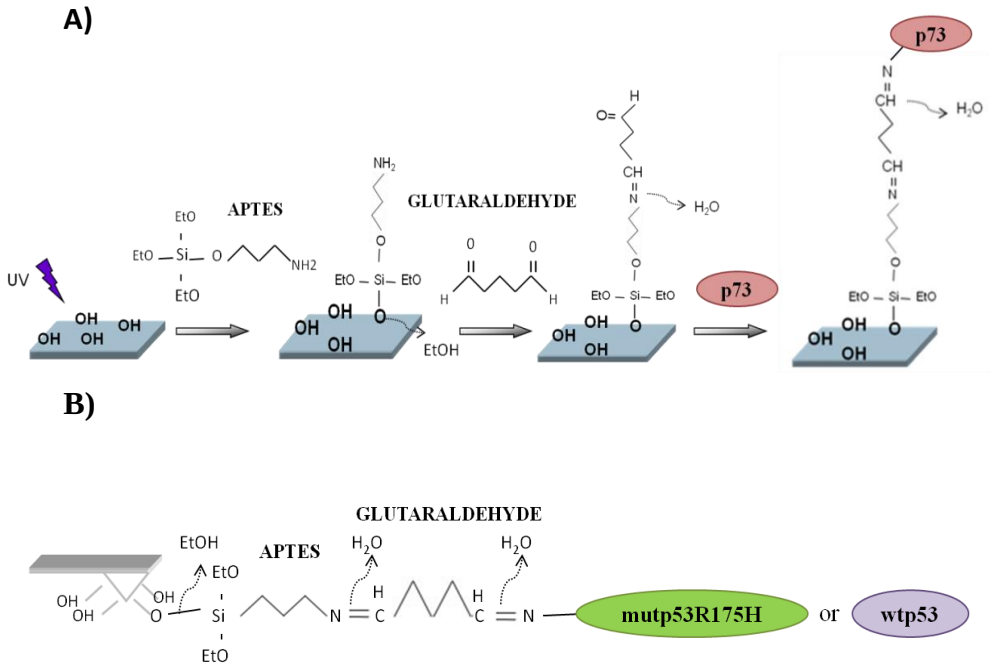

Figure 4.1. Immobilization strategies of p73 and mutp53R175H (or wtp53) on the glass substrate and the AFM tip, respectively. **(A)** p73 protein is immobilized on glass slides via a chemical platform involving sequentially linked amino-silane and glutaraldehyde. **(B)** mutp53R175H or wtp53 proteins are anchored to the AFS silanized tip through the NH_2 groups of lysine residues exposed on the protein surface after tip incubation with glutaraldehyde.

2.3. Force spectroscopy measurements and unbinding detection

Force-distance curves were acquired at RT using a commercial AFM (Nanoscope IIIa/Multimode AFM Digital Instruments, Santa Barbara, CA). AFS measurements were carried out in PBS buffer (50 mM K_3PO_4, 150 mM NaCl, pH 7.5) using force calibration mode AFM. Force plots were acquired using rectangular-shaped Si_3N_4 cantilevers (Veeco probes MSNL-10) with a nominal spring constant, k_{nom}, of 0.02 N/m functionalized as described in section 2.2. The effective spring constant of the functionalized tips, k_{eff}, was determined by following the procedure in ref. (*Hutter and Bechhoefer, 1993*).

A scheme of the approach-retraction (AR) cycle performed to acquire force-distance curves is shown in Fig. 4.2. Starting with the tip away from the substrate and setting a ramp size of 150 nm, mutp53R175H (or wtp53) protein-functionalized tip is approached at a speed, *v*, of 50 nm/s to the p73 protein functionalized surface (point 1 of Fig. 4.2). From the contact point on (point 2), the cantilever begins to deflect as due to the repulsive forces from the overlapping molecular orbitals between the tip and the substrate. The approaching phase (dotted line) keeping on, the cantilever exerts an increasing pushing force on the substrate and its deflection increases while ligand and receptor, brought in close proximity, could interact. When the cantilever exerts a force of 0.5 nN on the substrate, the approach phase is stopped to limit the maximum contact force (point 3). After 100 ms encounter time, the tip is retracted from the substrate (continuous line) at a speed ranging from 50-4200 nm/s, and attractive, adhesion or interaction forces formed during the contact phase, cause a downward curvature of the tip at the contact point (point 4). As far as the retraction phase continues, when the retraction force overcomes the strength of interaction between the partners, the cantilever jumps off returning to the baseline after complex dissociation (point 5). The complex unbinding force can be now determined from the product of the cantilever deflection, d, at the jump-off, by the cantilever effective spring constant, k_{eff} ($F = k_{eff} \cdot d$); the calculated unbinding force depending on the rate at which the force is applied ($r = dF/dt$), denoted loading rate, and it is given by the relationship $r = k \cdot v$, in which *v* is the retraction speed of the cantilever from the substrate (*Bell, 1978*).

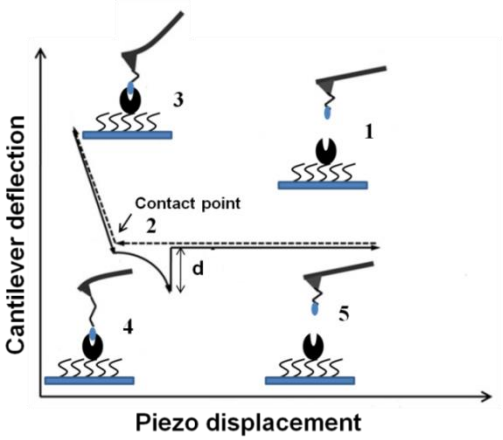

Figure 4.2. Sketch of AFS experiments. See the text for a detailed description.

The AFS experiments were thus performed at five different loading rates in the range 1-84 nN/s. Thousands of force curves were acquired at each loading rate, required to perform a statistical analysis and to obtain a reliable quantitative information from the experiments. To this aim, force curves corresponding to specific unbinding events were selected. Specifically, force curves whose retraction portion before the jump-off exhibited a non-linear trend starting and ending at the zero-deflection line, and curves presenting multiple jumps -due to subsequent rupture of the complex bonds- showing a last jump starting and ending at zero deflection, were used for the successive statistical analysis (*Bizzarri and Cannistraro, 2010*). At each loading rate, the unbinding force histogram was extracted and the most probable unbinding force *(F*)* was taken from the maximum of the main peak of the corresponding histogram. Thereby, the kinetic and thermodynamic parameters at the equilibrium were obtained from these non-equilibrium measurements (*Merkel et al., 1999*), in the framework of the Bell-Evans model (*Bell, 1978; Evans and Ritchie, 1997*) which assumes a linear relationship between the most probable unbinding force, *F**, and the natural logarithm of the loading rate, r, by Eq. (1):

$$F^* = \frac{k_B T}{x_\beta} \ln\left[\frac{r x_\beta}{(k_d k_B T)}\right] \qquad (1)$$

where k_B is Boltzmann's constant and T the absolute temperature, k_d is the equilibrium dissociation rate constant, and x_β is the width of the energy barrier along the direction of the

applied force. The effective loading rate r was here determined by the product between the retraction velocity and the spring constant of the entire system, k_{syst}, to take into account the contribution from molecules (i.e. proteins and/or linkers) tied to the AFM tip. The k_{syst} was thus evaluated as in Friedsam et al., 2003 (*Friedsam et al., 2003*). Therefore, the kinetic parameters k_d and x_β were obtained from the slope and intercept of a linear fit by Eq. (1) of the plot of F^* versus ln (r).

2.4. SPR substrate preparation

SPR analysis was performed at 25 °C with a Biacore X100 system (GE Healthcare, Bio-Sciences AB, Sweden). Using a standard amine coupling chemistry (*Johnsson et al., 1991*), p73 protein (ligand) was coupled on a CM5 sensor chip surface (Fig. 4.3). Briefly, the carboximethilated dextran surface of a CM5 sensor chip was first activated by a 7 min injection of a 1:1 mixture of 0.4 M N-ethyl-N-(3-diethylaminopropyl) carbodiimide (EDC) and 0.1 M N-hydroxyl-succinimide (NHS) at 10 μl/min to give reactive succinimide esters. Then a 0.02 μg/μl ligand solution in 10 mM acetate buffer pH 4.5 was fluxed on a single flow cell of the reactive matrix. In such a way, the NHS esters reacted spontaneously with the ligand amines to form covalent links. The injection of the ligand solution stopped when 110 resonance units (RU) of bound ligand were reached. Once the immobilization procedure was completed, non-specifically bound ligands were removed by washing with running buffer (50 mM PBS buffer pH 7.5 filtered with a 0.22 μM membrane filter, to which surfactant P20 0.005% from GE Healthcare was added) until the RU value became nearly constant. Reactive sites remaining on the surface were blocked by reaction with 1 M ethanolamine-HCl pH 8.5, fluxed over the two flow cells of the micro fluidic system with a flow rate of 10 μl/min for 7 minutes. Running buffer was again fluxed over the surface to stabilize the baseline. The reference flow cell was activated and deactivated without intermediate ligand immobilization in order to be used as a control surface for refractive index change and no specific binding during the kinetic analysis.

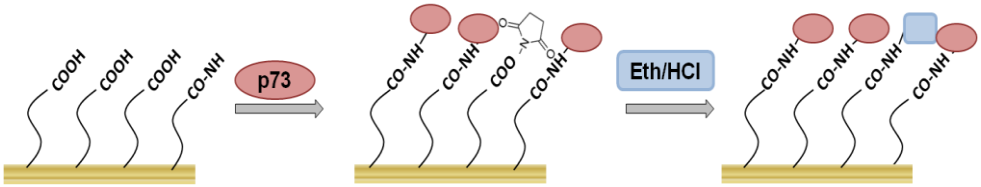

Figure 4.3. Schematic representation of the covalent binding of the p73 protein on the SPR CM5 sensor chip. First, a mixture of EDC/NHS is injected over the chip to activate the surface, then p73 (pink ovals) is fluxed over the surface and the N-hydroxysuccinimide esters react spontaneously with its amino groups to form covalent links. Eventually, reactive sites remaining on the surface are blocked by reaction with 1 M ethanolamine-HCl (Eth/HCl) pH 8.5 (blue rectangles).

2.5. SPR binding experiment

Binding experiments were conducted by a kinetic titration method known as single-cycle kinetics (SCK) which consists in sequentially injecting increasing concentrations of the analyte over the functionalized sensor chip surface, without regeneration steps between each sample injection. It follows that the SCK method is faster than the classical one and that the ligand activity is fully preserved during the experiment, resulting in an increased efficiency and a reduction of costs.

To avoid excessive bulk effects, sensor chip surface was equilibrated with mutp53R175H protein buffer (Tris 100 mM, NaCl 300 mM DTT 1 mM buffer, pH 8) until the baseline was stable and then four increasing concentrations of mutp53R175H protein (analyte) in the range of 0.1 - 1.6. μM, serially diluted, were injected sequentially over both the ligand and the reference surfaces at a flow rate of 30 μl/min for 160 s. Also prior to the analyte binding cycle, buffer was injected for four binding cycles to have a blank response to be used for double reference (see Section 3.2). Analyte injections were followed by a 400 s dissociation step performed with a 30 μl/min flux of running buffer. Analytical cycles were programmed by means of a wizard template and the entire analysis was completely automated. To extract kinetic parameters from SPR data, systematic artifacts were removed using a two steps data correction technique (*Myszka, 1999; Rich and Myszka, 2000*). First, the response collected over the functionalized surface was subtracted by the response obtained from the reference one to remove bulk refractive index change, drift during association phase, jumps due to injection needle positioning. Second, the response from running buffer injection was subtracted. Sensorgrams were then globally fitted using BiaEvaluation software 2.1 (GE

Healthcare, BIO-Sciences AB, Sweden) to a 1:1 interaction model (*Morton and Myszka, 1998*) including the correction for mass transfer rate. Goodness of the fit was evaluated based on visual inspection, on the χ^2 value (expected to be lower than 10) and on the residual plots. After substrate regeneration with a pulse of 10 mM NaOH solution, the interaction of p73 protein functionalized substrate with wtp53 protein was performed. The same experimental conditions (experimental method, analyte concentrations, flow rate, interaction and dissociation time) were set for the mutp53R175H/p73 protein interaction study in order to have comparable data.

3. Results and discussion

3.1. AFS unbinding results

The histograms of the unbinding forces recorded at the different loading rates display similar shapes; a representative histogram corresponding to 1 nN s^{-1} loading rate being shown in Fig. 4.4.

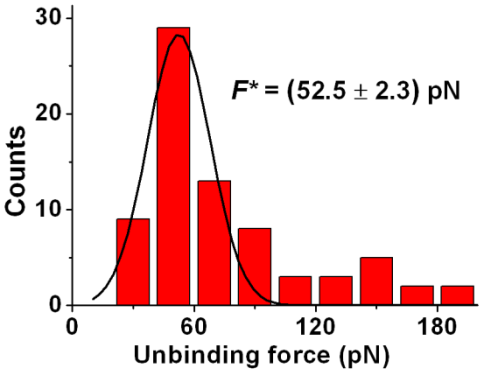

Figure 4.4. Histogram of the unbinding forces for the mutp53R175H/p73 complex from AFS measurements carried out at a loading rate of 1 nN/s. The most probable unbinding force value, *F**, was determined from the maximum of the main peak of the histogram.

However, the most probable unbinding force value (*F**) corresponding to the maximum of the main peak of each histogram, increases with the loading rate and shows values between 50 and 70 pN. These values fall in the range usually recorded for specific biological interactions (*Morfill et al., 2007*). The unbinding frequency, calculated as the ratio between

the number of events corresponding to specific unbinding processes over the total recorded events, is about 11%. Such a value, which is somewhat lower than that expected for ligand-receptor pairs (*Bizzarri and Cannistraro, 2009* and refs. therein), can be explained by considering that p73 is a big protein tightly packed on the glass substrate; this likely resulting into some steric hindrance which may limit the interaction with the partner. Additionally, the randomly bonded p73 protein via its lysine residues, may assume some orientations somewhat unfavorable to the complex formation.

According to the Bell-Evans model, the most probable unbinding force values F^* were plotted as a function of the natural logarithm of the loading rate (Fig. 4.5) in order to extract the kinetic parameters of the interaction. A single linear regime with ascending slope was observed and indicates the overcoming of a single barrier in the energy landscape. By fitting these data with Eq. (1), a width of the energy barrier x_β = (1.32 ± 0.28) nm and a dissociation rate constant, k_d, of (1.18 ± 0.07) · 10^{-5} s^{-1} were found; both these values being typical of specific biological complexes (*Bizzarri and Cannistraro, 2010*).

According to the procedure described in detail elsewhere (*Bizzarri et al., 2011, Taranta et al., 2008*), the complex association rate constant (k_a) was also estimated, by using the expression $k_a = N_A \cdot V_{eff}/t_{0.5}$, where N_A is the Avogadro's number, V_{eff} is the effective volume of a half-sphere with radius r_{eff} around the tip, and $t_{0.5}$ is the time for the half-maximal binding probability given by $t_{0.5} = 2\ r_{eff}/v$, where v is the approach speed of the cantilever. A k_a of about 10^3 M^{-1} s^{-1} was thus found. The corresponding dissociation equilibrium constant ($K_D = k_d/k_a$) of the mutp53R175H/p73 complex was thus in the order of 10^{-8} M; this value positioning the complex in the 'affinity region' typical of antigen-antibody pairs which show a K_D in the range of $10^{-7} – 10^{-11}$ M (*Bizzarri and Cannistraro, 2010*).

On the contrary, the AFS experiment carried out on the interaction between wild type 53 and p73 protein showed only a few number of unbinding specific events together with a negligible unbinding frequency (less than 3 %). This is indicative that no significant interaction between p73 and wtp53 proteins is occurring. Such a result confirms previous data from the literature dealing with immunoprecipitation techniques of whole cellular protein lysates (*Di Como et al., 1999*).

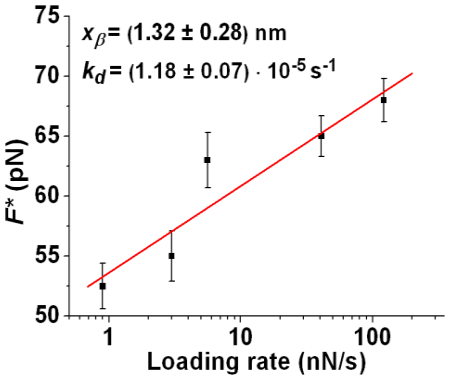

Figure 4.5. The most probable unbinding force, F^*, plotted versus the logarithm of the loading rate r for themutp53R175H/p73 complex, when p73 is immobilized on glass substrate and mutp53R175H is anchored on the AFS tip. The solid line is the bestfit of the experimental data by the Bell–Evans model (Eq. (1)); the extracted parameters k_d and x_β being reported.

3.2. SPR kinetic results

The SCK approach introduced by Karlsson and co workers (*Karlsson et al., 2006*) was used to study the interaction kinetics between mutp53R175H and p73 proteins. Fig. 4.6A (continuous line) shows the SPR signal (RU) as a function of time for successive injections of increasing concentrations of mutp53R175H. After the first injection with a 0.1 μM mutp53R175H solution, the signal increases nonlinearly approaching a plateau. Once the first injection is finished, the buffer is flowed over the ligand and the signal drops down, close to zero. The same trend is observed also for the successive injections of mutp53R175H. As far as higher mutp53R175H concentrations are used, progressively higher RU values are obtained; this being indicative of increasing levels of mutp53R175H (A, analyte) binding with the immobilized p73 (L, ligand). These kinetic data were analyzed in the framework of the Langmuir 1:1 binding model, which assumes a simple reversible bimolecular reaction between the ligand and the analyte (*Björquist and Boström, 1997, O'Shannessy et al., 1993*) as described by the following equation:

$$A_{bulk} \underset{k_t}{\overset{k_t}{\rightleftarrows}} A_{surface} + L \underset{k_d}{\overset{k_a}{\rightleftarrows}} LA \qquad (2)$$

The model was modified to take into account the mass transport effect. In particular, the analyte is transferred from the bulk solution (A_{bulk}) towards the sensor chip surface, and *vice versa*, with a mass transfer coefficient, k_t, which is assumed to be the same in both directions. Then, the analyte that has reached the sensor chip surface ($A_{surface}$), binds to the ligand resulting in the formation of the ligand-analyte complex (LA) characterized by the association, k_a, and dissociation, k_d, rate constants. Accordingly, the variation of $A_{surface}$, L and LA concentrations with time, can be described by the following set of differential equations (*Glaser, 1993*):

$$\frac{d[A_{surface}]}{dt} = k_t\left([A_{bulk}] - [A_{surface}]\right) - \left(k_a[L][A_{surface}] - k_d[LA]\right)$$

$$\frac{d[L]}{dt} = -\left(k_a[L][A_{surface}] - k_d[LA]\right) \qquad (3)$$

$$\frac{d[LA]}{dt} = \left(k_a[L][A_{surface}] - k_d[LA]\right)$$

To extract the kinetic parameters (k_a, k_d and K_D), the sensorgrams were globally fitted by a non linear least square analysis and numerical integration of Eq. (3) (*Morton et al., 1995*), by using the SPR evaluation software package. Such a fit, which is shown as dashed line in Fig. 4.6A, provided a k_a of $(6.4 \pm 0.5) \cdot 10^3$ M^{-1} s^{-1} and a k_d of $(3.1 \pm 1.8) \cdot 10^{-3}$ s^{-1}, with a χ^2 value of 2.24. These values resulted in a $K_D = k_d/k_a$ of $(4.9 \pm 0.6) \cdot 10^{-7}$ M.

The goodness of the 1:1 binding model was checked by generating the adsorption isotherm for the mutp73R175H/p73 system. The RU values reached at the steady state (R_{eq}) for each one of the sample injections shown in Fig. 4.6A were thus plotted versus the corresponding concentrations of the mutp53R175H protein (Fig. 4.6B). Data were fitted (continuous line of Fig. 4.6B) by using the Eq. (4), including a term for the bulk refractive index contribution (RI), which is assumed to be the same for all samples and which is used as the RU-axis offset:

$$R_{eq} = \frac{AR_{max}}{K_D + A} + RI \qquad (4)$$

where R_{max} is the analyte binding capacity of the surface and A is the analyte concentration. A K_D of (8.0 ± 2.2) · 10^{-7} M, with a χ^2 value of 4.86, was obtained confirming the value provided by the global fitting procedures.

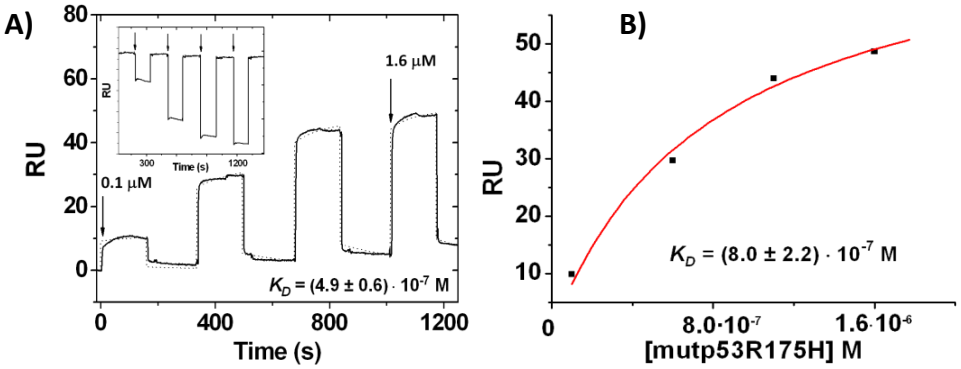

Figure 4.6. SPR kinetic characterization of the interaction ofmutp53R175H and wtp53with p73 **(A).** Sensorgram of response curves (SPR signal in RU) versus time (solid line). Increasing concentrations ofmutp53R175H protein solutions were injected sequentially over the substrate: 0.1mM (1st arrow on the left), 0.6mM (2nd injection), 1.1mM (3rd injection) and 1.6mM (4th injection, indicated with the arrow on the right). By fitting the sensorgram (dotted line) to a 1:1 binding model and taking into account the mass transport limitation, k_a, k_d and K_D values of the interaction are extrapolated. Inset: sensorgram of response curves versus time of increasingly concentrations of wtp53 injected over the p73 functionalized sensor chip surface. Arrows from left to the right indicate the successive injections of increasing concentrations of wtp53 over the substrate. No increase of the baseline signal is observed. **(B)** Binding affinity curve for the interaction ofmutp53R175H protein onto p73 modified CM5 surface after titration with increasing concentrations ofmutp53R175H protein. Equilibrium dissociation constant K_D was calculated by a fit through Eq. (4).

Interestingly, it should be remarked that even if the two experimental approaches, AFS and SPR, operate at different conditions, they strongly support that mutp53R175H and p73 are engaged in the formation of a very specific complex which is characterized by a K_D typical of antigen-antibody pairs, what may be at the basis of the p73 sequestration and inactivation in cancerous cells. The one order of magnitude difference between the K_{Ds} provided by AFS and SPR, which are in the order of 10^{-7} M and 10^{-8} M, respectively, reflects essentially the difference in the dissociation rate constants, k_{ds}, obtained with the two methodologies. Such a

difference should be attributed to the peculiarities of the two experimental techniques in which not only the interaction is monitored at level of single molecule in one case, AFS, and in bulk condition in the other, SPR, but also different substrates and procedures are used to immobilize p73 protein on the substrate, what could lead to slight differences in the results (*Bizzarri and Cannistraro, 2009*).

The same procedure previously described for the SPR investigation of the interaction between mutp53R175H and p73, was used to investigate also the wtp53/p73 binding kinetics. In this case no increase of the SPR signal was observed after the injection of increasing wtp53 concentrations over the p73 functionalized sensor chip surface (see the inset of Fig. 4.6A). This is indicative of the lack of a specific interaction between wtp53 and p73 proteins. Again, both AFS and SPR experiments indicate that no interaction occurs between wtp53 and p73, confirming previous literature data obtained with immunoprecipitation techniques (*Di Como et al., 1999*).

4. Conclusions

AFS and SPR have been used to investigate the interaction between p73 and both wild type p53 and the mutant p53R175H full length proteins in real time, in physiological conditions and without labels or sample manipulation. Both techniques confirm that conformational mutant mutp53R175H can physically interact with p73 resulting in the formation of a high affinity complex characterized by a K_D typical of antigen-antibody pairs, as well by a single well in the binding free energy. Additionally, AFS and SPR show that no interaction exists between wild type p53 and p73. The interaction between mutp53R175H and p73 deserves a high physiological relevance in cancer since the subsequent impairment of the p73 vicarious function of wtp53 would result in a marked chemoresistance of tumour cells (*Di Como et al., 1999; Strano et al., 2000; Di Agostino et al., 2008*). Collectively, our results strongly suggest that the mutp53R175H/p73 complex could be a potential target for innovative pharmaceutical drugs. These indeed by binding to the mutp53R175H, could induce crucial conformational changes of the protein able to prevent its binding to p73 or could break the mutp53R175H/p73 complex restoring the p73 transcriptional and pro-apoptotic function. At least, the safeguard of the p73 anti-proliferative activity may reduce the aggressiveness of cancerous cells carrying mutp53R175H protein and, at the same time, make them more responsive to common chemotherapeutic agents. It would be interesting to extend the present

investigation approaches to study the interaction between p73 and other p53 mutants, also with the aim of screening suitable drugs able to inhibit the formation of the corresponding complexes.

References

Bergamaschi D, Gasco M, Hiller L, Sullivan A, Syed N, Trigiante G, Yulug I, Merlano M, Numico G, Comino A, Attard M, Reelfs O, Gusterson B, Bell AK, Heath V, Tavassoli M, Farrell PJ, Smith P, Lu X, Crook T. 2003. p53 polymorphism influences response in cancer chemotherapy via modulation of p73-dependent apoptosis. *Cancer Cell* **3**: 387–402.

Bell GI. 1978. Models for the specific adhesion of cells to cells. *Science* **200**: 618–627.

Bizzarri AR, Cannistraro S. 2009. Atomic Force Spectroscopy in biological complexes formation: strategies and perspectives. *J. Phys. Chem. B* **113:** 16449-16464.

Bizzarri AR, Cannistraro S. 2010. The application of atomic force spectroscopy to the study of biological complexes undergoing a biorecognition process. *Chem. Soc. Rev.* **39**: 734-749.

Bizzarri AR, Santini S, Coppari E, Bucciantini M, Di Agostino S, Yamada T, Beattie CW, Cannistraro S. 2011. Interaction of an Anticancer Peptide Fragment of Azurin with p53 and its Isolated Domains studied by Atomic Force Spectroscopy. *Int. J. Nanomedicine* **6**: 3011-3019.

Björquist P, Boström S. 1997. Determination of the kinetic constants of tissue factor/factor VII/factor VIIA and antithrombin/heparin using surface plasmon resonance. *Thromb. Res*. **85:** 225-236.

Collavin L, Lunardi A, Del Sal G. 2010. p53-family proteins and their regulators: hubs and spokes in tumor suppression. *Cell. Death. Differ*. **17**: 901-911.

Cooper MA. 2003. Label-free screening of bio-molecular interactions. *Anal. Bioanal. Chem.* **377**: 834-842.

Di Agostino S, Strano S, Emiliozzi V, Zerbini V, Mottolese M, Sacchi A, Blandino G, Piaggio G. 2006. Gain of function of mutant p53: the mutant p53/NF-Y protein complex reveals an aberrant transcriptional mechanism of cell cycle regulation. *Cancer Cell* **10**: 191-202.

Di Agostino S, Cortese G, Monti O, Dell'Orso S, Sacchi A, Eisenstein M, Citro G, Strano S, Blandino G. 2008. The disruption of the protein complex mutantp53/p73 increases selectively the response of tumor cells to anticancer drugs. *Cell Cycle* **7**: 3440-3447.

Di Como CJ, Gaiddon C, Prives C. 1999. p73 function is inhibited by tumor-derived p53 mutants in mammalian cells. *Mol. Cell. Biol*. **19**: 1438-1449.

Ebner A, Hinterdorfer P, Gruber HJ. 2007. Comparison of different aminofunctionalization strategies for attachment of single antibodies to AFM cantilevers**.** *Ultramicroscopy* **107**: 922–927.

Evans E, Ritchie K. 1997. Dynamic strength of molecular adhesion bonds. *Biophys. J.* **72**: 1541–1555.

Flores ER, Sengupta S, Miller JB, Newman JJ, Bronson R, Crowley D, Yang A, McKeon F, Jacks T. 2005. Tumor predisposition in mice mutant for p63 and p73: evidence for broader tumor suppression functions for the p53 family. *Cancer Cell* **7**: 363–373.

Fontemaggi G, Dell'Orso S, Trisciuoglio D, Shay T, Melucci E, Fazi F, Terrenato I, Mottolese M, Muti P, Domany E, Del Bufalo D, Strano S, Blandino G. 2009. The execution of the transcriptional axis mutant p53, E2F1 and ID4 promotes tumor neo-angiogenesis. *Nat. Struct. Mol. Biol*. **16**: 1086-1893.

Friedsam C, Wehle AK, Kuhner F, Gaub HE. 2003. Dynamic single molecule force spectroscopy: bond rupture analysis with variable spacer length. *J. Phys. Condens. Matter* **15**: S1709–1723.

Glaser RW. 1993. Antigen-antibody binding and mass transport by convection and diffusion to a surface: a two-dimensional computer model of binding and dissociation kinetics. *Anal. Biochem.* **213**: 152-161.

Greenblatt MS, Bennett WP, Hollstein M, Harris CC. 1994. Mutations in the p53 tumor suppressor gene: clues to cancer etiology and molecular pathogenesis. *Cancer Res*. **54**: 4855–4878.

Homola J, Yee SS, Gauglitz G. 1999. Surface plasmons resonance sensors: review. *Sens. Actuators B* **54**: 3-15.

Hutter JL, Bechhoefer J. 1993. Calibration of atomic-force microscope tips. *Rev. Sci. Instrum.* **64**: 1868–1873.

Irwin MS, Kondo K, Marin MC, Cheng LS, Hahn WC, Kaelin WG Jr. 2003. Chemosensitivity linked to p73 function. *Cancer Cell* **3**: 403-410.

Johnsson B, Löfås S, Lindquist G. 1991. Immobilization of proteins to a carboxymethyldextran-modified gold surface for biospecific interaction analysis in surface plasmon resonance sensors. *Anal. Biochem*. **198**: 268-277.

Jost CA, Marin MC, Kaelin WG Jr. 1997. p73 is a simian [correction of human] p53-related protein that can induce apoptosis. *Nature* **389**: 191-194.

Kaelin WG Jr. 1999. The p53 gene family. *Oncogene* **18**: 7701-7705.

Kaghad M, Bonnet H, Yang A, Creancier L, Biscan JC, Valent A, Minty A, Chalon P, Lelias JM, Dumont X, Ferrara P, McKeon F, Caput D. 1997. Monoallelically expressed gene related to p53 at 1p36, a region frequently deleted in neuroblastoma and other human cancers. *Cell* **90***:* 809-819.

Karlsson R, Katsamba PS, Nordin H, Pol E, Myszka DG. Analyzing a kinetic titration series using affinity biosensors. *Anal. Biochem*. **349**: 136-147.

Lane DP. 1992. Cancer. p53, guardian of the genome. *Nature* **358:** 15-16.

Levine AJ. 1997. p53, the cellular gatekeeper for growth and division. *Cell* **88**: 323-331.

Lunghi P, Costanzo A, Mazzera L, Rizzoli V, Levrero M, Bonati A. 2009. The p53 family protein p73 provides new insights into cancer chemosensitivity and targeting. *Clin. Cancer. Res*. **15**: 6495-6502.

Merkel R, Nassoy P, Leung A, Ritchie K, Evans E. 1999. Energy landscapes of receptor-ligand bonds explored with dynamic force spectroscopy. *Nature* **397**: 50-53.

Morfill J, Blank K, Zahnd C, Luginbühl B, Kühner F, Gottschalk KE, Gottschalk KE, Plückthun A, Gaub HE. 2007. Affinity-Matured Recombinant Antibody Fragments Analyzed by Single-Molecule Force Spectroscopy. *Biophys. J.* **93**: 3583-3590.

Morton TA, Myszka DG, Chaiken IM. 1995. Interpreting complex binding kinetics from optical biosensors: a comparison of analysis by linearization, the integrated rate equation, and numerical integration. *Anal. Biochem.* **227:** 176-185.

Morton TA, Myszka DG. 1998. Kinetic analysis of macromolecular interaction using surface Plasmon resonance biosensors. *Methods Enzymol.* **295:** 268-294.

Myszka DG. 1999. Improving biosensor analysis. *J. Mol. Recognit.* **12**: 279–284.

O'Shannessy DJ, Brigham-Burke M, Soneson KK, Hensley P, Brooks I. Determination of rate and equilibrium binding constants for macromolecular interactions using surface plasmon resonance: use of nonlinear least squares analysis methods. *Anal. Biochem.* **212:** 457-468.

Prives C, Hall PA. 1999. The p53 pathway. *J. Pathol.* **187**: 112-126.

Rich RL, Myszka DG. 2000. Advances in surface Plasmon resonance biosensor analysis. *Curr. Opin. Biotechnol*. **11**: 54-61.

Schmale H, Bamberger C. 1997. A novel protein with strong homology to the tumor suppressor p53. *Oncogene* **15:** 1363-1367.

Sigal A, Rotter V. 2000. Oncogenic mutations of the p53 tumor suppressor: the demons of the guardian of the genome. *Cancer Res.* **60**: 6788-6793.

Stambolsky P, Tabach Y, Fontemaggi G, Weisz L, Maor-Aloni R, Siegfried Z, Shiff I, Kogan I, Shay M, Kalo E, Blandino G, Simon I, Oren M, Rotter V. 2010. Modulation of the vitamin D3 response by cancer-associated mutant p53. *Cancer Cell* **17**: 273-285.

Strano S, Munarriz E, Rossi M, Cristofanelli B, Shaul Y, Castagnoli L, Levine AJ, Sacchi A, Cesareni G, Oren M, Blandino G. 2000. Physical and functional interaction between p53 mutants and different isoforms of p73. *J. Biol. Chem.* **275**: 29503-29508.

Strano S, Fontemaggi G, Costanzo A, Rizzo G, Monti O, Baccarini A. 2002. Physical interaction with human tumor derived p53 mutants inhibits p63 activities. *J. Biol. Chem.* **277**: 18817-18826.

Strano S, Dell'Orso S, Di Agostino S, Fontemaggi G, Sacchi A, Blandino G. 2007. Mutant p53: an oncogenic transcription factor. *Oncogene* **26**: 2212-2219.

Taranta M, Bizzarri AR, Cannistraro S. 2008. Probing the interaction between p53 and the bacterial protein azurin by Single Molecule Force Spectroscopy. *J. Mol. Recognit.* **21**: 63-70.

Vogelstein B, Lane D, Levine AJ. 2000. Surfing the p53 network. *Nature* **408**: 307-310.

Weisz L, Damalas A, Liontos M, Karakaidos P, Fontemaggi G, Maor-Aloni R, Kalis M, Levrero M, Strano S, Gorgoulis VG, Rotter V, Blandino G, Oren M. 2007. Mutant p53 enhances nuclear factor kappaB activation by tumor necrosis factor alpha in cancer cells. *Cancer Res*. **67:** 2396-2401.

Chapter 5

Binding of azurin to cytochrome c 551 as investigated by surface plasmon resonance and fluorescence

Abstract

The interaction between azurin (Az) and cytochrome c 551 (CytC551) from *Pseudomonas aeruginosa* deserves particular interest for both its physiological aspects and their possible applications in bionano devices. Here, the kinetics of the interaction has been studied by surface plasmon resonance and fluorescence quenching. Surface plasmon resonance data have been successfully interpreted by the heterogeneous ligand model, which predicts the existence of two binding sites on the immobilized Az for CytC551 molecules in solution. On the other hand, the fluorescence study indicates the formation of a complex, with the involvement of the lone Az tryptophan (Trp) at position 48. The two different techniques point out the occurrence of an encounter complex between Az and CytC551 that evolves toward the formation of a more stable complex characterized by an equilibrium dissociation constant K_D typical of transient interactions.

The results presented in this chapter have been published as:

Santini S, Bizzarri AR, Yamada T, Beattie CW, Cannistraro S. 2014. Binding of azurin to cytochrome c 551 as investigated by surface plasmon resonance and fluorescence. *J. Mol. Recognit.* **27**: 124-130.

Introduction

Redox metalloproteins have gained in recent years a particular interest for their application in molecular bionanoelectronics (*Gorton et al., 1999; Willner and Willner, 2001; Adams et al., 2003; Jain, 2005; Guo and Dong, 2009; Prabhulkar et al., 2012*). Their very efficient electron transfer (ET) capability, as well as their property of recognizing the partner in a specific way (*Janin, 2000*), can be combined with the progress of microelectronics and nano-electronics to create hybrid systems to use as fast and sensitive biosensors (*Marvin and Hellinga, 2001; Andolfi and Cannistraro, 2005; Bonanni et al., 2005*). The ET process occurring between a metalloprotein, coupled with an electrode, and its partner in solution, requires a specific biorecognition event promoting the formation of a complex, likely characterized by a transient interaction and by a high physiological turnover. Indeed, equilibrium dissociation constants ($K_D = k_{off}/k_{on}$) in the 10^{-3}–10^{-6}M range have been registered for these complexes (*Crowley and Ubbink, 2003; Nooren and Thornton, 2003*).

Among ET proteins, blue copper proteins deserve particular interest (*Solomon et al., 1992*) They are biomolecules acting as mobile electron carriers in a variety of biological processes, where the ET deeply involves the active site containing a copper ion, switching between the Cu^{+} and Cu^{2+} state. Within the active site, the Cu ion is coordinated to a number of the protein ligands, according to a particular tetrahedral geometry, which endows the biomolecule with a finely tuneable ET mechanism, rendering them good candidates for application in biosensors.

In particular, Az (*Nar et al., 1991; Solomon et al., 1992; Arcangeli et al., 1999; Webb and Loppnow, 1999*), a 128 amino acids blue copper protein, which is part of the respiratory chain of the denitrifying bacteria *Pseudomonas aeruginosa*, is one of the most attractive ET proteins for its peculiar optical and spectroscopic properties (*Sykes, 1991; Webb and Loppnow, 1999; Cimei et al., 2002*). In addition, the protein has attracted growing interest for its prominent anticancer role consequent to its interaction with the tumor suppressor p53 (*Yamada et al., 2002; Taranta et al., 2008*) and perhaps involving oxygen reactive species generation (*Liu et al., 2008; Bizzarri et al., 2012).*

The physiological partner of Az is CytC551 (*Matsuura et al., 1982; Gray and Winkler, 1996; Cutruzzolà et al., 2002; Ceruso et al., 2003*), a monomeric heme protein of 82 amino acids organized in four α-helixes. Several experimental evidences of an ET process occurring between Az and CytC551 have been provided (*Wilson et al., 1975; Silvestrini et al., 1982; Zannoni, 1989; Cutruzzolà et al., 2002*). Moreover, the formation of an Az–CytC551

complex, whose existence has been under debate for decades (*Cutruzzolà et al., 2002*), has been recently modeled by computational methods and then experimentally supported. In particular, docking and molecular dynamics simulations (*Bizzarri et al., 2007; Bizzarri, 2011*) have predicted the best structure of the complex (Fig. 5.1(A)). On the other hand, the complex has been investigated at single molecule level by atomic force spectroscopy, which has allowed the determination of the protein–protein interaction force and the dissociation rate for different immobilization strategies (*Bonanni et al., 2005; Bonanni et al., 2006*). However, the complex has not been completely characterized from a kinetic point of view. This would be conversely quite insightful for the elucidation of the ET mechanism and crucial for using the Az–CytC551 system in bioelectronic devices.

In this work, the Az–CytC551 interaction has been studied with surface plasmon resonance (SPR) and fluorescence quenching spectroscopy. SPR has emerged as a strategic tool especially suited for sensitive kinetic investigation, in real time and without any labeling, of binding processes between a molecule anchored to a substrate and its partner free in solution (*Homola et al., 1999; Cooper, 2003*). On the other hand, fluorescence quenching is a powerful technique to study protein–protein interactions involving tryptophan or tyrosine residues when both the partners are free in solution, as it happens in physiological conditions (*Lakowicz, 2006*). The binding kinetics obtained by adding progressively higher concentrations of CytC551 to an Az-containing sample has been followed by both the two approaches. The experimental data, analyzed even in terms of several binding models, have pointed out the occurrence of a specific complex between Az and CytC551, whose equilibrium dissociation constant K_D is consistent with transient interaction features.

Experimental methods

Protein expression and purification

Azurin from *P. Aeruginosa* was purchased from Sigma Aldrich (St. Louis, Mo) and used without further purification.

Recombinant CytC551 was purified as described previously (*Goto et al., 2003; Hiraoka et al., 2004*). *Escherichia coli* JCB7120 was used as a host strain for expression of cytochrome c551-encoding gene of *P. Aeruginosa*. The transformed E. coli cells were cultivated under anaerobic conditions at 37 °C in the minimal medium as described (*Hasegawa et al., 1999*). Periplasmic protein fractions were collected by cold osmotic shock. The CytC551 in the

periplasmic fraction were purified by ÄKTAprime plus FPLC system (GE Healthcare), and protein concentrations were determined by the Bio-Rad protein assay kit (Bio-Rad, Hercules, CA) with bovine serum albumin as a standard. The purity of CytC551 were assessed on SDS-PAGE gels stained with Coomassie Brilliant Blue and also immune blotting with polyclonal anti-CytC551 antibody (*Hiraoka et al., 2004*).

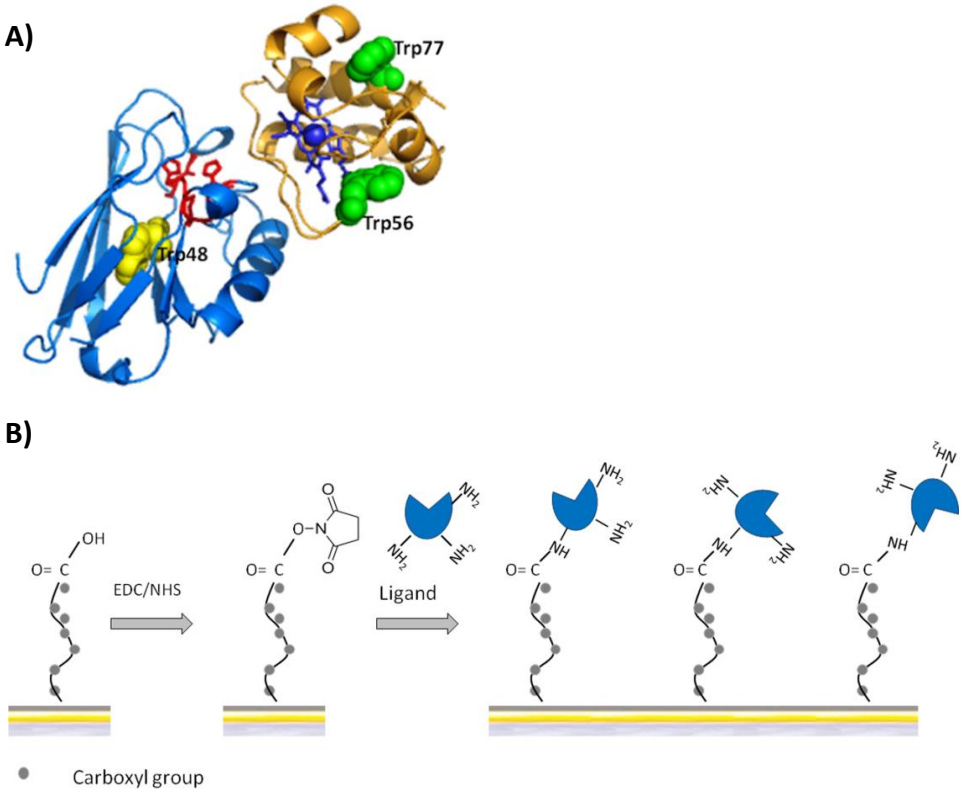

Figure 5.1. A) Three dimensional structure of the best complex between Az (blue) and CytC551 (orange) as predicted by the computational docking study reported in ref. 30. Az and CytC551 redox centers are shown as red and violet sticks respectively. Az Trp48 is shown as yellow spheres while green spheres in CytC551 represent its Trp77 and Trp56. **B)** Scheme of the immobilization strategy used in the SPR approach. First, the CM5 carboxymethylated dextran is activated by an EDC/NHS mixture, than the ligand (Az) is fluxed over the surface. The ligand immobilized through the NH_2 group of Lys residues is expected to be randomly oriented.

Surface plasmon resonance measurements

Surface plasmon resonance measurements were performed at 25 ° C using a Biacore X100 instrument (GE Healthcare, Bio-Sciences AB, Sweden). Experiments were carried out in 50-mMPBS buffer pH7.5 filtered with a 0.22-μM membrane filter, to which surfactant P20 0.005% (GE Healthcare) was added. Other reagents were all provided by GE Healthcare: CM5 sensor chip; Biacore Amine coupling Kit including N-hydroxyl-succinimide (NHS), N-ethyl-N-(3-diethylaminopropyl) carbodiimide (EDC) and ethanolamine hydrochloride 1MpH 8.5; acetate buffer pH 4 used as immobilization buffer; washing buffer SDS 0.05%.

In SPR measurements, Az molecules (ligand) were immobilized to a single channel of a CM5 sensor chip surface by targeting the amine groups of the lysine residues exposed on the protein surface.

To this aim, the standard amine coupling procedure (Fig. 5.1(B)) was used according to the manufacturer's instructions. Briefly, the COOH groups of the carboxymethylated dextran in the sensor chip were converted to active esters by mixing 100 μl 0.4M EDC with 100 μl 0.1M NHS from the amine coupling kit and injecting the mixture into the instrument at a flow rate of 10 μl/min for 7 min. The solution of Az, eluted up to a final concentration of about 0.06 μg/μl in 10 mM acetate buffer pH 4, was then injected over the activated surface until an immobilization level of about 200 resonance units (RU) was reached. Once the immobilization procedure was completed, nonspecifically bound proteins were removed by washing with running buffer until the RU value became nearly constant. Unreacted sites on the sensor chip were then masked by injecting 1M ethanolamine-HCl pH 8.5 for 7 min at flow rate of 10 μl/min. Running buffer was fluxed over the surface until the baseline was stable. The second (or reference) flow cell was instead activated and deactivated without coupling Az and used as a control surface for refractive index change and no specific binding.

Experiments were conducted via sequential injection of five flushes of CytC551 solution with increasing concentrations from 0.5 to $50 \cdot 10^{-6}$ M in running buffer flushed on the sensor chip surface at a flow rate of 30 μl/min for 120 s, followed by a 10-min dissociation time without intermediate regeneration. Analytical cycles were programmed by means of a wizard template, and the entire analysis was completely automated.

Experimental curves (sensorgrams) were double-reference subtracted (*Myszka, 1999*). In other words, the response collected over the functionalized surfaces was subtracted by the response from the reference surface to correct for bulk refractive index changes. Then, the

response from an average of blank injections was subtracted from the experimental response to remove any systematic artifact arising from the reaction flow and the reference cells.

The curves were then analyzed by nonlinear curve fitting of the entire data set with the BIAevaluation 2.0 software (GE Healthcare Bio-Sciences AB, Sweden). Fits were evaluated by visual inspection, χ^2 values, T-values, and observation of residual plot. They were accepted when χ^2 was <10, T value was >10, and when residuals were randomly distributed in a band as close as possible.

We also tried to covalently link CytC551 instead of Az to the chip according to the same amine coupling procedure described in the previous text. However, we did not reach the RU level necessary to perform a reliable kinetic study, this being likely a consequence of the unfavorable number and exposition of lysine residues on the CytC551 surface.

Steady-state fluorescence quenching measurements

Tryptophan fluorescence emission spectra were recorded at room temperature by a Spex FluoroMax (Jobin Yvon, France) spectrofluorimeter, equipped with a XBO 150W Xenon lamp (OSRAM GmbH, Munich, Germany). Samples were excited by a 290-nm wavelength (3 nm excitation bandwidth) so that excitation of tyrosine residues and energy transfer to the lone indole side chain were minimized. The light emitted by 500 µl of sample kept in a 0.2 × 1.0-cm internal size quartz cuvette was collected at right angle to the excitation radiation and scanned from 300 to 450 nm (3-nm emission bandwidth). An integration time of 1.0 s, related to 0.5 nm step, was used. Az sample 10 µM in sodium acetate buffer pH 4.6 was titrated with CytC551 at a final concentration ranging between 0 and 200 µM. The change in fluorescence emission intensity was measured within 1min after adding CytC551 to Az. Appropriate blanks corresponding to the buffer were subtracted to correct for Raman scattering background.

Results and Discussions

Surface plasmon resonance binding experiments

The interaction kinetics between CytC551 and Az has been studied by the SPR kinetic titration approach in which the analyte and the buffer solution are alternately injected into the cell containing the chip where the ligand has been immobilized (*Karlsson et al., 2006*). Such an approach is faster than the classical one because it does not require a complete

regeneration of the chip before each analyte injection. Furthermore, the immobilized target last longer and the ligand activity is fully preserved, this resulting in an increased efficiency and reduction of costs.

The resulting sawtooth SPR profile obtained from the successive injections of CytC551 solution at five progressively higher concentrations on the cell with Az is shown in Fig. 5.2 (continuous line).

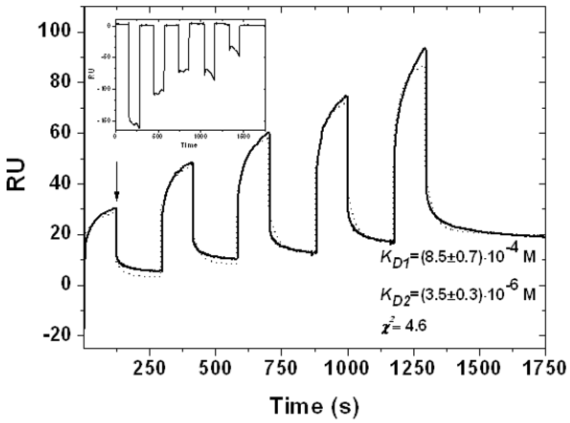

Figure 5.2. SPR sensorgram for the association and dissociation of CytC551 on Az- modified sensor chip surface (continuous line). The fit has been obtained by the heterogeneous ligand model (dashed line). The arrow indicates the first injection of the buffer. The global fitting procedure by Eq. 3-6, provided the following values for the k_{on} and k_{off} of the interaction: k_{on1}=(2.23±0.14) 10^2 M^{-1} s^{-1}; k_{off1}=(1.90±0.05) 10^{-1} s^{-1}; k_{on2}= (3.04±0.10) 10^2 M^{-1} s^{-1}; k_{off2}=(1.07±0.07) 10^{-3} s^{-1}. Inset: the binding isotherms for CytC551 with no ligand (Az) immobilized on the surface.

After the first injection with the CytC551 solution, the signal increases nonlinearly and approaches a plateau. At the end of the first CytC551 injection (see the arrow in Fig. 5.2), the buffer is flowed over the ligand and the signal drops down, followed by a slow decreasing trend down to zero until the successive CytC551 injection. Progressively higher signals are obtained as far as higher CytC551 concentrations are used.

The inset of Fig. 5.2, showing the binding isotherms for bare CytC551 with no ligand (Az) immobilized on the surface, displays a negligible increase of the baseline signal with respect to that observed on the cell with Az (about 2 RUs). This indicates that the progressive signal increase is due to a specific interaction of CytC551 to Az molecules immobilized on the chip. On the other hand, each buffer injection yields a decrease of the signal down to an almost

constant value different from zero and more and more higher at each step, this being ascribed to a partial dissociation of the previously formed complexes on the chip.

To extract information on the affinity between CytC551 and Az, we have analyzed the SPR data by fitting the whole SPR profile with several kinetic models by a nonlinear least square analysis (*Morton et al., 1995*). In particular, we have taken into account the classical Langmuir one-to-one, the heterogeneous ligand, the heterogeneous analyte, and the two-state binding models (*Schasfoort and Tudos, 2008*).

The Langmuir 1:1, or single-step binding model, provides the simplest approach to describe a ligand–analyte interaction, assuming a 1:1 interaction between the ligand (L), and the analyte (A) (*O'Shannessy et al., 1993; Björquist and Boström, 1997*). Such a model can be described by the following reaction equation:

$$L + A \underset{k_{off}}{\overset{k_{on}}{\rightleftarrows}} LA \qquad (1)$$

where k_{on} and k_{off} are the association and dissociation rates of the complex respectively, with the corresponding K_D being given by k_{off}/k_{on}. Here, the analyte is CytC551 and the ligand is Az. However, the best fit by this model does not allow us to reach a satisfactory description of SPR data with a χ^2 value higher than 10 (χ^2 = 12.6, not shown).

Similarly, both the heterogeneous analyte model and the two-state binding model were found not suitable to fit the experimental sensorgrams (data not shown). The former assumes that there are two independent reactions involving two different sites on the analyte (*Karlsson, 1994*), whereas the latter accounts for some conformational changes of the molecules upon forming complex (*De Crescenzo et al., 2000*). A good description of our SPR data has been instead obtained by the heterogeneous ligand model, which assumes the presence on the ligand of two binding sites (L_1 and L_2), each one binding one analyte molecule with different affinity (*O'Shannessy and Winzor, 1996*). Accordingly, the binding process can be described by:

$$L_1 + A \underset{k_{off1}}{\overset{k_{on1}}{\rightleftarrows}} L_1A \quad and \; L_2 + A \underset{k_{off2}}{\overset{k_{on2}}{\rightleftarrows}} L_2A \qquad (2)$$

where k_{onn} and k_{offn} (n=1 or 2) are the association and dissociation rates for the corresponding reactions, 1 or 2. The model is described by the following differential equations:

$$d[L_1]/dt = -(k_{on1} \cdot [L_1] \cdot [A] - k_{off1} \cdot [L_1A]) \quad (3)$$

$$d[AL_1]/dt = k_{on1} \cdot [L_1] \cdot [A] - k_{off1} \cdot [L_1A] \quad (4)$$

$$d[L_2]/dt = -(k_{on2} \cdot [L_2] \cdot [A] - k_{off2} \cdot [L_2A]) \quad (5)$$

$$d[AL_2]/dt = k_{on2} \cdot [L_2] \cdot [A] - k_{off2} \cdot [L_2A] \quad (6)$$

The best fit of the SPR data in the framework of this model is shown in Fig. 5.2 (dashed line) together with its χ^2 value and the K_D extracted for each ligand binding site. Association and dissociation rate constants of the interaction have been also extracted for each one of the two binding events. Specifically, we have found: k_{on1}= (2.23±0.14) 10^2 M^{-1} s^{-1}; k_{off1}=(1.90±0.05) 10^{-1} s^{-1}; k_{on2}= (3.04±0.10) 10^2 M^{-1} s^{-1}; k_{off2}=(1.07±0.07) 10^{-3} s^{-1}. The good χ^2 obtained (χ^2=4.6), the K_Ds values, and the sensorgram tendency towards the plateau indicate the formation of a complex between Az and CytC551 with a kinetics deviating from the pseudo-first order and involving two different Az binding sites. The K_{D1} dissociation constant, $K_{D1}=k_{off1}/k_{on1}$= (8.5±0.7)·10^{-4} M, is significantly higher than the values usually observed for biomolecular complexes, which range from 10^{-12} M for complexes characterized by an extremely high affinity, to 10^{-5} M for complexes with a very low affinity, including transient complexes (*Ubbink, 2009*). Accordingly, reaction 1 may correspond to an encounter interaction between the partners which likely does not give rise to the formation of a stable complex. Conversely, the second reaction, which is characterized by a lower dissociation constant $K_{D2}=k_{off2}/k_{on2}$=(3.5±0.3)·10^{-6} M could correspond to an interaction between CytC551 and Az typical of transient complexes. We note on passing that a dissociation constant of about 10^{-6} M has been obtained by SPR for a complex involving cytochrome c molecule and neuroglobin (*Bønding et al., 2008*). The existence of two Az binding sites for the interaction with CytC551 can be interpreted in terms of the so-called encounter complex model, which is often used to describe the formation of transient complexes between ET biomolecules (*Marcus and Sutin, 1985; Crowley and Ubbink, 2003; Ubbink, 2009).* Briefly, the binding process between two molecules takes place involving different steps: first, the two biomolecules form an encounter complex

typically guided by long range electrostatic forces; then, they undergo rotational, vibrational, and diffusional motions, giving rise to a specific reactive
interaction. Once this complex is formed, an ET process between the molecules takes place, followed by a dissociation of the complex itself to yield the products (*Ubbink, 2009*). Such a view could be consistent with the observation of two interaction sites, one with a low affinity, related to the formation of the encounter complex, and another one characterized by a much higher affinity, which describes the final complex between the molecules. However, we cannot rule out that the heterogeneity of the ligand immobilized on the chip could be responsible for the existence of two binding interactions (*Catimel et al., 1997*). Indeed, because Az is bound to the dextran matrix of a CM5 chip through amino groups attachment, the protein will be randomly oriented over the chip surface (Fig. 5.1(A)). Consequently, it could be likely that a subpopulation of bound molecules are oriented in such a way that they can have a different affinity for the partner or even they cannot participate in the binding reaction with CytC551. Accordingly, the two binding interactions could arise from the contribution of a weighted average of complexes with different affinity. Such a picture has been used to explain results from SPR experiments with a similar anchoring procedure (*De Crescenzo et al., 2000*).

Fluorescence quenching experiment

To get additional insight on the interaction between CytC511 and Az, we have followed the fluorescence emission of an Az solution, excited at a 290-nm wavelength after the addition of progressively higher concentrations of CytC551. When bare Az molecules in solution (10 μM) are excited at 290-nm wavelength, the corresponding emission spectrum is characterized by a peak at about 308nm (see the black dashed line in Fig. 5.3). Such a signal arises from the emission of the lone Az Trp (Trp48) (*Turoverov et al., 1985; Nar et al., 1991; Delfino and Cannistraro, 2009*), which is located in a highly hydrophobic environment (Fig. 5.1(A)). At the same excitation wavelength, the fluorescence emission spectrum of CytC551 shows a broad peak centered at about 348nm (see the inset of Fig. 5.3) (*Borgia et al., 2008*). Such a signal arises from the two CytC551 Trp residues, Trp77 and Trp56, the former occupying a marginal position with respect to the hydrophobic core of the protein and the latter being buried inside it (*Borgia et al., 2008*) (Fig. 5.1(A)). Because CytC551 Trps emission is situated well apart from that of the Az Trp, it is possible to distinguish the emission peak of

Az Trp48 from that of CytC551 in the mixed solution. Fluorescence emission spectra of Az titrated with CytC551 up to 15.7 μM are shown in Fig. 5.3. The intensity of the fluorescence peak at 308 nm, arising from the Az Trp48, is progressively reduced upon the addition of CytC551, without any wavelength shift of the maximum. At the same time, the fluorescence emission intensity at around 348 nm increases with the CytC551 concentration.

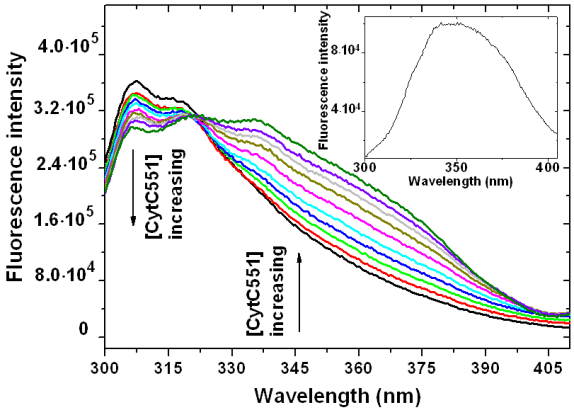

Figure 5.3. Representative fluorescence spectra of 10 μM Az in sodium acetate buffer pH 4.6 titrated by increasing CytC551 concentrations. Appropriate blanks corresponding to the buffer were subtracted to correct for Raman background. A quenching of the Az emission fluorescence of about 1.6% resulting from the dilution of the protein after CytC551 addition, has been considered and carefully added to the experimental spectra. Inset: fluorescence spectrum of CytC551 8.7 μM in acetate buffer pH 4.6 excited at 290 nm.

The fluorescence quenching of Az Trp48 is shown in Fig. 5.4, where the spectra of Fig. 5.3 have been carefully subtracted by the contribution of CytC551 to the fluorescence emission spectrum.

The quenching of the fluorescence emission at 308 nm after addition of CytC551, indicates a molecular interaction of CytC551 with Az, somewhat involving the lone Az Trp residue. It would be interesting therefore to ascertain if a dynamic or static process is responsible for such quenching; in other words if the quenching just arises from collisional encounters between the molecules, and then is dynamically controlled by diffusion, or, instead, by the formation of a specific complex between the two biomolecules, involving Trp48 of Az (*Lakowicz, 1999*).

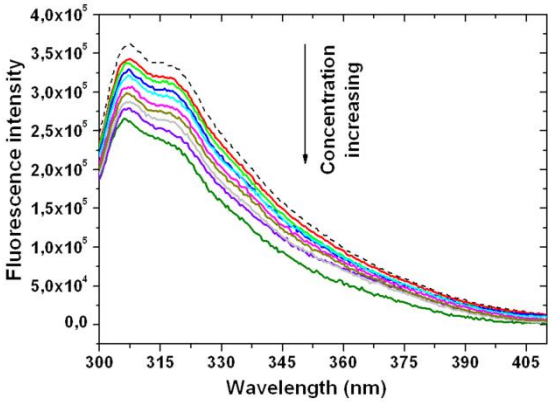

Figure 5.4. Fluorescence spectra showed in Fig. 5.3 subtracted by the contribution of CytC551 to the fluorescence.

The fluorescence quenching data have been thus analyzed by applying the Stern–Volmer equation given by:

$$\frac{F_0}{F} = 1 + k_q \tau_q [Q] = 1 + K_{SV}[Q] \qquad (7)$$

where F_0 and F are the fluorescence intensities in the absence and presence of the quencher respectively, k_q is the bimolecular quenching constant (or quenching rate constant), K_{SV} is the Stern-Volmer quenching constant of the interaction, providing information on the binding affinity, [Q] is CytC551 concentration and τ_q is the average lifetime of the fluorophore in the absence of quencher.

The Stern-Volmer plot of F_0/F vs CytC551 concentrations up to 30 μM, is shown in Fig. 5.5. At higher CytC551 concentrations the broad CytC551 emission peak centered at about 348 nm completely masks the Az Trp48 emission at 308 nm making the extraction of the F_0/F values practically unreliable. The plot reveals a linear trend which can be traced back to the involvement of a single Trp in the interaction with the quencher (Fig. 5.5). From the slope of the linear fit by Eq. 7, we have determined the Stern-Volmer quenching constant $K_{SV}=(0.024\pm0.001)\cdot10^6$ M^{-1}; the bimolecular quenching constant $k_q=K_{SV}/\tau_q$ can be also extracted upon estimating τ_q. A reasonable value for τ_q has been reported to be about 10^{-9} s (*Lakowicz, 1999*). Using such a value, we found that k_q turns out to be about 10^{13} M^{-1} s^{-1},

which is much higher than the limiting diffusion constant K_{diff} of the biomolecule (K_{diff} is about $2 \cdot 10^{10}$ M^{-1} s^{-1}) (*Myszka, 1999*). Therefore, we could rule out that the quenching of the Az fluorescence is due to a dynamic collisions. Instead, this fluorescence titration experiment could be indicative of a static quenching, confirming a specific interaction between CytC551 and Az with the involvement of the Az Trp residue. Indeed, the best predicted docking model indicated that the Az hydrophobic patch, which encompasses its Trp48 is in close proximity to the hydrophobic patch of CytC551, as shown in Fig. 5.1(A) (*Bizzarri et al., 2007*). Moreover, no shift of the maximum emission wavelength (at 308 nm) has been observed. Because of the high sensitivity of Trp residues emission to local environment (*Lakowicz, 2006*), the lack of the Az Trp48 emission shift could either indicate that the Trp48 environment has not been affected by an eventual Az conformational change, or the absence of any conformational change in the complex formation, in agreement with SPR results. Indeed, we recall that the two-state binding model assuming a conformational change of the complex after the interaction does not fit the SPR results.

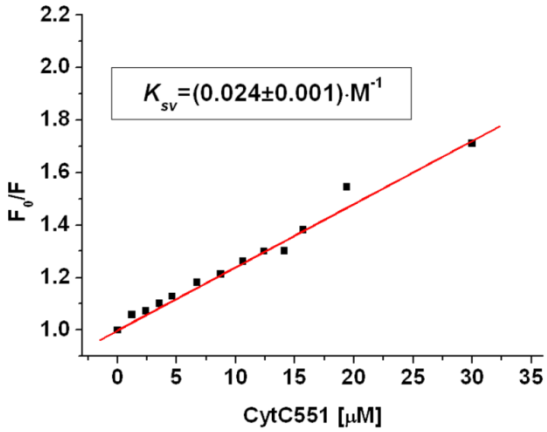

Figure 5.5. Stern – Volmer plot of Az fluorescence quenching as a function of CytC551 concentration. Continuous red line is the linear fit by Eq.7; the value of K_{SV} extracted from the fit being reported.

Fit of the data with Eq. 7, allowed us to estimate a $K_D=1/K_{SV}$ of $(4.2\pm0.2)\cdot10^{-5}$ M. Such a value falls in between the two values determined by SPR, $K_{D1}= (8.5\pm0.7)\cdot10^{-4}$ M and $K_{D2}=(3.5\pm0.3)\cdot10^{-6}$ M, in the framework of the heterogeneous model. Although such value is again indicative of the formation of a transient complex, the difference could be due to

the different conditions of the two experimental setup. While in SPR measurements, the ligand molecules are immobilized on the substrate and the analyte is in solution, in fluorescence experiment, both partners are free in solution, and this could lead to a somewhat different binding response between the two partners. In addition, fluorescence quenching method is able to monitor only the change in the microenvironment of Trp residues. This means that the method does not consider binding sites not involving Trps. Conversely, SPR monitors refractive index change upon binding interaction, and when proteins interact, the signal is generated independently from the binding site localization. It is thus possible that the K_D found in the fluorescence quenching experiment is the weighted average of complexes having different affinity (perhaps encounter and stable final complex) and that the binding sites of these complexes does not always involve Az Trp residue in the interaction. The fact that the kinetic results depend, at least in part, on the experimental technique used, should be taken into account when kinetic data from molecules in solution are extrapolated to immobilized biomolecules, as those reacting in biosensors.

Conclusions

The study of the interaction between the ET proteins Az and CytC551 by SPR and fluorescence quenching has allowed us to show the formation of a specific complex between the two biomolecules. An analysis of the SPR data in terms of the heterogeneous ligand model indicates that the binding process takes place through two independent reactions likely involving two sites of the Az molecules immobilized on the chip. This result could be traced back to the formation of an encounter complex between partners which then evolves towards the final, more stable arrangement. However, we cannot rule out that the existence of two binding interactions is the consequence of some heterogeneity in the binding properties of Az randomly immobilized on the chip. The values of the estimated dissociation constants are consistent with the formation of a transient complex in agreement with the electron transfer capability between Az and CytC551. On the other hand, emission fluorescence of the single Az Trp residue upon the addition of CytC551 at increasing concentrations shows the formation of a complex with the involvement of a single binding site close to the Az Trp residue close to the HP of the protein. No shift of Trp 48 emission has been observed after CytC551 binding, this suggesting that there is not a significant Az conformational change in complex formation. These results confirm the

prediction of previous computational docking and molecular dynamic simulation studies. The K_D value, as determined by fluorescence, reflects a high turnover of the complex again consistent with the transient character of the Az-CytC551 interaction. The fact that the K_D estimated by fluorescence is between the two values determined by SPR could be attributed to the different experimental conditions used in the two cases: in SPR experiment, one of the two partners, Az, is bound to a substrate, whereas in fluorescence, both partners are free in solution. In addition while SPR monitors all the interactions independently from the binding site localization, in fluorescence spectroscopy only complexes whose formation affect the Trp environment are considered. Such an aspect deserves some interest in the perspective to use these proteins as integrated in bio-nano-devices. In summary, the characterization of the kinetic properties of the Az-CytC551 complex, obtained by SPR and fluorescence, integrates the picture emerging from previous single molecule studies by Atomic Force Spectroscopy (*Bonanni et al., 2005; Bonanni et al., 2006*), by providing a more insightful view of the Az-CytC551 interaction. In particular, the kinetics of this complex seems to be consistent with the ET process occurring between Az and CytC551, and this may deserve some interest for possible application in molecular biosensors.

References

Adams DM, Brus L, Chidsey CED, Creager S, Creutz C, Kagan CR, Kamat PV, Lieberman XM, Lindsay S, Marcus RA, Metzger RM, Michel-Beyerle ME, Miller JR, Newton MD, Rolison DR, Sankey O, Schanze KS, Yardley J, Zhu X. 2003. Charge transfer on the nanoscale: current status. *J. Phys. Chem. B* **107**: 6668–6697.

Andolfi L, Cannistraro S. 2005. Conductive atomic force microscopy study of plastocyanin adsorbed on gold electrode. *Surf. Science* **598:** 68–77.

Arcangeli C, Bizzarri AR, Cannistraro S. 1999. Long term molecular dynamics simulations of Azurin: structure, dynamics and functionality. *Biophys. Chem*. **78:** 247–257.

Bizzarri AR, Brunori E, Bonanni B, Cannistraro S. 2007. Docking and Molecular Dynamics Simulation of the Azurin-Cytochrome c551 Electron Transfer Complex. *J. Mol. Recognit*. **20**: 122-131.

Bizzarri AR. 2011. Steered Molecular Dynamics Simulations of the Electron Transfer Complex between Azurin and Cytochrome c551. *J. Phys. Chem. B* **115**:1211-1219.

Bizzarri AR, Brida D, Santini S, Cerullo G, Cannistraro S. 2012. Ultrafast pump-probe study of the excited-state charge-transfer dynamics in blue copper rusticyanin. *J. Phys. Chem. B* **116**: 4192-4198.

Björquist P, Boström S. 1997. Determination of the kinetic constants of tissue factor/factor VII/factor VIIA and antithrombin/heparin using surface plasmon resonance. *Thromb. Res.* **85:** 225-236.

Bonanni B, Kamruzzahan ASM, Bizzarri AR, Rankl C, Gruber HJ, Hinterdorfer P, Cannistraro S. 2005. Single molecule recognition between cytochrome C 551 and gold-immobilized Azurin by force spectroscopy. *Biophys. J.* **89**: 2783–2791.

Bonanni B, Bizzarri AR, Cannistraro S. 2006. Optimized Biorecognition of Cytochrome c 551 and Azurin Immobilized on Thiol-Terminated Monolayers Assembled on Au(111) Substrates. *J. Phys. Chem. B* **110:** 14574-14580.

Bønding SH, Henty K, Dingley AJ, Brittain T. 2008. The binding of cytochrome c to neuroglobin: a docking and surface plasmon resonance study. *Int. J. Biol. Macromol*. **43**: 295-299.

Borgia A, Gianni S, Brunori M, Travaglini-Allocatelli C. 2008. Fast folding kinetics and stabilization of apo-cytochrome c. *FEBS Lett.* **582**:1003–1007.

Catimel B, Nerrie M, Lee FT, Scott AM, Ritter G, Welt S, Old LJ, Burgess AW, Nice EC. 1997. Kinetic analysis of the interaction between the monoclonal antibody A33 and its colonic epithelial antigen by the use of an optical biosensor. A comparison of immobilization strategies. *J. Chromatogr. A* **776**: 15–30.

Ceruso MA, Grottesi A, Di Nola A. 2003. Dynamic effects of mutations within two loops of cytochrome c(551) from Pseudomonas aeruginosa. *Proteins* **50:** 222–229.

Cimei T, Bizzarri AR, Cannistraro S, Cerullo G, De Silvestri S. 2002. Vibrational coherence in Azurin with impulsive excitation of the LMCT absorption band. *Chem. Phys. Lett.* **362:** 497-503.

Cooper MA. 2003. Label-free screening of bio-molecular interactions. *Anal. Bioanal. Chem.* **377**: 834-842.

Crowley PB, Ubbink M. 2003. Close encounters of the transient kind: protein interactions in the photosynthetic redox chain investigated by NMR spectroscopy. *Acc. Chem. Res.* **36**: 723–730.

Cutruzzolà F, Arese M, Ranghino G, Van Pouderoyen G, Canters G, Brunori M. 2002. Pseudomonas aeruginosa cytochrome C-551: probing the role of the hydrophobic patch in electron transfer. *J. Inorg. Biochem.* **88:** 353–361.

De Crescenzo G, Grothe S, Lortie R, Debanne MT, O'Connor-McCourt M. 2000. Real-Time Kinetic Studies on the Interaction of Transforming Growth Factor alpha with the Epidermal Growth Factor Receptor Extracellular Domain Reveal a Conformational Change Model. *Biochem.* **39:** 9466-9476.

Delfino I, Cannistraro S. 2009. Optical investigation of the electron transfer protein azurin-gold nanoparticle system. *Biophys. Chem.* **139:** 1-7.

Gorton L, Lindgren A, Larsson T, Munteanu FD, Ruzgas T, Gazaryan I. 1999. Direct electron transfer between heme-containing enzymes and electrodes as basis for third generation biosensors. *Anal. Chim. Acta*. **400**:91–108.

Goto M, Yamada T, Kimbara K, Horner J, Newcomb M, Das Gupta TK, Chakrabarty AM. 2003. Induction of apoptosis in macrophages by Pseudomonas aeruginosa azurin: tumour-suppressor protein p53 and reactive oxygen species, but not redox activity, as critical elements in cytotoxicity. *Mol. Microbiol.* **47:** 549–559.

Gray HB, Winkler JR. 1996. Electron transfer in proteins. *Ann. Rev. Biochem.* **65**: 537–561.

Guo S, Dong S. 2009. Biomolecule-nanoparticle hybrids for electrochemical biosensors. *Trends Anal. Chem.* **28**: 96-109.

Hasegawa J, Shimahara H, Mizutani M, Uchiyama S, Arai H, Ishii M, Kobayashi Y, Ferguson SJ, Sambongi Y, Igarashi Y. 1999. Stabilization of Pseudomonas aeruginosa Cytochromec 551 by Systematic Amino Acid Substitutions Based on the Structure of Thermophilic Hydrogenobacter thermophilus Cytochrome c 552. *J. Biol. Chem.* **274**: 37533-37537.

Hiraoka Y, Yamada T, Goto M, Das Gupta TK, Chakrabarty AM. 2004. Modulation of mammalian cell growth and death by prokaryotic and eukaryotic cytochrome c. *Proc. Natl. Acad. Sci. USA*. **101**: 6427-6432.

Homola J, Yee SS, Gauglitz G. 1999. Surface plasmons resonance sensors: review. *Sens. Actuators B* **54**: 3-15.

Jain KK. 2005. Nanotechnology in clinical laboratory diagnostics. *Clin. Chim. Acta* **358**: 37-54.

Janin J. 2000. Kinetics and thermodynamics of protein-protein interactions; In *Protein-Protein Recognition*. Oxford University Press: New York.

Karlsson R**.** 1994. Real-time competitive kinetic analysis of interactions between low-molecular-weight ligands in solution and surface-immobilized receptors. *Anal. Biochem.* **221:** 142-151.

Karlsson R, Katsamba PS, Nordin H, Pol E, Myszka DG. 2006. Analyzing a kinetic titration series using affinity biosensors. *Anal. Biochem.* **349**: 136-147.

Lakowicz JR. 1999. Principles of Fluorescence Spectroscopy. 2nd edn. Plenum Press, New York.

Lakowicz JR. 2006. Principles of Fluorescence Spectroscopy. 3rd edn. Springer, New York.

Liu B, Chen Y, St. Clair DK. 2008. ROS and p53: versatile partnership. *Free Radical Bio. Med.* **44**: 1529−1535.

Marcus RA, Sutin N. 1985. Electron transfer in chemistry and biology. *Biochim. Biophys. Acta* **811:** 265–322.

Marvin JS, Hellinga HW. 2001. Conversion of a maltose receptor into a zinc biosensor by computational design . *Proc. Natl. Acad. Sci. USA* ***98***: 4955–4960.

Matsuura Y, Takano, T, Dickerson RE. 1982. Structure of cytochrome c551 from Pseudomonas aeruginosa refined at 1.6 A resolution and comparison of the two redox forms. *J. Mol. Biol*. **156:** 389-409.

Morton TA, Myszka DG, Chaiken IM. 1995. Interpreting complex binding kinetics from optical biosensors: a comparison of analysis by linearization, the integrated rate equation, and numerical integration. *Anal. Biochem.* **227**: 176-185.

Myszka DG. 1999. Improving biosensor analysis. *J. Mol. Recognit.* **12**: 279 – 284.

Nar H, Messerschmidt A, Huber R, Van de Kamp M, Canters GW. 1991. Crystal structure analysis of oxidized Pseudomonas aeruginosa azurin at pH 5.5 and pH 9.0. A pH-induced conformational transition involves a peptide bond flip. *J. Mol. Biol.* **221:** 765–772.

Nooren IM, Thornton JM. 2003. Structural characterisation and functional significance of transient protein–protein interactions. *J. Mol. Biol.* **325**:991–1018.

O'Shannessy DJ, Brigham-Burke M, Soneson KK, Hensley P, Brooks I. 1993. Determination of rate and equilibrium binding constants for macromolecular interactions using surface plasmon resonance: use of nonlinear least squares analysis methods. *Anal. Biochem.* **212:** 457-468.

O'Shannessy DJ, Winzor DJ. 1996. Interpretation of Deviations from Pseudo-First-Order Kinetic Behavior in the Characterization of Ligand Binding by Biosensor Technology. *Anal. Biochem.* **236***:* 275–283.

Prabhulkar S, Tian H, Wang X, Zhu JJ, Li CZ. 2012. Engineered proteins: redox properties and their applications. *Antioxid. Redox Signal* **17**: 1796-1822.

Schasfoort RBM, Tudos AJ. 2008. Handbook of Surface Plasmon Resonance. Royal Society of Chemistry, London.

Silvestrini MC, Tordi MG, Colosimo A, Antonini E, Brunori M. 1982. The kinetics of electron transfer between Pseudomo-nas Aeruginosa cytochrome c-551 and its oxidase. *Biochem. J.* **203:** 445–451.

Solomon EI, Baldwin MJ, Lowery MD. 1992. Electronic Structure of Active Sites in Copper Proteins: Contributions to Reactivity. *Chem. Rev.* **92**: 521-542.

Sykes AG. 1991. Active-Site Properties of the Blue Copper Proteins. *Adv. Inorg. Chem.* **36**: 377-408.

Taranta M, Bizzarri AR, Cannistraro S. 2008. Probing the interaction between p53 and the bacterial protein azurin by Single Molecule Force Spectroscopy. *J. Mol. Recognit.* **21**: 63−70.

Turoverov KK, Kuznetsova IM, Zaitsev VN. 1985. The environment of the tryptophan residue in Pseudomonas Aeruginosa azurin and its fluorescence properties. *Biophys. Chem.* **23:** 79–89.

Ubbink, M. 2009. The courtship of proteins: Understanding the encounter complex. *Febs Lett.* **583**: 1060-1066.

Webb MA, Loppnow GRA. 1999. Structural basis for long-range coupling in Azurins from resonance raman spectroscopy. *J. Phys. Chem. A* **103:** 6283–6287.

Willner I, Willner B. 2001. Biomaterials integrated with electronic elements: en route to bioelectronics. *Trends Biotechnol*. **19**: 222–230.

Wilson MT, Greenwood C, Brunori M, Antonini E. 1975. Electron transfer between azurin and cytochrome c-551. *Biochem. J.* **145**: 449–457.

Yamada T, Goto M, Punj V, Zaborina O, Chen ML, Kimbara K, Majumdar D, Cunningham E, Das Gupta TK, Chakrabarty AM. 2002. Bacterial redox protein azurin, tumor suppressor protein p53, and regression of cancer. *Proc. Natl. Acad. Sci. USA* **99:** 14098-14103.

Zannoni D. 1989. The respiratory chains of pathogenic pseudomonas. *Biochim. Biophys. Acta* **975**: 299–316.

Chapter 6

Conclusions and perspectives

In this thesis a kinetic and molecular characterization of biomolecular recognitions of pharmaceutical interest, is presented. Atomic Force Spectroscopy (AFS) and Surface Plasmon Resonance (SPR), also complemented by docking, molecular dynamic simulations, and fluorescence spectroscopy studies, have been applied to characterize molecular interactions involving oncosuppressor p53 and p53 family proteins on one hand, and protein and peptides with anticancer activity on the other.

Great attention has been devoted to define at the molecular level the anticancer mode of action of the cell penetrating peptide p28, a 28 amino acids peptide fragment derived from the electron transfer protein Azurin and which shows a strong anticancer activity in some way connected with its interaction with p53. The combined approach based on both experimental and computational methods has allowed to define the molecular and kinetic details of the interaction between p28 and p53 full length and its fragments. These data, combined with results from most common biochemical approaches, have allowed to conclusively delineate the p28 mode of action. It emerged that p28 binds to the Dna-binding domain (DBD) of p53 at level of its L_1 loop (aa 112–124) and additional motifs within the binding regions of ubiquitin ligase COP1. Subsequent inhibition of the COP1 interaction with p53 and the COP1-mediated p53 proteasomal degradation results in the p53 stabilization and increase of its intracellular levels. Active p53 thus up regulates the downstream molecules p21 and p27 in p53 wild type and, at least, some p53 mutant cancer cells, down regulating FoxM1, and leading to the inhibition of cell cycle at G_2–M phase (Fig. 6.1).

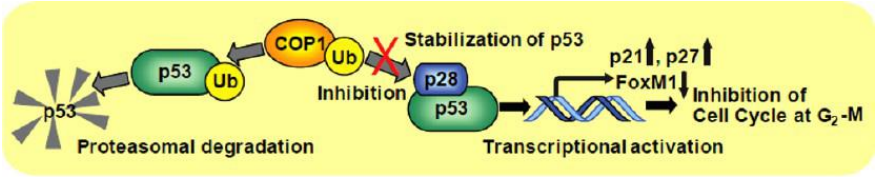

Figure 6.1. Scheme of the p28 mode of action. Figure is from *Yamada et al., 2013*. *Mol. Pharm*. ***10***: 3375–3383.

The p28 mode of action determined, its interaction with both non physiological (L114D, A119D, C124D, C229D) and physiological DBD mutants (K164, R273, P223/V274F) has been investigated by AFS. Obtained data have been analyzed in connection with molecular dynamic simulation and Raman spectroscopy studies in order to get insight into the possible connection between mutation induced DBD changes in term of conformation and surface hydrophobicity, and the p28 binding capability, both virtual and experimental. From such a comprehensive study it emerged that a mutation induced reduction in β-sheet content of specific motifs within the p53 DBD is associated with a loss of secondary structure which reduces the integrity of the p28 binding to the p53 DBD; all the mentioned data being gathered in a preliminary draft. Further studies aimed at define how p28 and similar proteins stabilize wild type and mutated p53 would improve the performance of these type of agents and could certainly help oncologists identifying which patients are most likely to respond to drug.

p53 stabilization through the inhibition of its interaction with ubiquitin ligases is only one of the appealing strategies that could be adopted to treat cancer. In fact, in addition to dominant negative activity and loss of wild type function, mutant p53 can also acquire oncogenic properties such as the ability to inhibit the function of p63 and p73 by protein-protein interaction thus making cancer cells more aggressive. In particular, the p73 loss of function consequent to its possible interaction with mutant p53 seems to be a major determinant of human tumour chemoresistance. There is thus a large interest in searching for drug able to hamper the mutant p53 interaction with p73 in order to restore the p73 anticancer activity.

In connection with this however it appears crucial to first unravel the molecular and kinetic details of the mutantp53/p73 interaction. To this aim AFS and SPR have thus been applied. The formation of a stable complex has been demonstrated, characterized by a K_D n the order of 10^{-7} M, as expected for specific interactions. No binding was instead observed between p73 and wild type p53. In the future, it could be certainly interesting to investigate by our combined approach the kinetics of the interaction between p53R175H and p63 and, then, search for molecules able to hamper or reduced the rate of such interactions.

Finally, collaterally to the main project, this work has also get insight the molecular and kinetic details of the interaction between electron transfer protein Azurin and its physiological partner Cytochrome C551, by Surface Plasmon Resonance and fluorescence. The study, pointing out the occurrence of an encounter complex between Azurin and Cytochrome C551

that evolves toward the formation of a more stable complex, has revealed the transient character of the interaction, whose properties could be exploited in nanobiosensors device for biomedical applications.

Appendix A

Atomic Force Microscopy and Spectroscopy

Atomic Force Microscopy

Atomic Force Microscopy (AFM) is a powerful high-resolution imaging tool suitable to investigate, at molecular level, the morphological properties of biological samples in physiological conditions and without the use of any label or sample manipulation (*Müller and Dufrêne, 2008; Bizzarri and Cannistraro, 2009*). For its peculiarities, AFM has emerged as one of the most innovative nanotechnological-based tool in nanoscience, also recognized for its applications in nonomedicine such as early diagnosis, pathological tissues analysis, drug delivery at the molecular level, mechanical properties of cancer cells, molecular trafficking within cells, etc. (*Jena and Hoerner, 2002; Engel and Müller, 2000; Ramachandran and Lal, 2010).* Moreover, AFM analyses complement traditional proteomic and molecular biology approaches for detecting novel biomarkers and for the functional analysis of the associated proteins and may help in the search for novel drugs.

In a typical AFM apparatus, the surface of a sample is probed with a sharp tip located at the free end of a cantilever spring. Interatomic forces (F, $10^{-12}/10^{-9}$ Newton) between the tip and the sample, mounted on a piezoelectric scanner which is able to assure a 3D positioning, causes the cantilever deflection according to the Hook's law $F=-k*d$ in which k is the cantilever spring constant and d the deflection of the cantilever with respect to the initial position. Cantilever deflection is detected through a laser beam bounces off the back of the cantilever onto a photodiode, as shown in Fig. A.1 (*Binning and Quate, 1986*). As the cantilever bends, the position of the laser beam on the photodetector shifts allowing to reconstruct the sample topography. The particular system configuration, allows a mechanical amplification of the cantilever displacement thus endowing AFM with an ultrasensitive detection capability. In fact, the apparatus is able of atomic resolution of flat surfaces or of simple molecules in which each atom is in intimate contact with the surface. For complex macromolecules nanometric resolution can be reached enabling the investigation of novel aspects even at level of single molecule and making possible to discover differences between them, undetectable with more traditional techniques. Consequently, while current methods are

able to detect biomarker concentrations at higher levels than required for early diagnosis ($<10^{-18}$ M), AFM is able to detect interaction at lower concentrations.

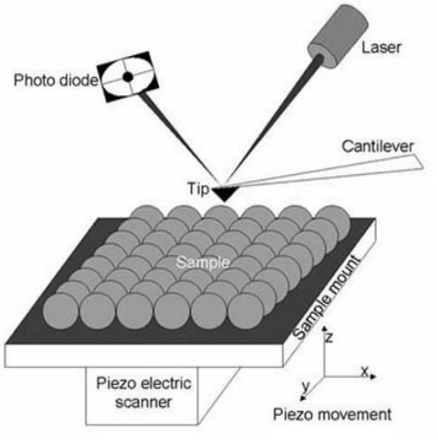

Figure A.1. Scheme of the main component of an AFM apparatus.

AFM measurements can be performed in air, vacuum and liquid, including physiological buffers. Images can be acquired in two different modality: by contact mode (CM), or by vibrating (dynamic) modes that can be classified as taping (TM) and non-contact mode (NC). In CM-mode the tip makes physical contact with the sample. In the TM-AFM modality, instead, the cantilever is put in oscillation by an internal oscillator with a frequency close to its resonance frequency (around 100 KHz) and positioned on the surface for a very small fraction of its oscillating period. The tip is still in contact with the sample but this occurs over a very short time reducing the lateral force and sample damages. Such a modality is a far better choice than CM when imaging soft sample materials like biological samples since the transient contact with the surface results in a minor destructive interaction. Fig. A.2A and A.2B show an example of images obtained by TM-AFM. Finally, in NC-AFM the cantilever is vibrated near (from tens to hundreds of angstroms) the sample surface, so it never contact the sample. The force between the tip and the sample is very low (ca. 10-12 N) and this is useful to study smooth, soft or elastic samples while the TM-AFM mode is used for rough sample.

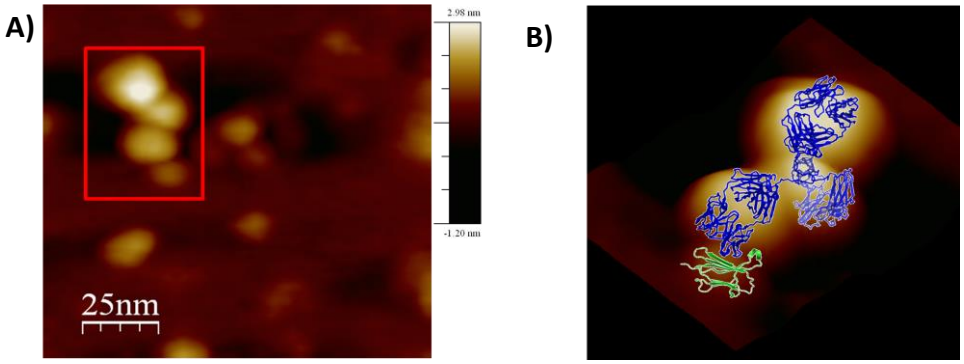

Figure A.2. A) TM-AFM image recorded in air of the complex formed by beta 2 microglobulin (B2M) and its antibody B2M-01 adsorbed on mica substrate after incubation with B2M. The complex is red squared. **B)** A zoom-in 3D topography image of the marked spot in A), interpreted as a complex formed by an antibody binding a single molecule of B2M through one antigen-binding fragment. The molecular structures of both B2M (green) and of IgG2a (blue), have been superimposed over the 3D AFM image of the complex (images not in scale). Figures are from *Coppari et al., 2016.*

Atomic Force Spectroscopy

General description

AFM can be used not only to look at a sample but also to study biomolecular recognition process when used in the modality called AFS (Atomic Force Spectroscopy). In the AFS modality, the AFM tip, functionalized with a ligand, is moved only in the vertical (z) direction, perpendicular to the sample plane where the ligand partner has been immobilized (*Hinterdorfer and Dufrêne, 2006; Bizzarri and Cannistraro, 2009 and refs. within; Bizzarri and Cannistraro, 2010 and refs. within*). When operating in this modality, the interaction forces between the functionalized tip and substrate can be measured even for only one partner couple (*Bizzarri and Cannistraro, 2012*). The functional groups involved in the interaction, the lifetime, the binding energy, can also be extrapolated, what could deserve pathological and pharmacological interest even to improve the design of new drugs. Moreover, the technique versatility has been exploited by researchers to study polymers stretching, cellular membrane elasticity, protein unfolding (*Bizzarri and Cannistraro, 2009 and refs. within; Bizzarri and Cannistraro, 2010 and refs. within*).

Fig. A.3 shows the scheme of a typical AFS experiment. One interacting partner is tethered to the AFM tip, located at the end of a spring cantilever, while the other is immobilized onto

a glass substrate. During the AFS experiment, force–distance curves are recorded: the ligand-functionalized tip, starting from point 1, is approached at a constant speed to the surface covered by the receptor, until it reaches the contact point (point 2), in the proximity of which the biorecognition process may start to take place. Further approach of the tip results in an increasing overlap of the partner molecular orbitals whose repulsion yields a cantilever upward deflection which is proportional to the applied force. The approaching is stopped when a preset maximum force value is reached (point 3); thereafter the motion of the cantilever being reversed. During the retraction, adhesion forces, and/or bonds, formed in the contact phase, cause the tip to adhere to the sample up to a distance beyond the initial contact point, following a nonlinear trend which reflects the stretching of the molecular bonds (*Hinterdorfer and Dufrêne, 2006; Bizzarri and Cannistraro, 2010*). When the spring force overcomes the interaction forces, the cantilever pulls off sharply, going to a non-contact position (point 5). Such a jump provides a measure of the unbinding force (or rupture force) between the biomolecular partners, which is given by $F=k*d$, with k being the cantilever spring constant and F the rupture or unbinding force needed to break the complex.

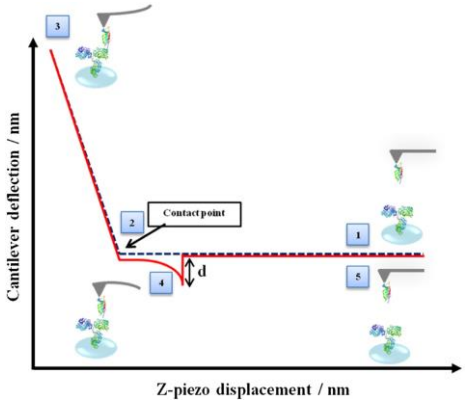

Figure A.3. Scheme of a typical approach/retraction cycle. Figure is from *Coppari et al., 2016.*

AFS data analysis

AFS experiments can be used to extrapolate interaction forces between biopartners as well kinetic parameters (k_{off}, dissociation rate constant, and x_β , width of the energy barrier) of the biorecognition process. To this aim, a careful analysis of force-curves must be firstly carried out and then specific models have to be applied for successive data analysis. Force-curves

collected in AFS unbinding experiments can significantly differ among them since the approach of functionalized tip towards a coated substrate does not necessarily result into the formation of a specific complex.. Hence, experimentally, thousands of force curves have to be acquired at many distinct positions on the substrate, also varying the loading rate, r, ($r = k \cdot v$) corresponding to the product between the retraction speed of the cantilever from the substrate, v, and its spring constant, k. Since only force curves corresponding to single specific unbinding events are to be taken into consideration for further processing, a preliminary selection should be done. Force curves are accepted showing a trend qualitatively similar of that shown in Fig. A.3 in which the retraction portion, before the jump-off, exhibits a nonlinear trend starting and ending at the zero-deflection line; such a behavior being attributed to specific events especially when flexible linkers are used to immobilize biomolecules to the tip or to the substrate. Fig. A.4 shows a few representative examples of force-distance curves; only curves 3 and 4 are representative of specific unbinding events

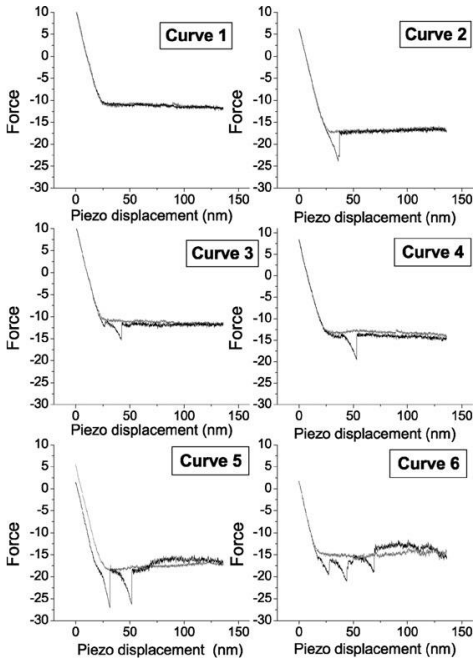

Figure A.4. Real AFS force curves for a biomolecular complex. Curve 1: no event, curve 2: nonspecific event since; curves 3 and 4: specific unbinding events; curves 5 and 6: multiple events. Figure is from *Bizzarri and Cannistraro, 2009.*

Upon selecting the curves related to specific events, the unbinding frequency, given by the ratio between successful events corresponding to specific unbinding processes over the total recorded events, is evaluated. The unbinding forces of each biorecognition events is than calculated and plotted as histograms usually displaying a Gaussian trend which is then fitted to obtain the most probable unbinding force value from the peak of the distribution.

Since the molecular dissociations measured by AFS take place under the application of an external force, the system is far from the thermodynamic equilibrium with a consequent alteration of the energy profile (Fig. A.5) (*Bizzarri and Cannistraro, 2012*). Therefore, to extract the kinetic and energy landscape parameters at the equilibrium, the use of suitable theoretical models is required (*Bell, 1978; Evans and Ritchie, 1997; Dudko et al., 2006; Friddle et al., 2012*). Bell predicted that under the application of an external force, F, the activation free energy (ΔG^*) of the reaction is lowered by a factor proportional to the applied F: $\Delta G^*(F) = \Delta G^* - Fx_\beta$ where $\Delta G^*(F)$ is the activation free energy under the application of a force F, ΔG^* is the activation free energy for a reaction at zero force, and x_β the width of the energy barrier.

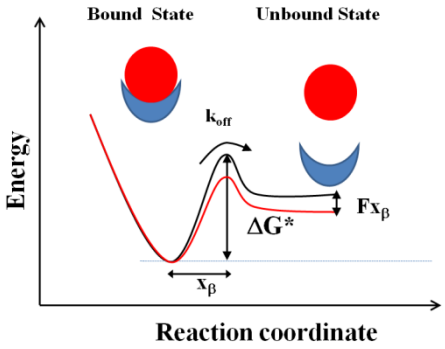

Figure A.5 A schematic diagram of the energy profile for a dissociation process of a biomolecular complex without an external force (black line) and under the application of an external force F (red line).

On the other hand, the dissociation rate $k_{off}(F)$, for an unbinding process under the application of a force F, increases exponentially by a factor proportional to F and it is thus given by: $k_{off}(F) = k_{off} \exp(Fx_\beta/k_\beta T)$ in which k_B is the Boltzmann constant, T is the absolute temperature and k_{off} is the dissociation rate constant of the unbinding event at zero force

which is given by an Arrehenius-like expression (*Kramers, 1940*): $k_{off} = w\exp(-\Delta G^*/k_\beta T)$ (with w a pre-exponential factor). Starting from the Bells assumption, Evans and Ritchie derived a description of the unbinding process in terms of a crossing over a single, sharp barrier through the application of a time-dependent force F(t), thus providing the dependence of the unbinding force on the loading rate. In particular, their model predicts a linear dependence of the most probable unbinding force, F^*, on the natural logarithm of the loading rate, r, as given by

$$F^* = \frac{k_B T}{x_\beta} \, ln\left(\frac{r x_\beta}{k_{off} k_B T}\right) \qquad (1)$$

where k_{off} is the dissociation rate constant at the equilibrium, x_β is the width of the energy barrier, k_B is the Boltzmann constant and T the absolute temperature. Experimentally, F^* is determined from the maximum of the main peak of each unbinding force histogram and r is given by the product between the retraction speed and the spring constant of the entire system, k_{syst}; the measurement of k_{syst}, calculated from the slope of the unbinding event, taking into account the contribution of the spring constant of the molecules tied to the AFM tip. By plotting F^* as a function of ln r, the equilibrium parameters k_{off} and x_β can be extracted as respectively the slope and the intercept of a linear fit (Fig. A.6).

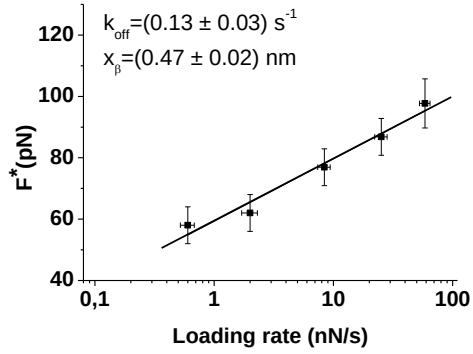

Figure A.6. An example of the linear dependence of the loading-rate on the most probable unbinding force F^*. The continuous lines represent the fit of the experimental data by the Bell–Evans model (Eq. 1). Reported data are from *Bizzarri et al., 2011*.

References

Bell GI. 1978. Models for the specific adhesion of cells to cells. *Science* **200**: 618–627.

Binning G, Quate CF. 1986. Atomic force microscope. *Phys. Rev. Lett.* **56**: 930-933.

Bizzarri AR, Cannistraro S. 2009. Atomic force spectroscopy in biological complex formation: strategies and perspectives. *J. Phys. Chem. B* **113**: 16449-16464.

Bizzarri AR, Cannistraro S. 2010. The application of atomic force spectroscopy to the study of biological complexes undergoing a biorecognition process. *Chem. Soc. Rev.* **39**: 734–749.

Bizzarri AR, Santini S, Coppari E, Bucciantini M, Di Agostino S, Yamada T, Beattie CW, Cannistraro S. 2011. Interaction of an anticancer peptide fragment of azurin with p53 and its isolated domains studied by atomic force spectroscopy. *Int. J. Nanomedicine* **6**: 3011–3019.

Bizzarri AR, Cannistraro S. 2012. Dynamic Force Spectroscopy and Biomolecular Recognition, CRC Press, Boca Raton.

Coppari E, Santini S, Bizzarri AR, Cannistraro S. 2016. Kinetics and binding geometries of the complex between β2-microglobulin and its antibody: an AFM and SPR study. *Biophys. Chem.* **211**: 19–27.

Dudko O, Hummer G, Szabo A. 2006. Theory, analysis and interpretation of singlemolecule force spectroscopy experiments. *Proc. Natl. Acad. Sci. U SA* **105**: 15755–15760.

Engel A, Müller DJ. 2000. Observing single biomolecules at work with the atomic force microscope. *Nat. Struct. Biol.* **7**: 715-718.

Evans E, Ritchie K. 1997. Dynamic strength of molecular adhesion bonds. *Biophys. J.* **72**: 1541–1555.

Friddle R, Noy A, De Yoreo J. 2012. Interpreting the widespread nonlinear force spectra of intermolecular bonds, *Proc. Natl. Acad. Sci. U SA* **109**: 13573–13578.

Hinterdorfer P, Dufrêne YF. 2006. Detection and localization of single molecular recognition events using atomic force microscopy. *Nat. Met.* **3**: 347-355.

Jena JBP, Hoerner JK. 2002. Atomic Force Microscopy in Cell Biology. *Methods in Cell Biology*, Academic Press. 2002, vol. 68.

Kramers HK. 1940. Brownian motion in a field of force and the diffusion model of chemical reactions. *Physica* **7:** 284-304.

Müller DJ, Dufrêne YF. 2008. Atomic force microscopy as a multifunctional molecular toolbox in nanobiotechnology. *Nature Nanotechn*. **3**: 261-269.

Ramachandran S, Lal R. 2010. Scope of atomic force microscopy in the advancement of nanomedicine. *Indian J. Exp. Biol*. **48**: 1020-1036.

Appendix B

Surface Plasmon Resonance

Surface Plasmon Resonance (SPR) has emerged as an innovative technique providing a non-invasive strategic tool for observing binding interactions between an analyte in solution and its partner immobilized on a substrate (*Homola et al., 1999; Cooper, 2003*). In this respect, SPR can be used in protein-binding studies, especially suited for sensitive kinetic process investigations, in real time, without labelling procedures (*Cooper, 2002*). The technique is becoming a progressively more relevant tool in clinical labs for the study of interaction partners of biological interest, such as protein-protein, protein-lipids, protein-nucleic acids, and even to monitor the interaction of proteins or nucleic acid with low molecular weight molecules such as drugs, substrates and cofactors, constituting then a quick way for checking drug interaction (*Cooper, 2002*).

SPR based instruments reveal the association between molecules only indirectly, by monitoring refractive index variations near (within 300 nm) a sensor surface. In a typical SPR apparatus (Fig. B.1) one of the two reactant molecules (ligand), is immobilized on the sensor surface while the other reactant, referred to as the analyte, flows past this surface in solution. Incident light is reflected from the internal face of a prism whose external face, coated with a thin metal film, represent the ligand-functionalized sensor chip surface. In condition of total internal reflection, the reflected photons create an evanescent field on the opposite side of the interface. At a particular critical angle (resonance angle) there is a drop in the reflected light, due to the resonance between the evanescent wave and the oscillation in the electrons (plasmons) on the surface of the metal film (*Davies, 1994*). Since the critical angle is dependent on the refractive index of the medium present on the metal surface, the method can be used to measure molecular interactions between analyte and ligand. Association and dissociation processes are measured in arbitrary units and displayed in a graph called sensorgram (Fig. B.1). Through the application of different models, connected with the analyzed system (one to one binding model, heterogeneous ligand model, heterogeneous analyte model, two state binding models…) the whole interaction process can be characterized by a kinetic point of view, resulting in the extrapolation of the dissociation rate constant (k_{off}), association rate constant (k_{on}), dissociation equilibrium constant (K_D).

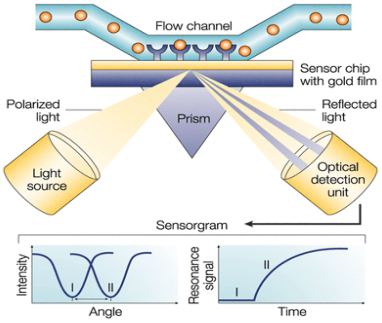

Figure B.1. Schematic representation of an SPR apparatus. Refractive index changes on the sensor chip surface as consequent to the interaction between the immobilized ligand and the analyte in solution, cause a shift in the critical (resonance) angle from I to II. This shift can be monitored in real time as a plot of resonance signal versus time (Figure is from *Cooper, 2002*).

Fig. B.2, shows the steps of a typical SPR experiment. At point 1, the receptor is immobilized, with appropriate coupling chemistry, on the sensor surface which is conditioning with a suitable buffer solution. The solution of the analyte in running buffer is then passed over the surface-immobilized receptor (point 2). As the analyte reacts with its immobilized partner (association phase), the refractive index near the sensor chip increases leading to an increase of the resonance signal (expressed in Resonance Unit, RU). The association phase then reaches a plateau at equilibrium, when the amount of associated and dissociated analyte is equal (point 3). Next, at point 4, buffer is injected onto the sensor chip surface and the non-specifically bound components are flushed off. The dissociation of the analyte also starts at this step, enabling the kinetics of the dissociation process to be studied. Many complexes have considerable half life so that a regeneration solution is injected, breaking the specific binding between analyte and ligand (point 5, regeneration phase). The entire process can be followed in real time. The described cycle is repeated many times at different analyte concentrations and a sequential fitting of the association and dissociation curves with a predefined model is applied to extract the kinetic parameters of the interaction.

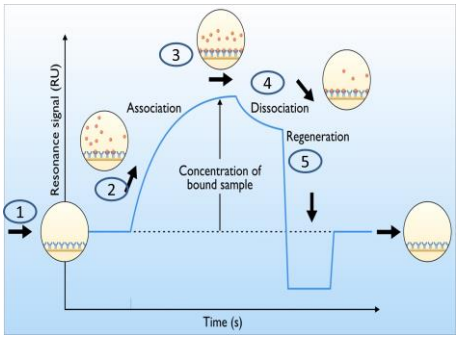

Figure B.2 Typical binding cycle observed with an SPR apparatus.

For a better understanding of the SPR application, I here report the SPR study I have performed on the interaction between beta 2 microglobulin (B2M) and its antibody (mAbB2M-01). The system is generally used as benchmark for the technique standardization but I have also used it to integrate results obtained at the single molecule level by AFS and AFM. Data have been published in *Coppari et al., 201*6.

SPR surface preparation

SPR experiments on the B2M/mAbB2M-01 system were carried out at 25 °C by using PBS (50 mM K3PO4, 150mMNaCl, pH 7.5, surfactant P20 0.005% from GE Healthcare) as running buffer. The mAbB2M-01 proteins (ligand) were covalently immobilized on a CM5 sensor chip surface (GE Healthcare, Uppsala, Sweden) by using an amine coupling kit according to the manufacturer's instructions. Briefly, the dextran matrix of the sensor chip surface was initially equilibrated with running buffer and its carboxyl groups were successively activated by a mixture of N-hydroxyl-succinimide (NHS) and N-ethyl-N-(3-diethylaminopropyl) carbodiimide (EDC). mAbB2M- 01 (0.025 μg/μL in 10 mM acetate buffer pH 4.5, GE Healthcare, Uppsala, Sweden) was injected for coupling reaction until 1400 RU immobilization level was reached resulting from the reaction of the lysine amino groups exposed on the mAbB2M-01 surface with the functionalized sensor chip matrix. Actually, unreacted NHS-esters were blocked by a 1 M ethanolamine-HCl, (pH 8.5, GE Healthcare, Uppsala, Sweden) injection. Therefore, running buffer was fluxed over both flow cells until the baseline was stable. A control flow cell was prepared without intermediate ligand immobilization, and successively used to correct the experimental data for refractive index changes and no specific interaction.

Kinetic experiment

Binding assay was performed by a multi-cycle kinetic (MCK) approach (*Morton and Myszka, 1998*) in which increasing concentrations of the analyte are injected over the sensor chip surface with intermediate regeneration steps that break the ligand-analyte interaction and remove the bound analyte molecules. Five increasing concentrations of B2M protein (analyte) in the range of 5–500 nM were thus sequentially injected over both the functionalized and the reference flow cell surfaces at a flow rate of 30 μL/min for 180 s. Each analyte injection was followed by 300 s of dissociation step with a 30 μL/min flux of running buffer and then by a 20 s pulse of regeneration solution (10 mM Gly-HCl, pH 2.5, from GE Healthcare, Uppsala, Sweden) to remove the B2M molecules bound to the mAbB2M-01 antibody. The binding assay also included three startup cycles using buffer to equilibrate the surface, as well a zero concentration cycle of analyte in order to have a blank response usable for double reference subtraction (*Morton and Myszka, 1998*). All the procedures were completely automated. Data evaluation was performed by using the BiaEvaluation software 2.1 (GE Healthcare, BIOSciences AB, Uppsala, Sweden). The experimental curves (sensorgrams) from the functionalized surface were corrected for bulk refractive index changes, drift, and jumps due to injection needle positioning by subtracting the response obtained from the reference flow cell. The contribution of the running buffer was then subtracted. Kinetic parameters were extracted by a global fit of the corrected sensorgrams with the heterogeneous ligand model. Fits were evaluated by $\chi 2$ value and residual plots.

SPR kinetic results

Fig. B.3A and B show that, as far as increasing concentrations of B2M (coloured lines) are injected over the mAbB2M-01 functionalized sensor chip surface, a proportional increase of the SPR signal is observed; such an effect being due to the specific interaction of increasing amount of B2M with the mAbB2M-01 biomolecules. After 180 s of analyte injections, running buffer is fluxed over both the ligand and the reference surface and the SPR signal drops down as a consequence of the spontaneous dissociation of B2M/mAbB2M-01 complexes.

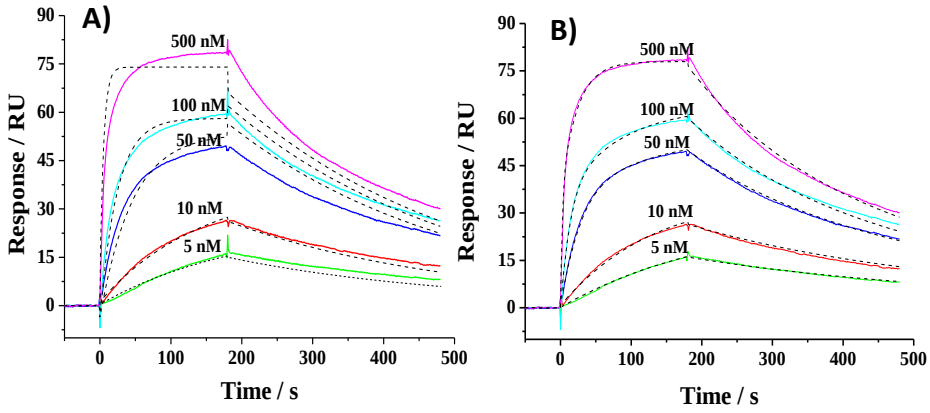

Figure B.3. SPR sensorgrams resulting from the association and dissociation of B2Mon mAbB2M-01-modified sensor chip surface (continuous coloured lines). **A)** Fit of sensorgrams by the 1:1 binding model and **B)** by the heterogeneous ligand model (black, dotted lines); the latter having been used to extract the kinetic parameters, k_{on}, k_{off}, and K_D.

To determine the B2M/mAbB2M-01 binding kinetics, the SPR data have been analyzed with two different kinetic models: i) the Langmuir 1:1 binding model and ii) the heterogeneous ligand model. The first model assumes a simple reversible bimolecular reaction between the ligand (L) and the analyte (A) (*Björquist and Boström, 1997; Santini et al., 2014*), with the formation of the surface-bound ligand–analyte (LA) complex, according to the following scheme:

$$A + L \underset{k_{off}}{\overset{k_{on}}{\rightleftarrows}} LA \qquad \text{(Scheme 1)}$$

where k_{on} and k_{off} are the specific association and dissociation rate constants of the LA complex. On the other hand, the heterogeneous ligand model assumes the existence on the ligand of different binding sites for the analyte (L_1 and L_2), each one binding a single analyte molecule with a specific affinity (*O'Shannessy and Winzor, 1996*). The model can be described by the following scheme :

$$L_1 + A \underset{k_{off1}}{\overset{k_{on1}}{\rightleftarrows}} L_1A \quad and \; L_2 + A \underset{k_{off2}}{\overset{k_{on2}}{\rightleftarrows}} L_2A \qquad \text{(Scheme 2)}$$

where k_{onn} and k_{offn} (n=1 or 2) are the association and dissociation rates for the corresponding reactions, 1 or 2. Fig. B.3A and B shows the best fit obtained by the 1:1 binding model and the heterogeneous ligand model, respectively (black dotted lines). From a visual inspection it is evident that the heterogeneous ligand model fits better the experimental data (Fig. B.3B, black dotted lines) than the simplest 1:1 binding model. This is as also confirmed by the $\chi 2$ values, being of ~0.6 and ~8.5 for the heterogeneous ligand model and the 1:1 binding model, respectively. The two kinetic parameter sets extracted from the heterogeneous ligand model were: k_{on1} = (7.9 ± 0.1) · 10^4 M^{-1} s^{-1}, k_{off1} = (49.7 ± 0.4) · 10^{-4} s^{-1}; k_{on2}= (9.5 ± 0.1) · 10^5 M^{-1} s^{-1} ; k_{off2} = (28.2 ± 0.4) · 10^{-4} s^{-1}. These results indicate the presence of two binding sites characterized by very similar interaction kinetics. In particular, both of them have rather long dissociation times: τ_1= 201 s and τ_2 = 354 s, respectively. Additionally, the corresponding dissociation equilibrium constants K_D, given by k_{off}/k_{on}, are: K_{D1} = (6.3 ± 0.1) · 10^{-8} M and K_{D2} = (2.9 ± 0.1) · 10^{-9} M. These values indicate a high affinity and fall within the range expected for the very stable and specific complexes (*Bizzarri and Cannistraro, 2010*).

References

Bizzarri AR, Cannistraro S. 2010. The application of atomic force spectroscopy to the study of biological complexes undergoing a biorecognition process. *Chem. Soc. Rev.* **39**: 734–749.

Björquist P, Boström S. 1997. Determination of the kinetic constants of tissue factor/factor VII/factor VIIa and antithrombin/heparin using surface plasmon resonance. *Thromb. Res.* **85:** 225–236.

Cooper MA. 2002. Optical biosensors in drug discovery. *Nat. Rev. Drug Discov*. **1**: 515-528.

Cooper MA. 2003. Label-free screening of bio-molecular interactions. *Anal. Bioanal. Chem*. **377:** 834-842.

Coppari E, Santini S, Bizzarri AR, Cannistraro S. 2016. Kinetics and binding geometries of the complex between β2-microglobulin and its antibody: an AFM and SPR study. *Biophys. Chem*. **211**: 19–27.

Davies J. 1994. Review: Surface plasmon resonance-The technique and its applications to biomaterial processes. *Nanobiol.* **3**: 5-16.

Homola J, Sinclair SY, Gauglitz G. 1999. Surface plasmon resonance sensors: review. *Sens actuators* **54**: 3-15.

Morton TA, Myszka DG. 1998. Kinetic analysis of macromolecular interaction using surface plasmon resonance biosensors. *Methods Enzymol*. **295**: 268–294.

O'Shannessy DJ, Winzor DJ. 1996. Interpretation of deviations from pseudo-first-order kinetic behavior in the characterization of ligand binding by biosensor technology. *Anal. Biochem*. **236**: 275–283.

Santini S, Di Agostino S, Coppari E, Bizzarri AR, Blandino G, Cannistraro S. 2014. Interaction of mutant p53 with p73: a surface plasmon resonance and atomic force spectroscopy study. *Biochim. Biophys. Acta Gen. Subj*. **1840**: 1958–1964.

Summary

Tumour suppressor p53, the so called "guardian of the genome" for its crucial role in the cell cycle progression control and coordination of cellular response to a broad range of stress factors, is a common denominator in human cancers, in most of which it is mutated or its pathway altered. Its prominent position in tumour development has stimulated a lot of research with the aim to target it or its pathway for the development of improved cancer therapies. In connection with this, the focus of this work has been the molecular and kinetic characterization of biomolecular interactions of pharmaceutical interest involving the oncosuppressor p53 both in its wild type and mutated form, proteins belonging to the p53 family, and peptides or proteins showing anticancer activities somehow connected with the p53 pathway. To this aim, Atomic Force Spectroscopy (AFS) and Surface Plasmon Resonance (SPR), have been used, supported by computational approaches and fluorescence spectroscopy. This work, conceived as the natural progression of a wide project in which I was involved since my master thesis, has been supported by the Italian Association for Cancer Research (AIRC) and carried out in the framework of the close collaboration with the Research Group of Dr. C. Beattie (Department of Surgical Oncology, Illinois University, Chicago) and with that of Dr. G. Blandino (Translational Oncogenomic Unit, Molecular Medicine Area, Regina Elena National Cancer Institute, Rome).

Chapter 1 provides an overview about oncosuppressor p53 and its pathway, its involvement in cancer development and the possible strategies that could be applied to stabilize and reactivate it in cancer cells. Moreover great attention is devoted to the anticancer peptide p28. It is a 28 amino acids peptide fragment formed by the residues 50–77 (LSTAADMQGVVTDGMASGLDKDYLKPDD) of the blue copper protein Azurin, and which has recognized anticancer role both *in vitro* and *in vivo*, connected with its interaction with the guardian of the genome p53. Even though p28 is now in the second clinical trial in patients with advanced refractory central nervous system tumours under FDA allowance, its mode of action has not been completely elucidated. This has been the main object of **Chapter 2.** Here, the results of some preliminary studies that I performed during my master thesis, concerning the use of AFS and computational method to study the interaction of p28 with full length p53 and its fragments, are reported. Indeed, the AFS study revealed that p28 forms a stable complex with the DBD of p53, while computational methods allowed me to

specifically define the molecular details of the p28/DBD interaction. These data, also combined with most common biochemical approaches, have allowed to elucidate the p28 mode of action, as reported in a work published on *British Journal of Cancer,* of which I am a co-author. The L_1 loop (aa 112–124), a region within the S_7–S_8 loop (aa 214–236) and residues T140, P142, Q144, W146, R282 and L289 of the p53DBD were identified as sites for p28 binding. Since the p28 binding region on p53, overlaps the p53 binding site for the ubiquitin ligase COP1, p28 is able to hamper the p53/COP1 interaction and the subsequent ubiquitination and proteasomal degradation of the guardian of the genome, leading to its stabilization and increase of its intracellular levels. p53 thus up-regulates the downstream molecules p21 and p27 in p53 wild type and, at least some, p53 mutant cancer cells, resulting in the down regulation of FoxM1, and leading to the inhibition of cell cycle at G_2–M phase.

Once the p28 mode of action was defined, I have used AFS for a detailed study of the p28 interaction with specific DBD mutants, as reported in **Chapter 3.** Non physiological DBD mutants L114D, A119D, C124D, C229D were taken into account, in which, non-polar hydrophobic residues, located in DBD loops involved in the interaction with p28, have been substituted with aspartate. Despite being non physiological mutants, they provide an excellent model for *proof of concept* that any alteration in p28 binding would be due to a mutation-induced structural change of the p53DBD that potentially reduce the hydrophobicity of the p28 binding site. Moreover, also the p28 interaction with the physiological DBD mutants K164E, R273H, and double mutant P223L,V274F has been investigated. The AFS study has been supported by computational methods by Prof. Beattie group and Raman studies by Prof. Cannistraro group to which I belong, in order to have a global vision of the possible correlation between the p28 binding, DBD conformation, hydrophobicity degree of the p28 binding site and the p28 biological activity. Overall, data have suggested that mutation induced reductions in the β-sheet content of specific motifs within the p53 DBD are associated with a loss of secondary structure and conformation essential to the integrity of p28 binding to the p53 DBD.

The inhibition of p53 interaction with ubiquitin ligases to stabilize and activate it, is only one of the possible strategies that could be adopted to treat cancer. In fact, it has been found that mutant p53 not only can lose its wild type function but it can acquire new oncogenic functions, among which the capability of interacting with and sequestrate p73 thus inhibiting its anticancer function and making cancerous cells more aggressive and

chemoresistent. In this context, the efforts to search innovative pharmaceutical drugs and molecules able to dissociate the aberrant mutantp53/p73 complex safeguarding the p73 activity are arousing greater interest. This requires however a deeper knowledge of the molecular and kinetic details of the mutant p53/p73 interaction. In connection with this, **Chapter 4,** reports the application of AFS and SPR to study at single molecule level and in bulk conditions, respectively, the interaction of both wild type and mutant p53R175H with p73. The study revealed that a stable complex is formed between mutant p53R175H and p73, characterized by a high interaction force and a dissociation equilibrium constant in the order of 10^{-7} M. No binding is instead observed between p73 and wild type p53.

Finally, in **Chapter 5** Azurin interaction with its physiological partner Cytochrome C551 by SPR and fluorescence spectroscopy has been investigated. Indeed it is known that Azurin, as the p28 peptide belonging to it, has anticancer activity consequent to its interaction with p53 which lowers the rate of p53 interaction with the ubiquitin ligase MDM2. As it cannot be rule out that Azurin anticancer activity could involve oxygen reactive species generation in some way connected with its electron transfer capability, the attempts to knowledge of the Azurin physiological role and interaction with its physiological partner, have attracted a fairly good interest. The study reported in Chapter 5 points out the occurrence of an encounter complex between Azurin and Cytochrome C551 that evolves toward the formation of a more stable complex involving the single protein Trp residue. The dissociation constants K_{Ds} values obtained by both SPR and emission fluorescence reflect a high turnover of the interaction and are consistent with the formation of a transient complex in agreement with the electron transfer capability of Azurin.

Finally, in **Chapter 6,** results are resumed together with the remaining issues and future perspectives.

Two appendices complete my thesis, dealing with the description of the two main approaches I have used for my studies, AFS (Appendix A) and SPR (Appendix B).

Riassunto

Il soppressore tumorale p53, chiamato anche guardiano del genoma per il suo ruolo cruciale nel controllo della progressione del ciclo cellulare e la coordinazione della risposta cellulare ad una vasta gamma di fattori stressogeni, è un comune denominatore nei tumori umani nella maggior parte dei quali risulta mutato o il suo pathway alterato. La sua posizione prominente nello sviluppo dei tumori, ha stimolato molte ricerche con lo scopo di targhettare il p53 o il suo pathway per lo sviluppo di terapie anticancro. In connessione con questo, il focus di questo lavoro è stato la caratterizzazione molecolare e cinetica di interazioni biomolecolari di interesse farmacologico coinvolgenti l'oncosoppressore p53, sia nella forma wild type che mutata, proteine appartenenti alla famiglia del p53, e peptidi o proteine con attività anticancro in qualche modo connessa con il pathway del p53. A questo scopo sono state usate la spettroscopia di forza atomica (AFS) e la risonanza plasmonica di superficie (SPR), supportate da approcci computazionali e spettroscopia di fluorescenza. Questo lavoro, concepito come il naturale proseguimento di un progetto più ampio in cui sono stata coinvolta a partire dalla mia tesi di laurea, è stato supportato dall'associazione italiana per la ricerca sul cancro (AIRC) e realizzato nell'ambito della stretta collaborazione con il gruppo di ricerca del Dr. Beattie (Dipartimento di Oncologia Chirurgica, Università dell'Illinois, Chicago) e del Dr. Blandino (unità di Oncogenomica Traslazionale, area di medicina molecolare, Istituto Nazionale Tumori Regina Elena, Roma).

Il **Capitolo 1** fornisce una visione d' insieme circa l'oncosoppressore p53 e il suo pathway, il suo coinvolgimento nello sviluppo del cancro e le possibili strategie che potrebbero essere messe in atto per stabilizzarlo e riattivarlo nelle cellule cancerogene. Inoltre, grande attenzione è rivolta al peptide anticancro p28. Si tratta di un frammento peptidico di 28 amino acidi formato dai residui 50-77 (LSTAADMQGVVTDGMASGLDKDYLKPDD) della proteina blu rame Azzurrina, e che ha una riconosciuta attività anticancro, sia *in vitro* che *in vivo*, connessa con l'interazione con il guardiano del genoma p53. Anche se il p28 si trova nella seconda fase del trial clinici in pazienti con tumori avanzati refrattari del sistema nervoso centrale su autorizzazione della FDA, come esso eserciti la sua funzione non è stato del tutto delucidato. Questo è stato l'oggetto principale del **Capitolo 2**. Qui, i risultati di alcuni studi preliminari che ho effettuato durante la tesi di laurea, riguardanti l'uso della AFS e di approcci computazionali per studiare l'interazione del p28 con il p53 full length e i suoi

frammenti, sono riportati. Lo studio di AFS infatti, aveva rivelato che il p28 forma un complesso stabile con il DBD del p53 mentre metodi computazionali mi avevano consentito di definire in modo specifico i dettagli molecolari dell'interazione p28/DBD. Questi dati, combinati anche con i più comuni metodi biochimici, hanno consentito di delucidare la modalità di azione del p28, come riportato in un lavoro pubblicato su *British Journal of Cancer*, del quale sono coautrice, Il loop L_1 (aa 112-124), una regione all'interno del loop S_7-S_8 (aa 214-236) ed i residui T140, P142, Q144, W146, R282 e L289 del p53 DBD sono stati identificati come siti di interazione per il p28. Poichè la regione di interazione del p28 con il p53, si sovrappone ai siti del p53 coinvolti nell'interazione con l'ubiquitina ligasi COP1, il p28 è in grado di bloccare l'interazione COP1/p53 e quindi la successiva ubiquitinazione e degradazione proteasomica del guardino del genoma, portando alla sua stabilizzazione e all'aumento dei suoi livelli intracellulari. p53 quindi up regola le molecole a valle p21 e p27 nelle cellule con p53 wild type e, almeno alcune, con p53 mutato, risultando nella down regolazione di FoxM1 e portando alla inibizione della progressione del ciclo cellulare nella fase G_2-M.

Una volta che la modalità di azione del p28 è stata definita, ho usato l'AFS per lo studio dettagliato della interazione del p28 con mutanti specifici del DBD come riportato nel **Capitolo 3.** I mutanti non fisiologici del DBD L114D, A119D, C124D, C229D, sono stati considerati, in cui residui non polari idrofobici, localizzati in loops del DBD coinvolti nella interazione con il p28, sono stati sostituiti con aspartato. Sebbene siano mutanti non fisiologici, tuttavia forniscono un eccellente modello per provare il concetto che ogni alternazione nel binding del p28 potrebbe essere dovuta ad un cambiamento strutturale indotto da una mutazione, che potenzialmente riduce l'idrofobicità del sito di interazione del p28. Inoltre, è stata studiata anche l'interazione del p28 con i mutanti fisiologici del DBD K164E, R273H, ed il doppio mutante P223L,V274F. Lo studio di AFS è stato supportato da metodi computazionali utilizzati dal gruppo del Prof. Beattie e da studi Raman condotti dal gruppo del Prof. Cannistraro al quale appartengo, al fine di avere una visione globale sulla possibile relazione tra il legame del p28, la conformazione del DBD, il grado di idrofobicità del sito di interazione del p28 e la sua attività biologica. Nell'insieme i dati hanno suggerito che le riduzioni del contenuto in foglietti beta indotte dalle mutazioni, in specifici motivi del DBD, sono associate ad una perdita di struttura secondaria e conformazione essenziali all'integrità del binding del p28 al p53DBD.

L'inibizione dell'interazione del p53 con ubiquitin ligasi al fine di stabilizzarlo ed attivarlo, è solo una delle possibili strategie che possono essere adottate per trattare il cancro. Infatti è stato dimostrato che il mutante p53 non soltanto può perdere la sua funzione wild type ma può acquisire nuove funzioni oncogeniche, tra le quali la capacità di interagire con il p73 e sequestrarlo, inibendo in questo modo la sua funzione anticancro e rendendo le cellule cancerose più aggressive e chemioresistenti. In questo contesto, gli sforzi nel cercare farmaci anticancro innovativi e molecole in grado di dissociare l'aberrante complesso costituito da p53mutato/p73 salvaguardando in questo modo la funzione del p73, stanno suscitando un grande interesse. Questo richiede tuttavia una conoscenza approfondita dei dettagli molecolari e cinetici dell'interazione p53 mutato/p73. In connessione con questo, il **Capitolo 4** riporta l'applicazione dell' AFS dell' SPR per studiare, a livello di singola molecola ed in bulk, rispettivamente, l'interazione del p53 wild type e del mutante p53R175H con il p73. Lo studio ha rivelato che si forma un complesso stabile tra il p53 R175H ed il p73, caratterizzato da un'alta forza di interazione e da una costante di dissociazione all'equilibrio nell'ordine di 10^{-7} M. Nessuna interazione è stata invece osservata tra il p73 ed il p53 wild type.

Infine, nel **Capitolo 5** è stata studiata l'interazione della proteina Azzurrina con il suo partner fisiologico, Citocromo C551, tramite SPR e spettroscopia di fluorescenza. Infatti è noto che l'Azzurrina, come il p28 che da essa deriva, possiede attività anticancro conseguente alla sua interazione con il p53 che a sua volta riduce la l'interazione di p53 con l'ubiquitina ligasi MDM2. Poiché tuttavia non può essere escluso che l'attività anticancro della proteina possa coinvolgere la generazione di specie reattive dell'ossigeno, in qualche modo connessa con la sua capacità di trasferimento elettronico, il tentativo di conoscere il ruolo fisiologico dell'Azzurrina e i dettagli della sua interazione con il citocromo C551, hanno attratto grande interesse. Lo studio riportato nel Capitolo 5 ha evidenziato l'esistenza di un "encounter complex" tra l'Azzurrina ed il Citocromo C551 che evolve verso la formazione di un complesso più stabile che coinvolge il singolo Trp della proteina. I valori delle costanti di dissociazione K_{Ds} ottenuti tramite SPR e emissione di fluorescenza, riflettono l'alto turnover del complesso e sono consistenti con la formazione di un complesso transiente in accordo con le proprietà di trasferimento elettronico dell'Azzurrina.

Infine, nel **Capitolo 6** vengono riassunti i principali risultati ottenuti insieme alle questioni ancora aperte e prospettive future.

Due appendici completano la mia tesi, riguardanti la descrizione dei due principali approcci che ho usato nei miei studi, AFS (Appendice A) ed SPR (Appendice B).

List of publications

Coppari E, Santini S, Bizzarri AR, Cannistraro S. 2016. Kinetics and binding geometries of the complex between ß2-microglobulin and its antibody: An AFM and SPR study. *Biophys. Chem.* **211**: 19-27.

Santini S, Di Agostino S, Coppari E, Bizzarri AR, Blandino G, Cannistraro S. 2014. Interaction of mutant p53 with p73: a Surface Plasmon Resonance and Atomic Force Spectroscopy study. *Biochim. Biophys. Acta* **1840**: 1958-1964.

Santini S, Bizzarri AR, Yamada T, Beattie CW, Cannistraro S. 2014. Binding of azurin to cytochrome c 551 as investigated by surface plasmon resonance and fluorescence. *J. Mol. Recognit.* **27**: 124-130.

Yamada T, Christov K, Shilkaitis A, Bratescu L, Green A, Santini S, Bizzarri AR, Cannistraro S, das Gupta T, Beattie C. 2013. p28, a First in Class Peptide Inhibitor of COP1 Binding to p53. *British J. Cancer* **108**: 2495-2504.

Bizzarri AR, Brida D, Santini S, Cerullo G, Cannistraro S. 2012. Ultrafast Pump-Probe Study of the Excited-State Charge-Transfer Dynamics in Blue Copper Rusticyanin. *J. Phys. Chem. B* **116**: 4192–4198.

Bizzarri AR, Santini S, Coppari E, Bucciantini M, Di Agostino S, Yamada T, Beattie CW, Cannistraro S. 2011. Interaction of an Anticancer Peptide Fragment of Azurin with p53 and its Isolated Domains studied by Atomic Force Spectroscopy. *Int. J. Nanomedicine* **6**: 3011-3019.

Santini S, Bizzarri AR, Cannistraro S. 2011. Modelling the interaction between the p53 DNA-binding domain and the p28 peptide fragment of Azurin. *J. Mol. Recognit.* **24**: 1043-1055.

Curriculum vitae

Simona Santini was born on 24 July, 1986 in Soriano nel Cimino (Viterbo), Italy. In Viterbo she attended to high school from 2000 to 2005 at the Scientific Gymnasium “Paolo Ruffini”. Later, she studied Biology from 2005 to 2008 at the University of Tuscia, Viterbo, where she graduated with honours in 2008. In the same year she enrolled at the degree in Cellular and Molecular Biology. In 2010 she started to prepare her master thesis at the Biophysics and Nanoscience Center under the supervision of Prof. Salvatore Cannistraro (University of Tuscia). There, she experienced studies of molecular docking, Atomic Force Spectroscopy, Atomic Force Microscopy, UV-visible and fluorescence spectroscopies. Moreover, she followed an intensive training on the use of the SPR apparatus Biacore X100. She defended her master thesis entitled "Molecular interaction of p53 and its domains with an anticancer azurin-derived peptide" in April 2011, and she graduated with honors. From April 2011 to February 2013 she continued her work in the group of Prof. Salvatore Cannistraro thanks to a scholarship holder "Application of Surface Plasmon Resonance to the interaction of p53 with antitumor polypeptides" funded by the Italian Association for Cancer Research and then in 2013 she started her PhD course in Genetics and cell biology at the Biophysics and Nanosciece Center and she continued to work in the context of the AIRC projects. During her PhD course she perfected the use of nanotechnological technique, especially concerning the application of Surface Plasmon Resonance for the study of biomolecular recognitions of pharmaceutical interest. Moreover, she experienced with Fluorescence Resonance Energy Transfer also attending at the 11th European short course on fluorescence spectroscopy, held in Berlin, (Germany), November 4-7, 2013. The aim of her PhD work was the application of nanoscopic and spectroscopic techniques to study biomolecular recognitions involving tumour suppressor p53, p53 family proteins, peptide and proteins with anticancer activity somehow connected with the p53 pathway.

Acknowledgements

I would express my sincere gratitude to my Professors Salvatore Cannistraro and Anna Rita Bizzarri, who have guided me in these years and gave me a great opportunity for growth, and learning.

Thanks are due to all people who have collaborated on this project, especially to Dr. Silvia Di Agostino and Dr. Giovanni Blandino (Translational Oncogenomic Unit, Molecular Medicine Area, Regina Elena National Cancer Institute, Rome, Italy), Dr. Tohru Yamada and Dr. Craig W. Beattie (Departments of Surgical Oncology University of Illinois College of Medicine, and Scientific Officer of CDG Therapeutics, Inc. of Chicago, USA), Dr. Monica Bucciantini (Department of Biomedical, Experimental and Clinical Sciences, University of Florence, Florence, Italy).

At last, a heartfelt thanks to my mother, who has always encouraged and supported me.